DISSERTATION | DOCTORAL THESIS

Titel | Title

Characterization of a novel selective autophagy pathway for protein quality control in *Arabidopsis thaliana*

verfasst von | submitted by

Marintia Mayola Nava García

angestrebter akademischer Grad | in partial fulfilment of the requirements for the degree of

Doctor of Philosophy (PhD)

Wien | Vienna, 2025

Studienkennzahl lt. Studienblatt | Degree programme code as it appears on the student record sheet:	UA 794 620 490
Dissertationsgebiet lt. Studienblatt | Field of study as it appears on the student record sheet:	Molekulare Biologie
Betreut von | Supervisor:	Yasin Dagdas PhD

AGRADECIMIENTOS

Primero quiero agradecer a mi madre, Alicia García por ser mi apoyo incondicional y por creer en mí. Por darme alas, acompañarme en mi vuelo y no dejarme caer. Por ser mi gran compañera de vida y hacerme sentir amada y protegida, sin importar la distancia. Gracias por dejarme ir para hacer mi vida y perseguir mis sueños, a pesar del dolor que nos provoca la distancia.

A mi padre, Jesús Nava, por enseñarme a darme mi lugar y hacerme respetar, a defender mi dignidad e individualidad. Gracias por enseñarme a no ser ni ama ni esclava. Tus letras, su filosofía y su música, me han acompañado toda mi vida. Gracias por creer en mí, echarme porras y hacerme sentir orgullosa de quien soy.

Gratitud enorme a los dos por su sacrificio, por apoyarme siempre y por ser mis mejores consejeros. Sin ustedes esto no hubiera sido posible. Los amo y llevo conmigo siempre.

A mi hermano Eliseo Nava, por crecer a mi lado, por su cariño y apoyo incondicional, y por cuidar a Laika y mis padres en mi ausencia.

A Laika, mi perra, le doy las gracias por haberme acompañado al inicio de mi viaje por la ciencia, por ser mi compañera de estudios, de desvelos y vida. Pero principalmente, por hacerme tan feliz y hacerme sentir tan plena con tan solo existir. También le agradezco por cuidar a mi familia en mi ausencia y por enseñarme a ser la perra más perra.

A Pierre, por darle brillo a mi vida y ser un faro de luz en mi noche oscura. Gracias por remar conmigo en contra de la corriente y mantenernos a flote ante la adversidad.

A mi madrina Geo y a mi tita Cris, por siempre apoyarme y recibirme con los brazos abiertos y llenos de amor. Y por cuidar a mi madre y mi hermano.

A mis abuelas por ser mujeres trabajadoras y a toda mi familia por su amor incondicional.

A Helí Morales también por haberme acompañado en una fase muy complicada en esta odisea y ayudarme a mantenerme a flote.

Y finalmente a mí misma, por haber resistido todo este tiempo, por mi enorme esfuerzo y trabajo. Principalmente por no haber comprometido my dignidad ni integridad y siempre alzar mi voz. Y por haber escrito esta tesis en dos semanas.

ACKNOWLEDGEMENTS

After acknowledging my family, I want to thank my friends Júlia, Mélanie, and Nina, who have been essential throughout these five years in Vienna. They have always been there for me, sharing tears, anger, and moments of joy and beauty. I am very lucky to have you. I also want to thank Marlene, my physiotherapist, who has kept my body going throughout this year.

From the GMI, I would like to thank Yasin Dagdas, my supervisor, for allowing me to work in his lab. I also thank former lab members like Marion Clavel, for teaching me to work with *Arabidopsis thaliana*, and Roksolana Kobylinska, my dear friend, who made my time at the GMI so enjoyable and beautiful. I am also grateful to current lab members, including Jierui Zhao, who taught me confocal microscopy and image analysis; Nenad Grujic, who keeps the lab running smoothly and has always provided seeds and help when needed; Peng Gao, for performing the EM analysis for this study; and last but not least, Angelina Gross, for insightful scientific and life discussions and for making my final year at the GMI much better. Additionally, I am grateful to Liam Dolan for his valuable scientific advice.

I would also like to thank Lyna Benchalel, the Master's student I supervised, who, as part of her project, studied CESAR and NBR1 crosstalk. She is a wonderful person to work with, and her dedication and values shine through her work.

From the VBC, I want to thank the Training Team, particularly Eva Schmid, for her professionalism and dedicated work. I am also grateful to all the outstanding core facilities at the VBC, especially the Proteomics Facility, and in particular, Elisabeth Roitinger and Karel Stejskal, with whom I worked closely.

I also wish to express my appreciation to Tim Clausen and Silvia Ramundo, members of my TAC, for their invaluable scientific advice and support.

Finally, I want to thank my reviewers, Erika Isono and Barbara Korbei, for accepting the challenge of reviewing my thesis within a month, as well as my examiner, Elif Karagöz.

TABLE OF CONTENTS

CONTRIBUTIONS

All the experiments and data analysis shown were performed by the author of this doctoral thesis with the following exceptions:

Part1: Identification of CESAR as an AIM-dependent ATG8 interactor

Figures 6 and 7 – Phylogenetic analysis and their representation in figures were done by Víctor Sánchez de Medina and Varsha Marthur.

Figure 7 Datasets - *Arabidopsis thaliana* datasets were produced by the author of this doctoral thesis. Datasets for *Chlamydomonas reinhardtii, Marchantia polymorpha, Nicothiana benthamiana,* and *Physcomitirum patens*, were performed by co-authors of the resulting manuscript, including Marta García León, Jakob Valdbjørn and Víctor Sánchez de Medina.

Figure 8 and S1 - Sample preparation and AP-MS of ATG8 in *A.thaliana* was performed by the author of this doctoral thesis, as well as the pre-analysis of the proteomics data. Marion Clavel performed the final analysis and elaborated the figures for proteomic data representation.

Part2: Characterization of CESAR as a Selective Autophagy Receptor

Figures S2 and **S3 –** The phylogenetic tree of CESAR, the in vitro pulldowns were done by Víctor Sánchez de Medina.

Figures 10C and **S5** – EM was performed by Peng Gao.

Figures 16B and **16C** – In vitro pulldowns were performed by Víctor Sánchez de Medina.

Figure 16D – Gaurav Anand performed the experiment.

Figures 16 E-H and **Figures S11 C-F** – The author of this doctoral thesis optimized the treatments conditions and prepared the *A.thaliana* samples. Víctor Sánchez de Medina performed the TUBE-pulldown assays.

Figure 16 I-K – Fractionation assays were performed by Andreev Veselin.

Part4: CESAR and NBR1 crosstalk

Figures 18A and **B** – Lyna Benchalel performed the microscopy and subsequent analysis as part of her Master thesis under the supervision of the author of this doctoral thesis.

Figures 19A, 19B and **S14** - Lyna Benchalel performed the experiments under the supervision and assistance of the author of this doctoral thesis.

The results presented in this doctoral thesis, except Part 4, ended up in the following manuscript:

Sánchez de Medina, V. S. and Nava García, M.M., et al (2024). Cross-species interactome analysis uncovers a conserved selective autophagy mechanism for protein quality control in plants. *bioRxiv*. https://doi.org/10.1101/2024.09.08.611708

ABSTRACT

Rising temperatures caused by climate change present a significant challenge to plant growth and survival, posing a substantial risk to global food security. To maintain cellular homeostasis under both biotic and abiotic stresses, plants have evolved intricate protein quality control mechanisms, including selective autophagy. This process is mediated by selective autophagy receptors (SARs), which recognize and target specific cellular components—such as damaged organelles, protein aggregates, and surplus macromolecules—for degradation within the vacuole.

Despite the crucial role of selective autophagy in plant resilience, the identification and characterization of SAR repertoires remain limited. To uncover novel selective autophagy players in plants, we conducted a comparative interactome screen across five species, leading to the identification of CESAR, a highly conserved protein that we characterized as a novel SAR.

Our results revealed that CESAR is essential for heat stress tolerance and survival under proteotoxic stress in *Arabidopsis thaliana*. We propose that CESAR is involved in the autophagic clearance of ubiquitinated protein aggregates. Additionally, we found that CESAR associates *in vivo* with NBR1, a well-known aggrephagy receptor. Further analysis revealed crosstalk between CESAR and NBR1, suggesting they work together to ensure efficient cargo degradation.

Our findings uncover a novel selective autophagy pathway and establish CESAR as a key regulator of protein quality control and cellular homeostasis in plants.

ZUSAMMENFASSUNG

Steigende Temperaturen, die durch den Klimawandel verursacht werden, stellen eine erhebliche Herausforderung für das Pflanzenwachstum und -überleben dar und bergen ein beträchtliches Risiko für die globale Ernährungssicherheit. Um die zelluläre Homöostase unter biotischen und abiotischen Stressbedingungen aufrechtzuerhalten, haben Pflanzen komplexe Mechanismen zur Kontrolle der Proteinqualität entwickelt, einschließlich der selektiven Autophagie. Dieser Prozess wird durch selektive Autophagie-Rezeptoren (SARs) vermittelt, die spezifische zelluläre Komponenten wie beschädigte Organellen, Proteinaggregate und überschüssige Makromoleküle erkennen und für den Abbau in der Vakuole markieren.

Trotz der entscheidenden Rolle der selektiven Autophagie für die Widerstandsfähigkeit von Pflanzen sind die Identifizierung und Charakterisierung von SAR-Repertoires bisher begrenzt. Um neue Akteure der selektiven Autophagie in Pflanzen zu entdecken, führten wir einen vergleichenden Interaktom-Screen über fünf Arten hinweg durch, was zur Identifizierung von CESAR führte, einem hochkonservierten Protein, das wir als neuartigen SAR charakterisierten.

Unsere Ergebnisse zeigten, dass CESAR für die Hitzestress-Toleranz und das Überleben unter proteotoxischem Stress in *Arabidopsis thaliana* essenziell ist. Wir schlagen vor, dass CESAR an der autophagischen Entfernung von ubiquitinierten Proteinaggregaten beteiligt ist. Darüber hinaus fanden wir heraus, dass CESAR in vivo mit NBR1, einem bekannten Rezeptor der Aggrephagie, assoziiert. Weitere Analysen zeigten eine Wechselwirkung zwischen CESAR und NBR1, was darauf hindeutet, dass sie zusammenarbeiten, um eine effiziente Frachtdegradation sicherzustellen.

Unsere Ergebnisse decken einen neuartigen Weg der selektiven Autophagie auf und etablieren CESAR als einen zentralen Regulator der Proteinqualitätskontrolle und der zellulären Homöostase in Pflanzen.

ABBREVIATIONS

ADS – Aim Docking Site

AIM – ATG8 Interacting Motif

AP-MS – Affinity Purification Mass Spectrometry

At – *Arabidopsis thaliana* or *A.thaliana*

B - Bortezomib

C - Control

CESAR – CUE containing SAR

CoIP – Co-immunoprecipitation

CUE – Coupling of Ubiquitin to ER degradation

D - DMSO

ER – Endoplasmic Reticulum

HS – Heat stress

LIR – LC3 Interacting Region

SA – Selective Autophagy

SAR / SARs – Selective Autophagy Receptor/s

TUBEs – Tandem Ubiquitin Binding Entities

UBA – Ubiquitin Associated Domain

UPS – Ubiquitin Proteasome System

WB – Western Blot

WT – *wild-type*

INTRODUCTION

Plants are constantly exposed to a wide range of environmental conditions. Both biotic and abiotic stresses limit plant growth, development, and productivity, ultimately reducing yield. To cope with these challenges, plants have evolved sophisticated molecular mechanisms to sense, respond, and adapt to stress (Nawaz et al., 2023). Among these mechanisms, autophagy plays a critical role. It is induced by various abiotic and biotic stresses, and mutants with impaired autophagy exhibit heightened sensitivity to such conditions, along with reduced growth, decrease in fitness, and early leaf senescence (Janse Van Rensburg et al., 2019) (Figure 1).

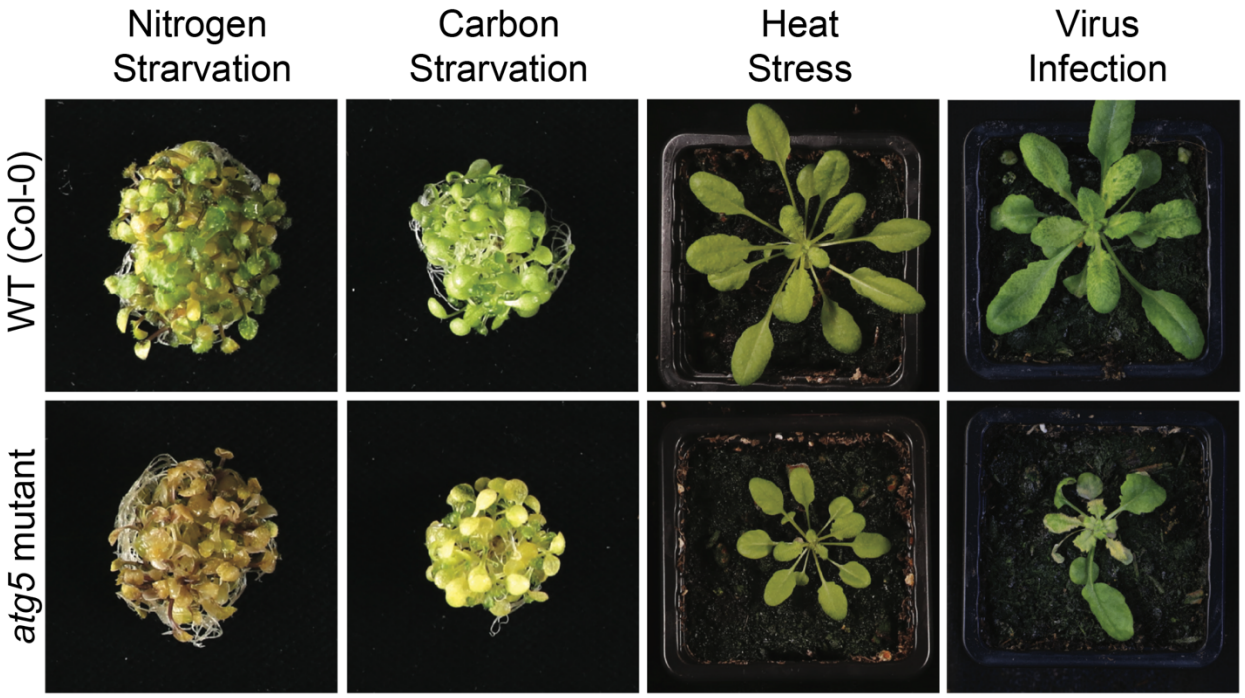

Figure 1. Autophagy deficient mutants are hypersensitive to stress. *Arabidopsis thaliana* WT plants are shown in the upper panel and autophagy deficient mutant plants in the lower panel. For nutrient starvation, bushes of seedlings are shown whereas for heat stress and virus infection, rosettes are shown (modified from Gross et al., 2024).

One of the major abiotic stressors is elevated temperature, which can cause protein misfolding and the formation of non-specific aggregates. Heat stress often results in significant morphological and phenotypic changes, such as cell cycle arrest and slowed growth, primarily due to protein aggregation and disruptions in protein homeostasis.

Beyond proteins, heat stress also affects cell membranes and RNA regulatory mechanisms, further compromising cellular function (Richter et al., 2010).

Much of what is known about the heat stress response in plants comes from studies on model species such as *Arabidopsis thaliana*, tomato, and rice (Zhao et al., 2020). Similar to other organisms, heat stress leads to the accumulation of misfolded proteins and organelle damage in plants, which results in disrupted growth and homeostasis, (Kan et al., 2023). To restore protein and cellular homeostasis, and support post-stress recovery, plants rely on selective autophagy. This process degrades and recycles damaged organelles, misfolded proteins and protein aggregates, thereby mitigating stress-related damage. The specificity of selective autophagy is mediated by selective autophagy receptors (SARs), which recognize and bind specific cargo, recruit the autophagy machinery, and facilitate its sequestration into autophagosomes for degradation in the vacuole (Gubas and Dikic, 2022).

In *Arabidopsis thaliana*, NBR1 was the first SAR identified in plants (Svenning et al., 2011). It shares homology with the mammalian SARs p62 and NBR1, and is involved in targeting ubiquitinated protein aggregates formed under heat stress through a process known as aggrephagy (Jung et al., 2020a; Svenning et al., 2011; Zhou et al., 2013). While the mechanisms of selective autophagy in mammalian cells, including the removal of protein aggregates and damaged organelles, are well-studied, much less is known about the mechanistic details of this process in plants. This knowledge gap is partly due to the limited number of SARs identified in plants.

Identifying and characterizing novel SARs, is essential to understanding how plants fine-tune their cellular contents in response to environmental challenges. Gaining insights into the molecular mechanisms of selective autophagy in plant stress responses will help uncover the adaptive strategies plants use to contend with environmental stressors. Furthermore, plants provide a valuable model for studying heat stress and selective autophagy at the organismal level in a multicellular organism.

The discovery of new selective autophagy pathways will not only deepen our understanding of plant stress responses but also identify potential targets for enhancing stress resistance and improving crop yields. This is particularly critical in the context of climate change, where rising temperatures threaten plant survival and food security.

LITERATURE REVIEW

The dynamic nature of the cellular proteome

The cellular proteome represents a complex network of structural and regulatory systems that demands constant monitoring and adjustment to adapt to the cell's dynamic needs (Harper and Bennett, 2016). During dynamic cellular processes, protein levels frequently fluctuate over time. These changes can result from alterations in protein production rates, degradation rates, or a combination of both (Ross et al., 2021). The continuous process of protein synthesis and degradation, and the balance between the two, is referred to as protein turnover and it's regulated in response to cell-intrinsic and environmental signals (Hinkson and Elias, 2011; Rolfs et al., 2021).

Molecular chaperons as part of the proteostasis network

In order to function properly in biological processes, most proteins need to achieve a defined three-dimensional structure and stay properly folded throughout their lifespan (Hipp et al., 2019). To fold appropriately and efficiently within a timeframe that is relevant for biological processes a significant portion of newly synthesized proteins depend on molecular chaperones (Ellis, 1987; Hartl and Hayer-Hartl, 2009). Molecular chaperones are proteins that interact with and stabilize partially folded or unstable conformations of other proteins. Through regulated cycles of binding and release, they assist these proteins in achieving their proper functional outcomes *in vivo*, such as correct folding, assembly into oligomeric complexes, transport to specific subcellular locations, or targeted degradation (Hendrick and Hartl, 1993).

The native conformation of proteins can be influenced by modifications or alterations in the cellular environment (Weids et al., 2016). Conformational flexibility is essential for

protein function, however, abnormal conformations and misfolding, usually induced by environmental stress or genetic mutations, can expose hydrophobic regions of polypeptides, triggering aberrant protein-protein interactions and protein aggregation (Hartl et al., 2011; Vabulas et al., 2010). To prevent protein aggregation, molecular chaperones recognize and act upon misfolded and non-native proteins (Kim et al., 2013). Additionally, chaperones also have the ability to compartmentalize misfolded proteins within specific cellular regions, reducing their detrimental effects (Pilla et al., 2017; Sontag et al., 2014). If protein aggregates form, specific chaperones with disaggregase activity act to solubilize them. The released polypeptides are then directed either toward refolding or degradation (Nillegoda and Bukau, 2015).

The molecular mechanisms that maintain protein homeostasis and proteome balance are collectively called proteostasis network (PN) (Jayaraj et al., 2020). In addition to managing protein folding, the proteostasis network facilitates the removal of excess and misfolded proteins through autophagy or proteasome-mediated degradation (Hipp et al., 2019) (See next section). When these mechanisms fail, misfolded proteins and aggregates accumulate, disrupting protein function, impairing organelle activity, and causing cellular toxicity (Kandel et al., 2024)

Ubiquitin-Proteasome-System and Selective Autophagy are major degradative systems

To preserve cellular and organismal health, eukaryotes have developed quality control mechanisms that isolate and degrade malfunctioning proteins, lipids, and organelles (Henne, 2021). Two major pathways involved in this process are the ubiquitin-proteasome system (UPS) and selective autophagy (SA) (Pohl and Dikic, 2019).

The UPS is responsible for degrading short-lived, damaged, or soluble misfolded proteins through the proteasome, a self-compartmentalized protease (Marshall and Vierstra, 2019). Proteins targeted for degradation are first tagged with ubiquitin, a process mediated by three classes of enzymes: E1s (activating enzymes), E2s (conjugating

enzymes), and E3s (ligases) (Su et al., 2020). Once ubiquitinated, these proteins are directed to the proteasome for breakdown (Su et al., 2020).

Ubiquitination can occur in several ways: monoubiquitination (a single ubiquitin attached to one lysine), multiubiquitination (single ubiquitin molecules attached to multiple lysines), or polyubiquitination (ubiquitin chains formed by further ubiquitination of the initial ubiquitin) (Song and Luo, 2019). Polyubiquitination can involve one of ubiquitin's seven lysines or its amino-terminal methionine (M1), resulting in eight distinct linkage types: K6, K11, K27, K29, K33, K48, K63, and M1 (Chen et al., 2019). Among these, K48 and K63 linkages are the most abundant in both animals and plants (Raffeiner et al., 2023). For proteasomal degradation, K48-linked chains are the canonical signal (Thrower, 2000).

Selective autophagy also relies on ubiquitin as a key signal for recognition of certain targets (Vainshtein and Grumati, 2020). K63-linked ubiquitin chains are commonly associated with autophagy, as well as other non-proteolytic processes, such as endosomal trafficking and DNA repair (Dósa and Csizmadia, 2022; Ikeda and Dikic, 2008)

Selective autophagy is responsible for the degradation of specific cytoplasmic components, such as dysfunctional macromolecular complexes, protein aggregates, organelles, and pathogens (Lamark and Johansen, 2021). These components are recognized by specific receptors and sequestered into a double-membrane vesicle called the autophagosome (Marshall and Vierstra, 2019). The autophagosome then fuses with lysosomes in metazoans or vacuoles in fungi and plants for degradation (Ohsumi, 2014).

Since the ubiquitin code operates with greater complexity than previously recognized classical pathways, identifying the presence or specific type of ubiquitin chain linkages alone is insufficient to fully predict whether a substrate will undergo proteasomal or autophagic degradation (Ji and Kwon, 2017). Beyond ubiquitin signaling, the choice between the UPS and autophagy for substrate degradation depends predominantly on the physicochemical properties of the target (Raffeiner et al., 2023). The UPS primarily handles individual, unfolded polypeptides that can pass through the narrow proteasome channel, whereas autophagy is better suited for degrading larger cytosolic structures (Pohl and Dikic, 2019; Schreiber and Peter, 2014).

Even though the UPS and autophagy have different substrates, recent studies have revealed crosstalk between these two pathways. In mammalian cells and *Drosophila melanogaster*, proteasome inhibition has been shown to induce autophagy, suggesting that autophagy can compensate for impaired proteasomal degradation (Iwata et al., 2005; Pandey et al., 2007; Schreiber and Peter, 2014; Wang et al., 2019). In contrast, autophagy inhibition in mammalian cells leads to the accumulation of proteasomal substrates due to delayed delivery to proteasome proteases (Korolchuk et al., 2009).

Therefore, the precise function and spatiotemporal coordination of these two degradative pathways, both in relation to each other and other protein quality control systems, such as chaperones, are crucial for maintaining cellular homeostasis and ensuring an effective response to stress.

Selective autophagy receptors orchestrate selective autophagy

Autophagosome biogenesis

Autophagy is an evolutionarily conserved mechanism, and apart from degrading of cytoplasmic materials, it also functions to recycle them, generating new building blocks for cellular renovation and homeostasis (Mizushima and Komatsu, 2011).

This process can be categorized into two primary types based on specificity. The first is 'bulk' or 'non-selective' autophagy which, in response to starvation, captures and degrades portions of the cytoplasm in an indiscriminate manner, including organelles and macromolecular complexes. The second is 'selective' autophagy, which targets specific cargos for degradation, such as those detrimental for cellular health (Vargas et al., 2023). Both forms fall under the broader category of macroautophagy, the primary type of autophagic process, which involves the sequestration of substrates into autophagosomes (Feng et al., 2014).

The molecular mechanisms of autophagy depend on the stepwise assembly of a complex, multi-component system involving around 40 evolutionarily conserved ATG genes. This highly regulated process is controlled by conserved kinase signaling

pathways that respond to both environmental and cellular stressors. Various subcomplexes within the autophagy machinery interact to construct the autophagosome, recognize the cellular components designated for degradation, and ultimately deliver them to the lysosome or the vacuole for breakdown (Gross et al., 2025).

The formation of autophagosomes begins with membrane nucleation, driven by the induction and assembly of the initiation complex, which facilitates the generation of the phagophore, the precursor to the autophagosome (Nakatogawa, 2020). The nucleation process involves forming a membrane contact site between small membrane precursors, originating from ATG9A-containing vesicles, and a specific subregion of the endoplasmic reticulum (Gómez-Sánchez et al., 2018; Sawa-Makarska et al., 2020). ATG2 is a key protein in membrane contact sites, facilitating lipid transfer between ATG9 vesicles and the endoplasmic reticulum (ER) membrane. Alongside lipid production in the ER, ATG2A helps deliver lipids to ATG9A-positive membranes. Once there, ATG9A's scramblase activity ensures these lipids are evenly distributed between the two layers of the expanding phagophore (Adriaenssens et al., 2022). The initiation complexes ULK1/2 (Atg1 complex in yeast) and the the PI3KC3-C1 activate and regulate the establishment of the membrane contact site and the expansion of the isolation membrane (also known as phagophore) (Nishimura and Tooze, 2020).

As the process progresses, the elongation of the phagophore membrane involves the coordinated activity of PI3P-binding WIPI proteins, the Atg8-family and Atg12 conjugation systems (including Atg3, Atg4, Atg5, Atg7, Atg10, Atg12, Atg16, LC3s, and GABARAPs) (Hurley and Young, 2017). During this process, the ATG8 family of proteins, are covalently linked to phosphatidylethanolamine and the membrane extensions become decorated with the resulting lapidated ATG8. To support the elongation and proper engulfment of the isolation membrane, additional membranes are delivered to it. Eventually, the isolation membrane seals to form autophagosomes, which can reach a diameter of up to 1 μm (Vargas et al., 2023).

Selective Autophagy Receptors

In selective autophagy, autophagosome formation takes place at the site of the cargo (Turco et al., 2020). Selective autophagy receptors (SARs), also known as cargo adaptors or cargo receptors, are proteins that bind to and specify the cytoplasmic components destined for degradation through autophagy (Gatica et al., 2018a). These receptors bridge the ATG8 family of proteins, associated with the phagophore membrane, with the target cargo, enabling the selective degradation process (Birgisdottir et al., 2013) (Figure 2). The interaction between SARs and ATG8 proteins, is mediated by an ATG8-interacting motif or LC3-interacting region (AIM/LIR) (Noda et al., 2010) (Figure 3). This motif consists of an aromatic residue followed by two variable amino acids and an aliphatic residue (W/F/Y-x-x-L/I/V) (Noda et al., 2010).

Selective autophagy occurs in different ways depending on the specific target, but all forms require the involvement of a SAR. Thus, SARs are main players of selective autophagy (Gatica et al., 2018b). The SAR may be an integral component of the cargo, such as Atg32 at the mitochondria (Kanki et al., 2009), or can bind the cargo via specific signals associated to the cargo, most commonly ubiquitin linkages (Gatica et al., 2018b).

Over the past few years, several forms of selective autophagy have been identified, each determined by the specificity of its corresponding SAR or group of SARs. Among these, aggrephagy, the autophagic degradation of protein aggregates, is one of the most extensively studied forms of selective autophagy (Lamark and Johansen, 2012). Additionally, numerous studies have demonstrated SAR-mediated selective degradation of various organelles, including mitochondria (mitophagy), peroxisomes (pexophagy), lysosomes (lysophagy), the endoplasmic reticulum (ER-phagy), ribosomes (ribophagy), and even parts of the nucleus (nucleophagy), among others (Li et al., 2021).

Beyond organelles, macromolecular complexes such as the proteasome (proteophagy) (Goebel et al., 2020; Marshall et al., 2015; Marshall and Vierstra, 2019) and the nuclear pore complex (NPC-phagy) (Lee et al., 2020; Tomioka et al., 2020) have also been shown to undergo selective autophagic degradation. Furthermore, as part of the immune response, cells can target and degrade intracellular pathogens through a process known

as xenophagy (Mao and Klionsky, 2017). Other forms of selective autophagy, such as ferritin degradation (ferritinophagy) (Mancias et al., 2014) have also been reported.

Although SARs have different cargos and different forms of activation, SARs share the same machinery that forms the sequestering membrane and are degraded along their cargos in an autophagy dependent manner (Germain et al., 2024).

Aggrephagy receptors in mammalian cells

The majority of known aggrephagy receptors have been identified and characterized in mammalian cells, offering important insights into the underlying mechanisms of the process. The primary aggrephagy pathway is initiated by the coordinated action of the cargo receptors p62 (also known as SQSTM1) and the sequestosome-like receptor (SLR) NBR1, with ubiquitylation of cargo proteins acting as the main selective trigger for the pathway (Bauer et al., 2023).

The traditional view held that selective autophagy receptors are recruited to large, pre-existing protein aggregates to facilitate their tethering to autophagosome membranes. However, latest data indicates that cargo receptors, such as p62 and NBR1, can target misfolded proteins before large-scale aggregation occurs by sequestering them into dynamic condensates (Adriaenssens et al., 2022).

Both p62 and NBR1 possess UBA domains that bind ubiquitin and PB1 domains that mediate oligomerization (Lamark et al., 2003; Long et al., 2010; Walinda et al., 2014). The PB1 domain of p62 allows it to oligomerize and interact with the PB1 domain of NBR1, forming hetero-oligomeric complexes (Lamark et al, 2003). However, NBR1 cannot oligomerize on its own due to the absence of one oligomerization interface (Ciuffa et al., 2015; Lamark et al., 2003). Instead, NBR1 supports p62 cargo condensation with its high-affinity UBA domain, which binds ubiquitin more strongly than the UBA domain of p62 (Kirkin et al., 2009; Lamark et al., 2003; Turco et al., 2021).

The hetero-oligomer formed by p62 and NBR1 sequesters ubiquitinated proteins into liquid-like, membraneless condensates via liquid–liquid phase separation (Bauer et al., 2023; Vargas et al., 2023). The ability of p62 to oligomerize is essential for its receptor function and for directing the isolation membrane to ubiquitinated cargo, underscoring the cooperative role of p62 and NBR1 in the formation of condensates and the execution of aggrephagy (Vargas et al., 2023).

Following p62–NBR1-dependent condensate formation, additional factors like TAX1BP1 are recruited to facilitate autophagy (Bauer et al., 2023). The recruitment of TAX1BP1 to p62 condensates is regulated by GABARAP proteins, which compete with TAX1BP1 for binding to NBR1, and by its interaction with ubiquitin, which has been suggested to require a threshold concentration of ubiquitin for effective recruitment (Bauer et al., 2024). Once TAX1BP1 is recruited via its interaction with NBR1, it plays a central role in initiating autophagosome formation at the condensates to ensure the clearance of the ubiquitnated cargo (Ohnstad et al., 2020; Sarraf et al., 2020; Turco et al., 2021). Together, p62, NBR1, and TAX1BP1 coordinate the transition from condensate formation to autophagosome assembly, enabling aggrephagy.

In addition to p62, NBR1, and TAX1BP1, Tollip was identified a SAR that binds to ubiquitin via its CUE-domain, and mediates the autophagic degradation of cytotoxic protein aggregates, including those formed by expanded polyQ isoforms of huntingtin (Lu et al., 2014). Apart from ubiquitin-binding selective autophagy receptors, CCT2 was recently identified as an aggrephagy receptor that plays a role in clearing solid protein aggregates in cells and mouse brain in a ubiquitin-independent manner. In addition, CCT2 does not depend on p62, NBR1 and TAX1BP1. The accumulation of aggregation-prone proteins induces CCT2 to transition from a chaperone subunit to an autophagy receptor by promoting its monomerization, which activates its autophagic function (Ma et al., 2022).

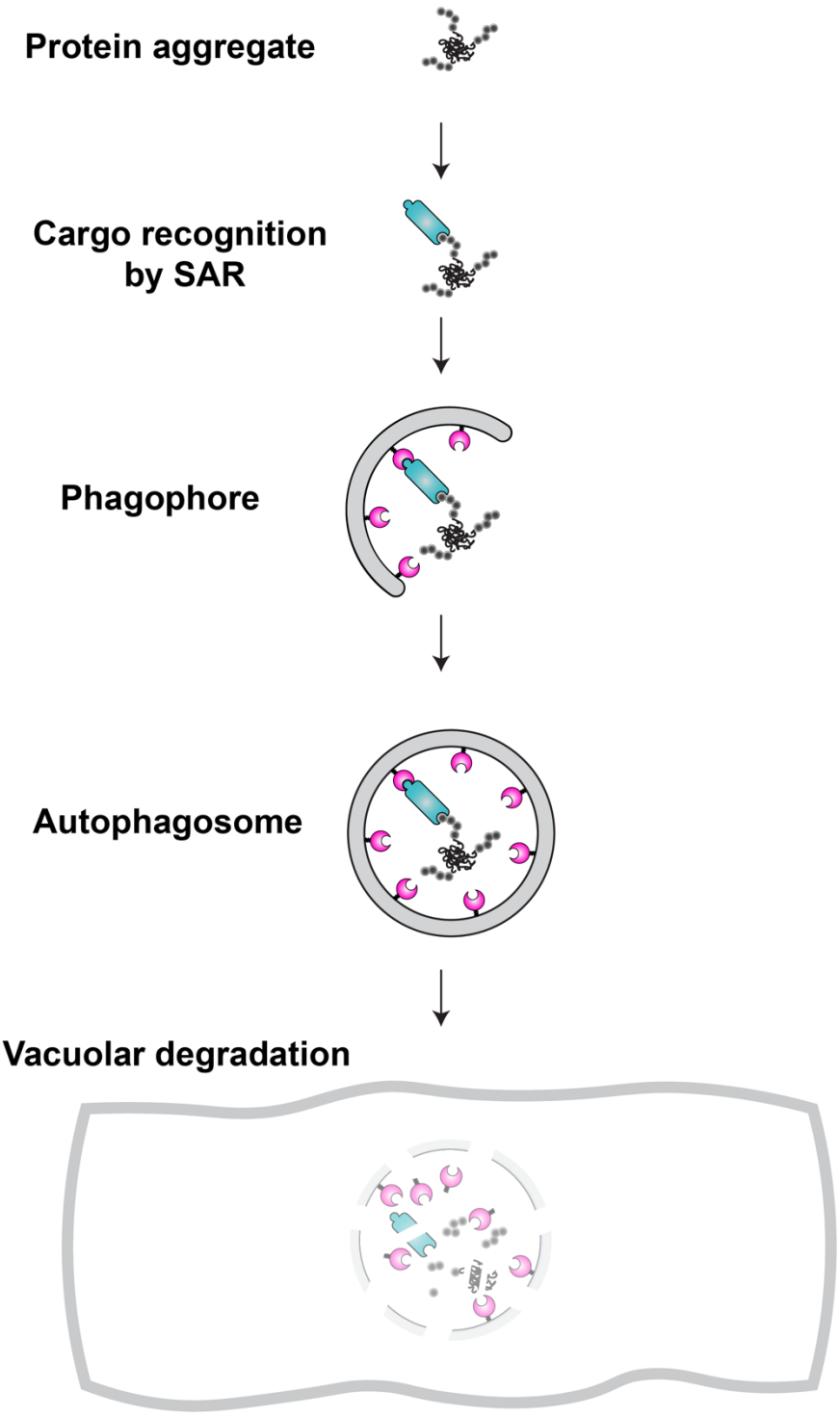

Figure 2. Selective Autophagy. Selective Autophagy Receptors (SARs) recognize and bind specific cargo, such as protein aggregates, targeting them for degradation. SARs recruit the autophagy machinery to assemble a phagophore around the cargo, which matures into an autophagosome. The autophagosome is then transported to the vacuole for degradation.

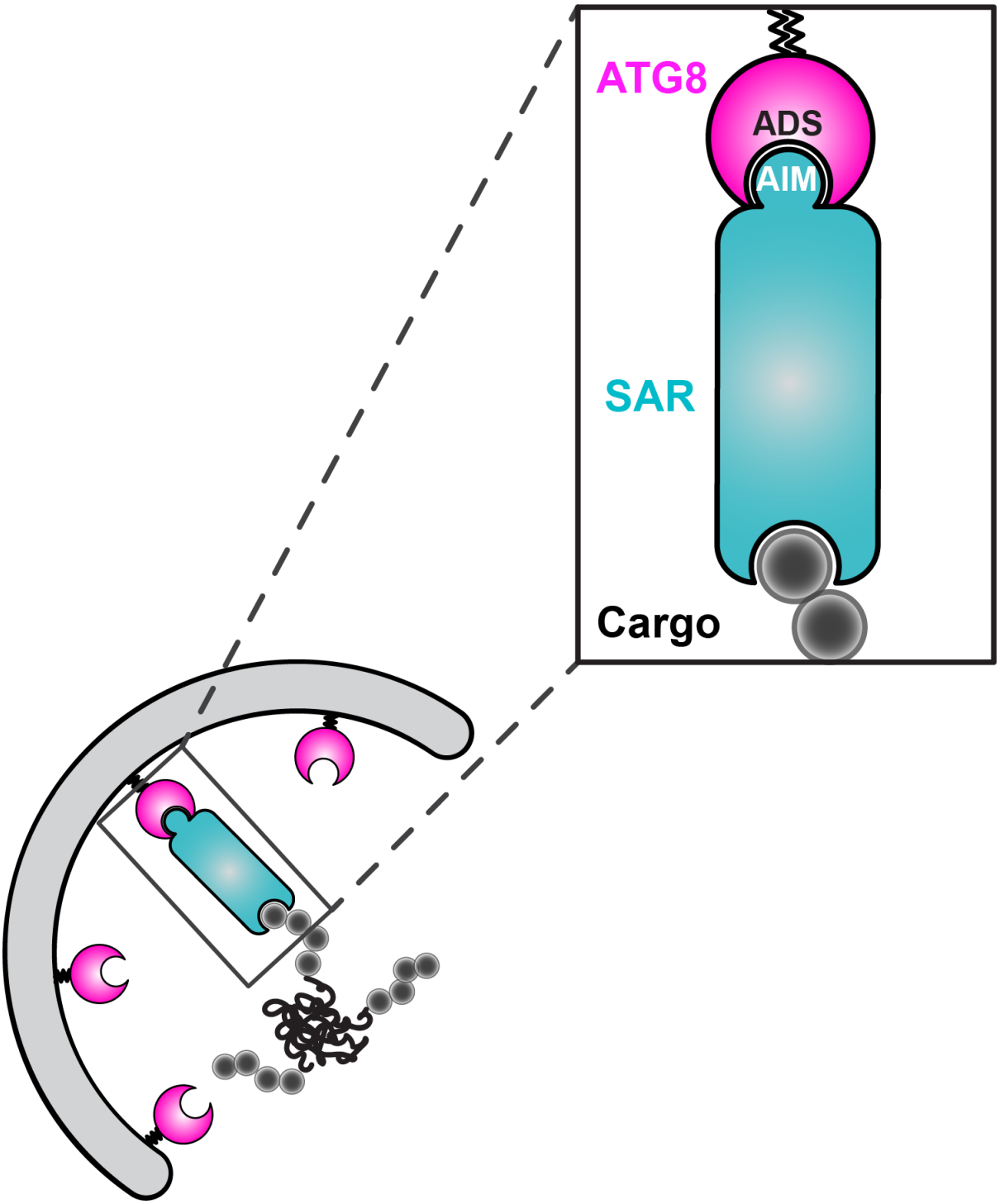

Figure 3. Selective Autophagy Receptors (SARs) link ATG8 proteins to the cargo. SARs contain an ATG8-Interacting Motif (AIM), which binds to a hydrophobic pocket of ATG8 proteins, known as the AIM-docking site (ADS).

Aggrephagy receptors in plants

NBR1 is conserved across all eukaryotic kingdoms, whereas p62 is specific to metazoans. Non-metazoan organisms typically possess a single NBR1 homolog, while metazoans may have p62 alone or in combination with NBR1 (Svenning et al., 2011).

The *Arabidopsis thaliana* NBR1 homolog (AtNBR1) shares structural and sequence similarities with mammalian NBR1 but also exhibits functional traits comparable to p62. The first study to explore selective autophagy in plants and the role of AtNBR1 as a selective autophagy receptor was conducted by Svenning and colleagues. This study demonstrated that AtNBR1 contains two UBA domains, with only the C-terminal UBA2 domain capable of binding ubiquitin. It also features a conserved AIM motif (WDPI), located between the two UBA domains, which mediates its interaction with ATG8 (Svenning et al., 2011).

Similar to p62, AtNBR1 forms homopolymers via its PB1 domain at the N-terminus. While polymerization enhances AtNBR1's co-precipitation with AtATG8 proteins, the interaction itself is independent of polymerization. In vivo, AtNBR1 colocalizes with AtATG8A, and its AIM motif is essential for vacuolar delivery. Additionally, AtNBR1 accumulates in autophagy-deficient plants, supporting its role as a substrate for selective autophagy (Svenning et al., 2011).

Later, Zhou and colleagues identified NBR1 as an ATG8 interactor through yeast two-hybrid assays using an Arabidopsis cDNA prey library. To investigate the function of NBR1, two *nbr1* knockout mutants were isolated. These mutants exhibited sensitivity to various abiotic stresses, including heat, oxidative, salt, and drought stress, but showed no significant phenotype under carbon starvation or during plant senescence (Zhou et al., 2013) (Figure 4A).

Furthermore, the number of NBR1-GFP puncta in transgenic lines increased in response to heat stress. Notably, under heat stress, NBR1 was found to accumulate in the insoluble fraction, and *nbr1* mutants displayed an accumulation of insoluble ubiquitinated proteins, suggesting the presence of protein aggregates. This study proposed that NBR1 may play

a role in targeting ubiquitinated protein aggregates for degradation under stress conditions (Zhou et al., 2013).

Importantly, Jung and colleagues used an aggregation prone substrate named GFP–FL2ΔSP in *Arabidopsis thaliana in vivo and* demonstrated its co-localization with NBR1 puncta and its subsequent vacuolar degradation via NBR1-mediated autophagy (Figure 4B). These findings further suggest that NBR1 acts as an aggrephagy receptor, playing a crucial role in maintaining proteostasis under both heat stress and normal conditions (Jung et al., 2020a).

In addition to its role as an aggrephagy receptor, recent studies have demonstrated that NBR1 is involved in the autophagic removal of photodamaged chloroplasts (Lee et al., 2023) and the degradation of TOC proteins at the chloroplast outer envelope membrane under UV-B radiation and heat stress (Zhang and Ling, 2024).Furthermore, during the recovery phase following heat stress, NBR1 mediates the degradation of HSP90.1 and its interacting partner ROF1, contributing to the regulation of heat stress memory (Thirumalaikumar et al., 2021).

Beyond these functions, NBR1 plays a role in plant immunity by targeting specific viral components for degradation (Hafrén et al., 2017) and is also involved in lateral root formation by mediating the degradation of the transcription factor ARF7 (Ebstrup et al., 2024).

Aside from NBR1, no other protein has been conclusively validated as an aggrephagy receptor in plants. Considering the complexity of aggrephagy networks in mammalian cells, it is evident that our understanding of aggrephagy mechanisms in plants remains limited and incomplete.

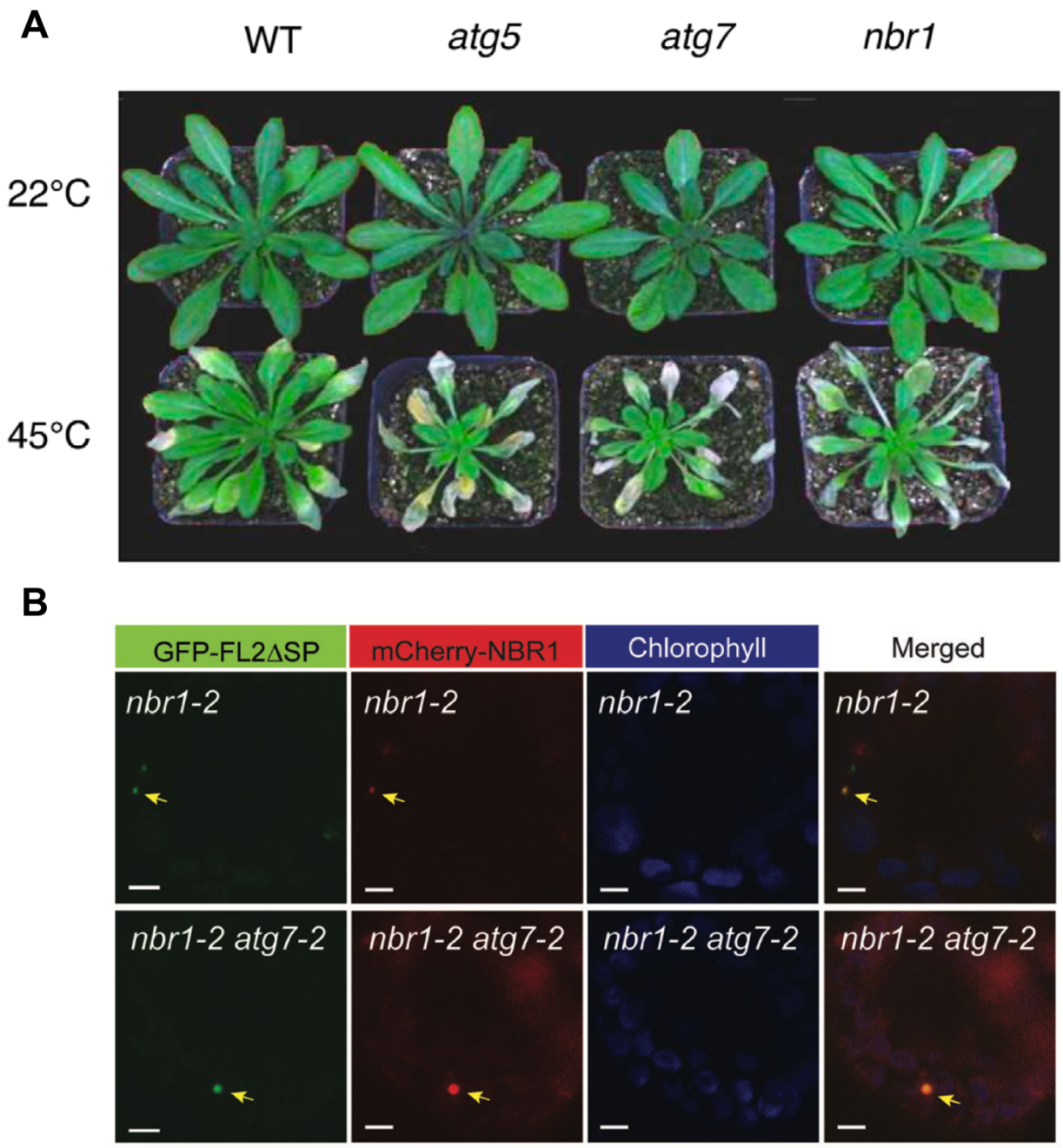

Figure 4. (A) *nbr1* mutant is sensitive to heat stress. Five weeks old Arabidopsis Col-0 wild type (WT), atg5 and nbr1 mutant plants incubated at 22°C and 45°C for 10 hours and recovered at room temperatue for 3 days (Zhou et al., 2013). **(B) Protein aggregate reporter colocalizes with NBR1.** Confocal fluorescence images of mesophyll cells from *nbr1-2* and *atg7-2 nbr1-2* plants co-expressing GFP-FL2ΔSP and mCherry-NBR1. Arrows highlight GFP–FL2ΔSP puncta that colocalize with the mCherry–NBR1 fluorescence signal. Chlorophyll autofluorescence is displayed in blue. Scale bars: 5 μm (Jung et al., 2020b). *Figures taken from the cited manuscripts*.

RESEARCH AIMS

The overarching aim of this study is to uncover and characterize novel selective autophagy receptors that regulate protein quality control in plants during heat stress recovery.

This study is divided in four parts:

Part 1: Identification of CESAR as an AIM-dependent ATG8 interactor

Part 2: Characterization of CESAR as a Selective Autophagy Receptor

Part 3: The physiological role of CESAR in organismal homeostasis

Part 4: CESAR and NBR1 crosstalk

Hypothesis and aims:

Part 1: Identification of CESAR as an AIM-dependent ATG8 interactor

Hypothesis

A comparative interactome screen will identify novel SAR candidates and SA players.

Aim:

1. **Perform AP-MS coupled to peptide competition to identify ATG8A and ATG8E AIM-dependent interactors in *Arabidopsis thaliana***

   Protein extracts from transgenic *A. thaliana* lines expressing mCherry-tagged ATG8A and ATG8E will be used to generate interactome data. To identify AIM-dependent interactors, a peptide competition assay will be performed following the approach of Stephani et al. (Stephani et al., 2020). The immunoprecipitation reaction will be incubated with a synthetic peptide containing a wild-type (WT) AIM

motif, which has a high affinity for the AIM-Docking Site (ADS) in ATG8. As a control, a mutant AIM (AIM mut) peptide with low ADS affinity will be used (Figure 5). The resulting data will help identify ATG8 AIM-dependent interactions for interspecies comparative analysis.

Hypothesis

AP-MS coupled to peptide competition for ATG8 will help identify candidate SARs involved in maintaining homeostasis during heat stress in *A. thaliana*.

Aim:

2. **Identify ATG8-AIM dependent interactions enriched under heat stress in *Arabidopsis thaliana***

   Seven-day-old seedlings expressing mCherry-ATG8A or mCherry-ATG8E will be subjected to heat stress (37°C for 6 hours, followed by 4 hours of recovery at 21°C) with or without CB5083 treatment. Enrichment of ATG8-AIM-dependent interactors will be analyzed using MS data to identify potential selective autophagy receptors (SARs) and autophagy-related proteins involved in heat stress recovery.

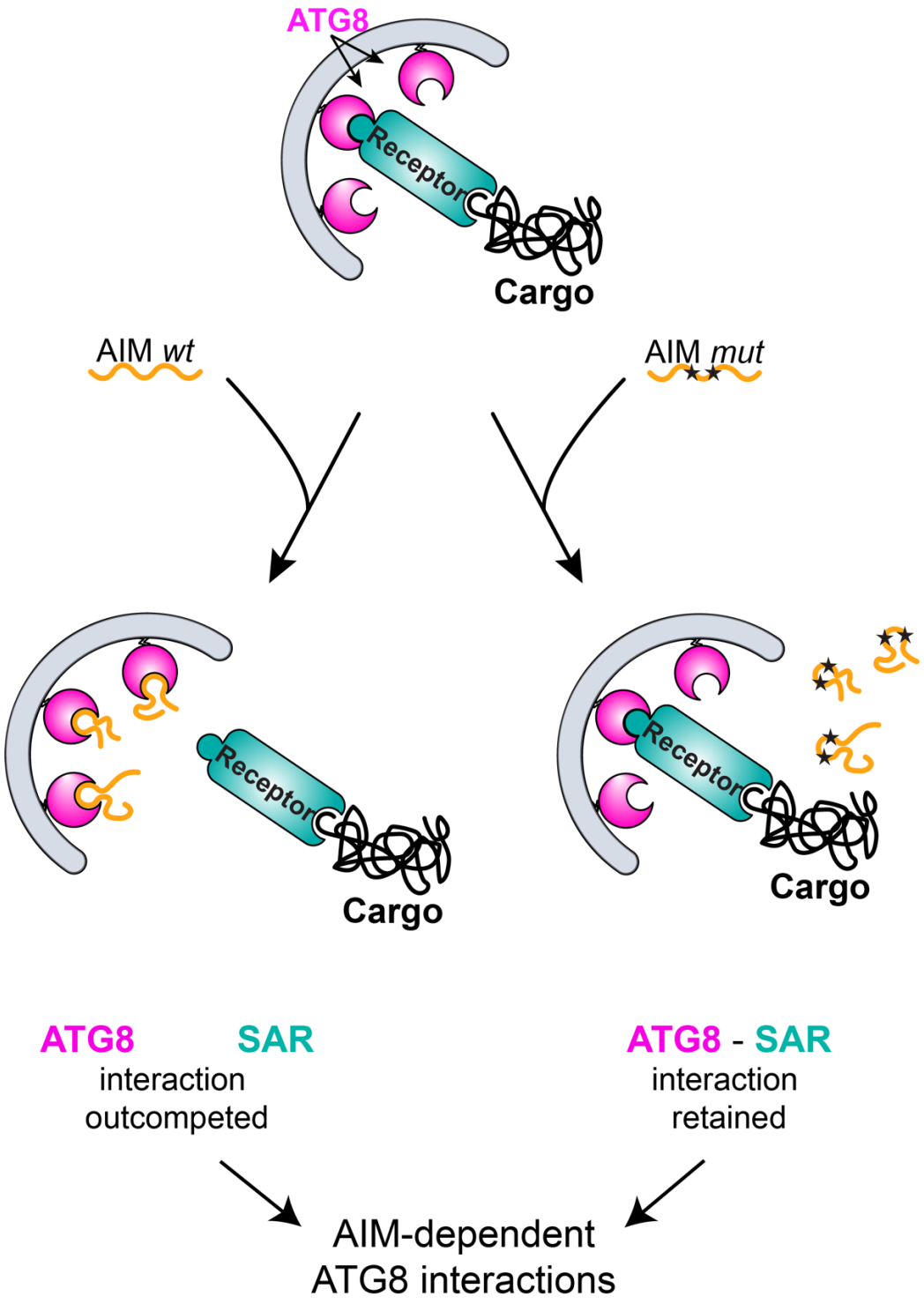

Figure 5. Schematic illustrating the peptide competition approach. The addition of the AIM wild-type (wt) peptide, which has high affinity for the ATG8 AIM-docking site (ADS), competes with AIM-dependent ATG8 interactors, including SARs. In contrast, the AIM mutant (mut) peptide, with low affinity for the ADS, has no effect. The comparison of both datasets reveals AIM-dependent ATG8 interactions.

Part2: Characterization of CESAR as a Selective Autophagy Receptor

CESAR was identified as a conserved ATG8-AIM-dependent interactor in four out of five species analyzed in the comparative approach. Additionally, CESAR1 and CESAR2 were found to be enriched as ATG8-AIM dependent interactors following heat stress treatment in *Arabidopsis thaliana*.

Hypothesis

CESAR is a conserved selective autophagy receptor involved in maintaining protein homeostasis during heat stress.

Aims:

3. **Characterize CESAR as a Selective Autophagy Receptor *in vivo***

   If CESAR functions as a SAR, it should meet the following criteria: (1) localize to autophagosomes and associate with ATG8 in an AIM-dependent manner *in vivo*, (2) undergo autophagic degradation, and (3) target specific cargo for degradation.

   3.1 Assess CESAR localization to autophagosomes and its association with ATG8 in vivo.

   Since Arabidopsis thaliana possess two copies of CESAR gene, CESAR1 and CESAR2 localization and co-localization with ATG8 will be evaluated in *A. thaliana* roots under control and heat stress conditions using confocal microscopy. Co-immunoprecipitation (co-IP) experiments with peptide competition will confirm AIM-dependent interaction between CESAR and ATG8. Transgenic lines expressing fluorescently tagged CESAR1/2 and co-expressing CESAR1/2 with ATG8 will be generated for these experiments.

3.2 Evaluate CESAR response to heat stress at the protein and mRNA levels

Changes in CESAR protein levels will be analyzed under different heat stress time courses in transgenic lines expressing CESAR-GFP under a constitutive promoter. Endogenous CESAR1/2 mRNA levels will be quantified using RT-qPCR.

3.3 Determine whether CESAR undergoes autophagic degradation

CESAR-GFP autophagic degradation will be assessed in WT and autophagy-deficient (*atg5*) backgrounds under heat stress (37°C) and proteasomal inhibition (Bortezomib). Autophagic flux experiments upon and confocal microscopy Concanamycin A treatment will be used to evaluate CESAR-GFP vacuolar degradation.

3.4 *Assess whether CESAR functions as an aggrephagy receptor*

CESAR's ability to bind ubiquitin and ubiquitinated proteins will be tested. CESAR enrichment in the insoluble protein fraction following heat stress will be analyzed. Co-localization of CESAR with protein aggregates will be assessed using an aggregate reporter (Jung et al., 2020a) and the protein aggregation assay PROTEOSTAT.

Part 3: The physiological role of CESAR in organismal homeostasis

Hypothesis 4

CESAR plays a critical role in heat stress resistance.

Aims:

4. **Assess CESAR1 and CESAR2 mRNA expression in *cesar1 cesar2* line**

   CESAR1 and CESAR2 mRNA levels will be quantified in the *cesar1 cesar2* double mutant using RT-qPCR.

5. **Determine the role of CESAR in heat stress tolerance.**

   Phenotypic assays will evaluate the sensitivity of the *cesar1 cesar2* double mutant, along with *atg5* and *nbr1* mutants, to heat stress and proteotoxic stress conditions. In addition, carbon and nutrient starvation will also be assessed.

Part 4: Functional Relationship Between CESAR and NBR1

Our previous studies suggested that CESAR and NBR1 follow similar kinetics. Additionally, CESAR and NBR1 are among the top ATG8 interactors in our interactome analysis.

Hypothesis 5

CESAR and NBR1 function in the same autophagy pathway to maintain protein homeostasis during stress.

Aims:

6. **Determine whether CESAR colocalizes with NBR1 *in vivo***

   Co-localization of CESAR and NBR1 will be assessed in *A. thaliana* roots using confocal microscopy. Transgenic lines expressing co-expressing fluorescently tagged CESAR and NBR1 will be generated for these experiments.

7. **Assess whether NBR1 influences CESAR autophagic flux.**

   Autophagic flux experiments will be performed in transgenic lines expressing CESAR2-GFP in WT and *nbr1* mutant backgrounds under heat stress and proteasomal inhibition.

METHODS

Phylogenetic analyses

To identify potential homologs of the autophagy receptor candidates across various species, profile hidden Markov models (HMMs) for MpCESAR were constructed using HMMER v3.4, as available at http://hmmer.org.

OrthoFinder v2.5.5 was employed to group the proteomes of the five species of interest (*C. reinhardtii, M. polymorpha, P. patens, N. benthamiana, and A. thaliana*) into Phylogenetic Hierarchical Orthogroups (HOGs) (Emms and Kelly, 2020) . UpSet plots were created in RStudio v2023.12.1 using the complexUpset and ggplot2 libraries (Sánchez de Medina and Nava García, et al., 2024, BioRxiv).

Plant material and molecular cloning procedures

All *A. thaliana* lines used in this study were derived from the Columbia (Col-0) ecotype, with specific lines detailed in the materials section. Previously described lines include atg5-1 (Thompson et al., 2005), nbr1-2 (Zhou et al., 2013), pUBQ::mCherry (Zhao et al., 2022), pUBQ::mCherry-AtATG8A (Zhao et al., 2022), pUBQ::mCherry-AtATG8E (Stephani et al., 2020), pUBQ::mCherry-AtATG8E/atg5-1(Stephani et al., 2020), and pUBQ::GFP-AtATG8A (Stephani et al., 2020).

The double mutant *cesar1 cesar2* was generated by crossing cesar1-1 and cesar2-1 T-DNA insertion lines obtained from SALK (SALK_112206.23.80.x and SALK_022568,

respectively). Homozygous plants were identified through genotyping PCR, with primers listed in the materials section. Stable transgenic *A. thaliana* lines were produced via Agrobacterium-mediated transformation using the floral dip method. Transgenic lines, including pRSP5::AtCESAR2-GFP in pUBQ::mCherry-AtATG8E, pRPS5::AtCESAR2-GFP in pUBQ::mCherry-AtATG8E/*atg5-1*, were generated by transforming the respective genotypes with the pGGSun-pRPS5::AtCESAR2-GFP vector. Transformants were selected on sulfadiazine-containing medium, and F1 and F3 generations were screened for AtCESAR2-GFP protein expression. Similarly, lines such as pRPS5::AtCESAR1-mCherry in Col-0 and pRPS5::AtCESAR1-mCherry in pRPS5::AtCESAR2-GFP were obtained by transforming the relevant genotypes with the pGGSun-pRPS5::AtCESAR1-mCherry vector. The transgenic lines: pRSP5::AtCESAR2-mCherry in pNBR1::GFP-AtNBR1 and pRSP5::AtCESAR2-mCherry in pUB1::GFP were generated by transforming the mentioned genotypes with pGGSun-pRPS5::AtCESAR2-mCherry. The transgenic line pRPS5::AtCESAR2-GFP in *nbr1* was generated by transforming nbr1-2 mutant with pGGSun-pRPS5::AtCESAR2-GFP vector. Transformants were selected on sulfadiazine or hygromycin-containing media, and protein expression was confirmed in F1 and F3 generations (Sánchez de Medina and Nava García, et al., 2024, BioRxiv).

Plant growth conditions and treatments

For standard *Arabidopsis thaliana* plant growth, seeds were sterilized using vapor-phase sterilization (90% sodium hypochlorite and 10% HCl) and sown on a water-saturated peat-based substrate (Klasmann Substrat 2, Klasmann-Deilmann GmbH, Geeste, DE). A solution of *Bacillus thuringiensis* (Gnatrol, Valent BioSciences, Libertyville, IL, USA) was applied as a preventative measure against fungus gnats. Lighting was provided by a custom-designed, multi-channel LED system developed in collaboration with RHENAC GreenTec AG (Germany), optimized for uniform light distribution. Plants were grown at 21ºC under a 16-hour light/8-hour dark photoperiod with a light intensity of 165 µmol m^{-2} s^{-1} (PPFD). The LED channels used included 400 nm, white 4500K, 660 nm, and 730 nm, resulting in the following spectral composition: 22% PPF-Blue (400–500 nm), 31% PPF-Green (500–600 nm), and 47% PPF-Red (600–700 nm). Additionally, far-red light

(PPF-NIR; 700–780 nm) was supplemented at 17% of PPFD, with a red-to-far-red ratio of 1:0.35.

For in vitro seedling growth, *A. thaliana* seeds were sterilized in 70% ethanol with 0.05% SDS for 15 minutes, rinsed twice with absolute ethanol, and air-dried on sterile paper.

All heat stress (HS) assays in this study were conducted at 37ºC in a temperature-controlled chamber (Percival CU-36L4, SN: 8287.01.06C) under fluorescent lighting with an intensity of 140 µmol m^{-2} s^{-1} and 65% humidity. For affinity purification experiments, approximately 16 mg of seeds per genotype were sown in 250 mL Erlenmeyer flasks containing 90 mL of liquid ½ MS salts (Duchefa) with 1% sucrose. Seeds were stratified in the dark at 4ºC for 48 hours, then grown under a 16-hour light/8-hour dark photoperiod with 50 µmol m^{-2} s^{-1} light intensity while being gently shaken for 7 days. For affinity purification, 7-day-old seedlings were incubated at 37ºC for 6 hours, followed by a 4-hour recovery in fresh liquid ½ MS salts with 1% sucrose, either with 50 µM CB5083 (BIOCAT GmbH; dissolved in DMSO) or an equivalent volume of DMSO as a control.

For protein extraction, co-immunoprecipitation, and protein content analysis, seeds were sown in 12-well plates containing liquid ½ MS salts with 1% sucrose, stratified in the dark at 4ºC for 48 hours, and grown under a 16-hour light/8-hour dark photoperiod with 50 µmol m^{-2} s^{-1} light intensity while being gently shaken for 7 days.

For co-immunoprecipitation experiments, 7-day-old seedlings were incubated at 37ºC for 6 hours, followed by a 4-hour recovery in fresh liquid ½ MS salts with 1% sucrose, either with 50 µM CB5083 (BIOCAT GmbH; dissolved in DMSO) or an equivalent volume of DMSO. Control samples were maintained under standard conditions for 6 hours, followed by a 4-hour recovery in fresh liquid ½ MS salts with 1% sucrose.

For protein content analysis during HS, 7-day-old seedlings were incubated at 37ºC for 1 to 4 hours, followed by a 1 to 4-hour recovery under control conditions. For autophagic flux experiments during HS, 7-day-old seedlings were incubated at 37ºC for 4 hours, followed by either a 4-hour recovery in fresh liquid ½ MS medium or a 20-hour recovery in liquid ½ MS medium containing 1 µM Concanamycin A (ConA; CAS 80890-47-7; Santa

Cruz) or an equivalent volume of DMSO. For TUBE-pulldown experiments, 7-day-old seedlings were incubated at 37ºC for 4 hours, followed by a 4-hour recovery in fresh liquid ½ MS medium under control conditions. For aggregate isolation and fractionation experiments, 7-day-old seedlings were incubated at 37ºC for 4 hours, followed by either a 4-hour or 20-hour recovery in fresh liquid ½ MS medium under control conditions.

For protein content analysis after Bortezomib treatment, 7-day-old seedlings were incubated in liquid media containing either DMSO or 50 µM Bortezomib (Santa Cruz; CAS 179324-69-7) for 4 hours under control conditions, followed by a 1 to 4-hour recovery in fresh media. For autophagic flux experiments after Bortezomib treatment, 7-day-old seedlings were incubated with either 50 µM Bortezomib for 4 hours or an equivalent volume of DMSO, followed by either a 4-hour recovery in fresh liquid ½ MS medium or a 20-hour recovery in fresh liquid ½ MS medium containing 1 µM Concanamycin A or an equivalent volume of DMSO. For TUBE-pulldown experiments, 7-day-old seedlings were incubated with either 5 µM Bortezomib or an equivalent volume of DMSO for 1 hour under control conditions, followed by a 1-hour recovery in fresh liquid ½ MS medium.

For autophagic flux experiments after CB5083 treatment, 7-day-old seedlings were incubated with either 50 µM CB5083 (BIOCAT GmbH) for 4 hours or an equivalent volume of DMSO, followed by either a 4-hour recovery in fresh liquid ½ MS medium or a 20-hour recovery in fresh liquid ½ MS medium containing 1 µM Concanamycin A or an equivalent volume of DMSO.

For electron and confocal microscopy, seeds were sown in a single line on ½ MS medium (Duchefa) containing 1% agar and 1% sucrose, stratified in the dark at 4ºC for 48 hours, and grown under 50 µmol m^{-2} s^{-1} LED lighting with a 16-hour light/8-hour dark photoperiod for 5 days under control conditions. Plates were oriented vertically to promote root elongation along the medium surface. To assess co-localization during HS, 5-day-old seedlings were incubated at 37ºC for 3 hours, followed by a 3-hour recovery under control conditions before imaging. For autophagic flux analysis during HS, seedlings were incubated at 37ºC for 3 hours, then transferred to fresh liquid ½ MS medium containing 1 µM Concanamycin A (dissolved in DMSO) or an equivalent volume of DMSO and allowed

a 3-hour recovery under control conditions before imaging. For autophagic flux analysis after Bortezomib treatment, 5-day-old seedlings were transferred to fresh liquid ½ MS medium containing 50 µM Bortezomib (Santa Cruz; CAS 179324-69-7; dissolved in DMSO) or an equivalent volume of DMSO and incubated for 2 hours under control conditions. This was followed by a 2.5-hour recovery in ½ MS medium containing 1 µM Concanamycin A or an equivalent volume of DMSO before imaging.

For proteasome activity assays, *A. thaliana* seeds of the specified genotypes were sown on ½ MS medium (Duchefa) containing 0.8% agar, stratified in the dark at 4ºC for 72 hours, and grown under 110 µmol m^{-2} s^{-1} light intensity with a 16-hour light/8-hour dark photoperiod at 22ºC/18ºC and 70% relative humidity for 14 days. Fourteen-day-old seedlings were incubated under control conditions or at 37ºC for 4 hours, followed by a 4-hour recovery phase under control conditions. After recovery, samples were flash-frozen in liquid nitrogen (each biological replicate consisted of six randomly selected seedlings of the same genotype from identically treated plates) and stored for further analysis (Sánchez de Medina and Nava García, et al., 2024, BioRxiv).

Affinity purification coupled to mass spectrometry (AP-MS) of *A. thaliana* samples

For affinity purification coupled with mass spectrometry (AP-MS) of *Arabidopsis thaliana* samples, 7-day-old seedlings expressing mCherry, mCherry-AtATG8A, or mCherry-AtATG8E were prepared as described previously and used as starting material. The tissue weight was measured, and the samples were ground in GTEN buffer (10% glycerol, 50 mM Tris-HCl pH 7.5, 150 mM NaCl, 1 mM EDTA, 0.2% Nonidet P-40, 0.5 mM DTT, and Protease Inhibitor Cocktail tablet) at a 3:1 v/w ratio. Each sample was first ground into a fine powder using a mortar and pestle in liquid nitrogen. The powdered tissue was then mixed with chilled GTEN buffer in the mortar to form a fine paste. The crude extract was allowed to thaw on ice in the mortar for approximately 15 minutes while other samples were processed in the same manner. The extracts were collected into 15 mL Falcon tubes and placed on a carousel at 4°C for 25 minutes. Afterward, the samples were centrifuged twice in a swinging-bucket rotor at maximum speed for 15 minutes. The cleared crude extract was transferred to fresh tubes and kept on ice for total protein

quantification, which was performed using the Amidoblack method. For each immunoprecipitation reaction, equal volumes of crude extract were transferred to LoBind Eppendorf tubes and AIM wild-type (AIM wt) or mutant (AIM mut) peptides were added to the extracts at a final concentration of 100 µM. RFP-Trap magnetic agarose beads (Chromotek) were equilibrated in 1 mL of GTEN buffer on a carousel at 4°C. The bead slurry volume was set to 30 µL per reaction, and the total slurry volume for the experiment was equilibrated in a single tube. The beads were immobilized on a magnetic stand, and the appropriate volume of equilibrated beads was added to each tube. The binding reactions were carried out on a carousel rotating at 12 rpm for 1 hour at 4°C. After binding, the samples were briefly centrifuged in a tabletop centrifuge and immobilized on a magnetic stand placed on ice. The crude extract was removed by pipetting and replaced with 0.9 mL of GTEN buffer. Each tube was inverted approximately six times by hand, centrifuged again, and immobilized. This washing procedure was repeated three times using GTEN buffer. Subsequently, the samples were washed three additional times with a buffer containing 10% glycerol, 50 mM Tris-HCl pH 7.5, 150 mM NaCl, and 1 mM EDTA (without detergent, DTT, or protease inhibitors). The first wash was performed by inverting the tubes by hand, while the second and third washes involved rotating the tubes 360° on the magnetic rack. After the final wash, the beads were resuspended in 200 µL of the same buffer and transferred to fresh LoBind Eppendorf tubes. A 20 µL aliquot (1/10th of the beads) was removed, denatured in 10 µL of 2X Laemmli buffer, and used for quality control via western blot analysis. The remaining beads were drained of excess buffer and flash-frozen in liquid nitrogen before undergoing on-bead trypsin digestion (Sánchez de Medina and Nava García, et al., 2024, BioRxiv).

In vivo co-immunoprecipitation (CoIP)

For the enrichment of mCherry-AtATG8E, 7-day-old seedlings were prepared as described previously and used as the starting material. For each sample, 150–250 mg of frozen tissue was ground into a fine powder in 1.5 mL Safe-Lock Eppendorf tubes containing glass beads (Carl Roth; 1.7–2.1 mm) using a Silamat S6 (Ivoclar Vivadent). The pulverized tissue was then mixed and homogenized with chilled GTEN buffer (10% glycerol, 50 mM Tris-HCl pH 7.5, 150 mM NaCl, 1 mM EDTA, 0.2% Nonidet P-40, 0.5

mM DTT, and Protease Inhibitor Cocktail tablet) at a 3:1 v/w ratio. The tubes were placed on a carousel at 4ºC (14 rpm) to allow lysis to proceed for approximately 30 minutes.

After lysis, the samples were centrifuged twice in a microcentrifuge at maximum speed for 15 minutes at 4ºC. The cleared crude extract was transferred to fresh tubes and kept on ice. For each immunoprecipitation reaction, equal volumes of crude extract were transferred to LoBind Eppendorf tubes. RFP-Trap magnetic agarose beads (Chromotek) were equilibrated in GTEN buffer, and normalized plant extracts were incubated with 30 µL of bead slurry per reaction. The binding reactions were carried out on a carousel rotating at 12 rpm for 1 hour at 4ºC.

Following binding, the samples were briefly centrifuged in a tabletop centrifuge and immobilized on a magnetic stand placed on ice. The crude extract was removed by pipetting and replaced with 0.9 mL of GTEN buffer. Each tube was inverted approximately six times by hand, centrifuged again, and immobilized. This washing procedure was repeated three times using GTEN buffer. The purified complexes were then eluted and denatured in 20 µL of 2X Laemmli buffer for 10 minutes at 70ºC before being analyzed by Western blotting (Sánchez de Medina and Nava García, et al., 2024, BioRxiv).

Sample preparation for Confocal Microscopy

For *Arabidopsis thaliana* confocal microscopy, whole seedlings were mounted on slides with water, and the roots were covered with coverslips. Epidermal cells in the root transition zone were imaged to assess co-localization, while those in the root elongation zone were imaged for autophagic flux analysis (Sánchez de Medina and Nava García, et al., 2024, BioRxiv).

Confocal Microscopy

All *A. thaliana* images were acquired using an upright point laser scanning confocal microscope (ZEISS LSM800 Axio Imager.Z2, Carl Zeiss) equipped with high-sensitivity GaAsP detectors (Gallium Arsenide), an LD C-Apochromat 40X objective lens (numerical aperture 1.1, water immersion), and ZEN software (blue edition, Carl Zeiss). GFP

fluorescence was excited at 488 nm and detected between 410 and 546 nm. mScarlet fluorescence was excited at 561 nm and detected between 571 and 617 nm. mCherry fluorescence was excited at 587 nm and detected between 565 and 617 nm. For each experiment, all replicate images were acquired using identical parameters. Confocal images were processed using Fiji software (version 1.52, Fiji) and exported as .tiff files for panel assembly (Sánchez de Medina and Nava García, et al., 2024, BioRxiv).

Image processing and analysis

For co-localization and autophagic flux experiments, single snapshots were used for quantification. Co-localization experiments were analyzed using Mander's co-localization analysis (Vega-Lugo et al., 2022) via Fiji software (version 1.52 and later versions, including 2.14.0/1.54f). M1 and M2 Mander's coefficient values were calculated using the JACoP plugin. Thresholds for each channel were adjusted for individual snapshot images based on the puncta signal in the original confocal images, as configured in the JACoP plugin settings.

For quantifying the total number of puncta, images were cropped to focus on the root area. Brightness and contrast for each channel were standardized across all images. Thresholds were adjusted for each snapshot image based on the puncta signal in the original confocal images, and particles were counted using the "Analyze Particles" function with size parameters of 0.1–9 μm² and circularity values of 0.00–1.00. The number of puncta per 10,000 μm² was normalized by multiplying the puncta count by 10,000 μm² and dividing by the crop area.

For vacuolar versus cytoplasmic puncta quantification, images were cropped to focus on the root area. Brightness and contrast for each channel were standardized across all images. Cytoplasmic puncta were identified using the "multi-point" function, and Regions of Interest (ROIs) were saved for cytoplasmic puncta selection in each image. Thresholds were adjusted for each snapshot image based on the puncta signal in the original confocal images, and particles were counted using the "Analyze Particles" function with size parameters of 0.1–9 μm² and circularity values of 0.00–1.00. Composite ROIs for

identified particles were saved. ROIs for cytoplasmic puncta were added to the composite ROI image for total puncta to distinguish between cytoplasmic and vacuolar puncta. Vacuolar puncta were manually quantified using the "multi-point" function. The number of cytoplasmic puncta was confirmed by subtracting the vacuolar puncta count from the total puncta count. Total, cytoplasmic, and vacuolar puncta counts per 10,000 μm² were normalized by multiplying the respective puncta counts by 10,000 μm² and dividing by the crop area. Ratios were calculated by dividing the normalized number of vacuolar or cytoplasmic puncta by the total normalized puncta count (Sánchez de Medina and Nava García, et al., 2024, BioRxiv).

Transmission Electron Microscopy (TEM)

High-pressure freezing, freeze-substitution, low-temperature embedding, ultramicrotomy, and TEM imaging were performed following a previously described protocol. Briefly, after the respective plant treatments, roots from 5-day-old seedlings were cryofixed using an HPM100 high-pressure freezer (Leica Microsystems, Austria) and incubated in a freeze-substitution medium (anhydrous acetone containing 0.25% glutaraldehyde and 0.1% uranyl acetate) for two days at −80°C. The incubation temperature was then gradually increased to −50°C at a rate of 1°C per hour. The freeze-substitution medium was subsequently washed with anhydrous acetone, and the samples were embedded in HM20 resin (Ted Pella, USA) over two days at −50°C. Resin curing was performed under UV illumination for 24 hours at −50°C. Freeze-substitution, resin embedding, and polymerization were carried out using an AFS2 machine (Leica Microsystems, Austria).

For double-immunogold labeling of transgenic *A. thaliana* plants co-expressing AtCESAR2-GFP and mCherry-AtATG8E, primary antibodies α:GFP (chicken polyclonal antibody; ab13970) and α:mCherry (rabbit polyclonal antibody; ab167453) were diluted 1:80 and 1:40, respectively. The primary antibodies were detected using secondary antibodies conjugated with gold particles: anti-rabbit IgG (10 nm; SKU.25109, Electron Microscopy Sciences) and anti-chicken IgG (15 nm; SKU.25591, Electron Microscopy Sciences). Thin sections (90 nm) and immunogold labeling were prepared as described previously(Kang, 2010; Wang et al., 2017). Post-staining was performed with uranyl

acetate and Reynolds lead citrate solutions. The sections were then examined using a transmission electron microscope (Hitachi H-7650) operated at 80 kV (Sánchez de Medina and Nava García, et al., 2024, BioRxiv).

Plant phenotypic assays

For carbon starvation assays, approximately 30 ethanol-sterilized seeds were cultivated in 12-well plates containing liquid ½ MS salts (Duchefa) with 1% sucrose. After stratification, the plates were placed under a 16-hour light/8-hour dark photoperiod with a light intensity of 50 µmol m^{-2} s^{-1} and constant gentle shaking. On day 9, the medium was replaced with either a control medium (½ MS, MES, 1% sucrose; +C) or a carbon-deficient medium (½ MS, MES; -C). Seedlings were rinsed twice with their respective medium, and plates with carbon-deficient medium (-C) were wrapped in aluminum foil to block photosynthesis. Seedlings were grown in their respective media for an additional 6 days before imaging.

For nitrogen starvation assays, approximately 30 ethanol-sterilized seeds were grown in 12-well plates containing liquid ½ MS salts (Caisson Labs) with 1% sucrose. After stratification, the plates were maintained under a 16-hour light/8-hour dark photoperiod with a light intensity of 50 µmol m^{-2} s^{-1} and constant gentle shaking. On day 9, the medium was replaced with either nitrogen-sufficient medium (½ MS salts with 1% sucrose; +N) or nitrogen-deficient medium (-N), which consisted of ½ MS salts without nitrogen (Caisson Labs) supplemented with Gamborg B5 vitamin mixture (Duchefa), 0.5 g/L MES, and 1% sucrose (pH 5.7). Seedlings were rinsed twice with their respective medium and returned to the same culture conditions for 6 additional days before imaging.

For heat stress (HS) phenotypic assays, 7 x 7 x 6.5 cm pots were filled with 58 grams of peat-based substrate (Klasmann Substrat 2, Klasmann-Deilmann GmbH, Geeste, DE) and soaked in water for 24 hours. A *Bacillus thuringiensis* solution was applied to prevent fungus gnats. Seeds from four genotypes (as shown in Figure 5) were vapor-phase sterilized (90% sodium hypochlorite and 10% HCl), and approximately 15 seeds were sown per pot. Genotypes and treatment positions were randomized. Seeds were stratified

in the dark at 4ºC for 24 hours and grown for 5 days under an 8-hour light/16-hour dark photoperiod (short-day) with a light intensity of 165 µmol m^{-2} s^{-1} (PPFD) using LED channels (400 nm, white 4500K, 660 nm, and 730 nm). On day 5, extra seedlings were removed, leaving one seedling per pot to grow for an additional 16 days. At 21 days old, plants were subjected to either control conditions or heat stress (37ºC) for 3 consecutive days without watering under an 8-hour light/16-hour dark photoperiod. Plants were then allowed to recover under control conditions for 18 days, maintaining the same pre-treatment growth conditions. Images were taken 18 days post-treatment.

For rosette area measurements, individual pot images were cropped to 1720 x 1720 pixels and converted to 8-bit format. Pixel units were converted to centimeters (930 pixels = 7 cm). The rosette area was manually selected and adjusted using the Threshold command, and the Paintbrush tool was used to remove non-rosette regions, such as pot borders. The rosette area was measured using the Analyze Particles command in Fiji with a Circularity value of 0 and a size range of 20–Infinity. The measured rosette areas were used for statistical analysis.

For Bortezomib phenotypic assays, 40 seeds per genotype (four genotypes as shown in Figure 5) were sown in single-line arrays on solid ½ MS medium (Duchefa) containing 1% sucrose and 1% agar, supplemented with either 3.75 µM Bortezomib (Santa Cruz; CAS 179324-69-7; dissolved in DMSO) or an equivalent volume of DMSO as a control. Genotypes were sown in randomized positions on the plates. Seeds were stratified in the dark at 4ºC for 72 hours and grown on horizontally oriented plates under 50 µmol m^{-2} s^{-1} LED light intensity with a 16-hour light/8-hour dark photoperiod at 21ºC for 18 days. After 18 days, resistant seedlings were photographed and counted. The number of sensitive seedlings was determined by subtracting the number of resistant seedlings from the total number of seeds sown. Green seedlings larger than 0.3 cm in width were classified as resistant (Sánchez de Medina and Nava García, et al., 2024, BioRxiv).

Plant pictures

All plant images were captured using a Canon EOS 80D DSLR camera equipped with either a 60 mm fixed lens or an 18–135 mm lens, using manual settings in CR2 format. The camera was mounted on a fixed stand, and a dark cloth was used as the background. *A. thaliana* images were processed in Fiji, where brightness and contrast were standardized across all images. The pictures were then exported in TIFF format for panel assembly (Sánchez de Medina and Nava García, et al., 2024, BioRxiv).

Proteasome activity measurements

Proteasome activity measurements in *Arabidopsis thaliana* under heat stress were conducted following a previously published protocol (Langin, G., and Üstün, S.,2023) (Lois and Trujillo, 2023) using the Proteasome-Glo™ Cell-Based Assay (Promega, Walldorf; cat. no. G1180) with minor modifications. Briefly, treated seedlings of the specified genotypes were homogenized in 600 µL of ice-cold proteasome extraction buffer (50 mM HEPES-KOH pH 7.2, 2 mM DTT, 2 mM ATP, 0.25 M sucrose) and incubated on ice for 10 minutes. The samples were then centrifuged at 17,000 × g for 10 minutes at 4°C. During centrifugation, proteasome assay substrates were prepared according to the original protocol.

After centrifugation, 150 µL of the proteasome extract supernatant was transferred to a new microcentrifuge tube and diluted 1:1 with ice-cold proteasome extraction buffer. For each sample, 50 µL of the diluted extract was pipetted into three separate wells of a white 96-well plate to measure the three protease activities (chymotrypsin-like, trypsin-like, and caspase-like) individually. The plate was incubated at room temperature in darkness for 15 minutes. Subsequently, 50 µL of the respective substrate solutions were added to the proteasome extracts using a multichannel pipette to initiate the reaction. Luminescence was measured using a microplate reader (Tecan Infinite 200 PRO) over a 30-minute time course, with data points recorded every minute. The results were analyzed as described in the original protocol (Langin, G., and Üstün, S.,2023) (Lois and Trujillo, 2023), and the data were presented as relative luminescence units per minute (RLU min^{-1}), representing

the respective protease activities (Sánchez de Medina and Nava García, et al., 2024, BioRxiv).

Protein extraction and Western Blotting

Plant material was harvested following the respective treatments and flash-frozen in liquid nitrogen. The frozen tissue was ground into a fine powder in 1.5 mL Safe-Lock Eppendorf tubes containing glass beads (Carl Roth; 1.7–2.1 mm) using a Silamat S6. Total protein extraction was performed by adding 350 µL of 2X Laemmli buffer to the ground tissue and homogenizing the mixture in the Silamat S6 for 20 seconds. The samples were then denatured at 70ºC for 10 minutes and centrifuged at maximum speed for 5 minutes in a microcentrifuge. Protein quantification was carried out using either the Bradford assay (Sigma-Aldrich) according to the manufacturer's instructions or the Amidoblack method (Popov et al., 1975). For the Amidoblack method, 10 µL of the protein sample was diluted in 190 µL of deionized water and mixed with 1 mL of normalized Amidoblack staining solution (90% methanol, 10% acetic acid, 0.05% Naphthol Blue Black). The samples were centrifuged at maximum speed for 10 minutes, and the supernatant was discarded. The resulting pellets were washed with 1 mL of washing solution (90% ethanol, 10% acetic acid), centrifuged again, and dissolved in 1 mL of 0.2 N NaOH. The optical density (OD) at 630 nm was measured using a plate reader (Synergy HTX Multi-Mode Microplate Reader; BioTek) with NaOH as the blank. Protein concentration was calculated using the formula $C=(OD-b)10aC=10a(OD-b)$, where aa and bb were determined from a Bovine Serum Albumin (BSA) standard curve.

For Western blotting, the indicated amount of total protein was loaded onto SDS-PAGE gels (4–20% Mini-PROTEAN TGX precast gel; Bio-Rad) and transferred to membranes. Transfers were performed either on PVDF Immobilon-P membranes (Millipore) using a wet transfer apparatus (Bio-Rad) in cold transfer buffer (25 mM Tris Base, 175 mM Glycine, 20% ethanol) for 2 hours at 170 mA, or on nitrocellulose membranes (Bio-Rad) using the semi-dry Trans-Blot Turbo Transfer System (Bio-Rad). Membranes were blocked in TBST (10 mM Tris-HCl pH 7.5, 150 mM NaCl, 0.1% Tween 20) supplemented with 5% skimmed milk or 2.5% BSA at room temperature for 1 hour. Primary antibodies

were incubated with the membranes for 1 hour at room temperature or overnight at 4ºC in blocking buffer. After several washes with TBST, membranes were incubated with secondary antibodies diluted in TBST + 5% skimmed milk for 45 minutes, followed by additional washes before imaging. All primary and secondary antibodies are listed in the materials section. The immune reaction was developed using either Pierce™ ECL Western Blotting Substrate (ThermoFisher) or SuperSignal™ West Pico PLUS Chemiluminescent Substrate (ThermoFisher) and detected using either the ChemiDoc Touch Imaging System (Bio-Rad) or the iBright Imaging System (Invitrogen). Equal protein loading was confirmed by Amidoblack staining of the membranes (Sánchez de Medina and Nava García, et al., 2024, BioRxiv).

Protein expression and purification for biochemical assays

Recombinant proteins were expressed in *E. coli* strain Rosetta2 (DE3) pLysS. Transformed cells were grown in 2XTY medium supplemented with 100 µg/mL spectinomycin at 37ºC until reaching log phase (OD600 0.6–0.8). Protein expression was induced with 300 µM isopropyl β-D-1-thiogalactopyranoside (IPTG), and the cultures were incubated overnight at 18ºC. Cells were harvested by centrifugation and resuspended in lysis buffer (100 mM Sodium Phosphate [NaPi] pH 7.0, 300 mM NaCl, 20 mM imidazole) supplemented with cOmplete EDTA-free protease inhibitor (Roche) and Benzonase. Cells were lysed by sonication, and the lysate was clarified by centrifugation at 20,000 × g.

The clarified lysate was loaded onto a HisTrapFF column (GE Healthcare) pre-equilibrated with lysis buffer. Proteins were washed with lysis buffer for 10 column volumes (CV) and eluted with lysis buffer containing 500 mM imidazole. The eluted fractions were buffer-exchanged to 50 mM NaPi pH 7.2, 50 mM NaCl, and further purified using either cation exchange (Resource S, Cytiva) or anion exchange (Resource Q, Cytiva) chromatography. Proteins were eluted using a gradient of 5–55% (v/v) Ion Exchange Buffer B (50 mM NaPi pH 7.2, 1 M NaCl) over 20 CV.

Finally, proteins were separated by size exclusion chromatography using a HiLoad® 16/600 Superdex® 75 pg column (GE Healthcare) pre-equilibrated in 50 mM NaPi pH 7.0, 100 mM NaCl. Proteins were concentrated using Vivaspin concentrators (5000 Da MWCO). Protein concentration was determined by measuring UV absorption at 280 nm using a DS-11 FX+ Spectrophotometer (DeNovix) (Sánchez de Medina and Nava García, et al., 2024, BioRxiv).

Ubiquitin-Linkage specificity analysis

To analyze ubiquitin-linkage specificity, 10 nmol of Halo-tagged MpCESAR CUE domain was incubated with 100 µL of HaloLink resin (Promega) in 500 µL of coupling buffer (50 mM Tris pH 7.5, 150 mM NaCl, 0.05% NP-40 substitute, 0.5 mM TCEP) under constant rotation at 30 rpm for 2 hours at 4°C. The resin was then centrifuged at 800 × g for 2 minutes, and the supernatant was removed. The resin was washed three times with HALO-wash buffer (50 mM Tris pH 7.5, 250 mM NaCl, 0.2% NP-40, 0.5 mM TCEP) and resuspended in 100 µL of pre-chilled HALO-pulldown buffer (50 mM Tris pH 7.5, 150 mM NaCl, 0.1% NP-40, 0.5 mM TCEP, 0.5 mg/mL BSA).

For the pulldown analysis, 10 µL of the coupled Halo-MpCESAR CUE resin was incubated with 30 pmol of tetra-ubiquitin (Ub4) chains of the specified linkages (M1, K6, K11, K29, K33, K48, and K63) in 500 µL of pulldown buffer for 1 hour at 4°C. The resin was centrifuged at 800 × g for 2 minutes at 4°C to remove unbound Ub4 chains, followed by two washes with 500 µL of HALO-wash buffer and one wash with 500 µL of HALO-coupling buffer. Captured Ub4 chains were eluted by adding 20 µL of LDS sample buffer, separated by SDS-PAGE (4–12% Bis-Tris gel, Life Technology), and visualized using silver staining with the Pierce Silver Stain Kit (ThermoFisher) (Sánchez de Medina and Nava García, et al., 2024, BioRxiv).

***In vitro* pulldowns**

For in vitro pulldown experiments, 5 µL of glutathione magnetic agarose beads (Pierce Glutathione Magnetic Agarose Beads, Thermo Scientific) were equilibrated by washing twice with wash buffer (100 mM NaPi pH 7.2, 300 mM NaCl, 1 mM DTT, 0.01% (v/v)

Nonidet P-40). Normalized *E. coli* clarified lysates were mixed with the washed beads and incubated on an end-over-end rotator for 1 hour at 4°C. The beads were washed five times with 1 mL of wash buffer, and bound proteins were eluted by adding 50 µL of Laemmli buffer. The samples were analyzed by western blotting (Sánchez de Medina and Nava García, et al., 2024, BioRxiv).

TUBE pulldown assays

For TUBE (Tandem Ubiquitin Binding Entities) pulldown assays, 7-day-old *A. thaliana* seedlings treated as previously described were used as starting material. Approximately 0.2 grams of tissue was harvested, homogenized in liquid nitrogen, and dissolved in grinding buffer (25 mM Tris-HCl pH 7.5, 150 mM NaCl, 1 mM EDTA, 10% glycerol, 0.25% Nonidet P-40, 1 mM DTT, Protease Inhibitor Cocktail tablet) by vortexing. The plant lysates were cleared by centrifugation at 16,000 × g for 15 minutes at 4°C, and protein concentration was determined using the Bradford protein assay (Sigma-Aldrich).

Halo™ Magnetic Beads (Promega) were coupled to recombinant Halo-tagged TUBEs overnight at 4°C and washed five times with GTEN buffer. Normalized plant extracts were incubated with 10 µL of TUBE-coupled Halo beads for 4 hours at 4°C. The beads were washed five times with GTEN buffer and boiled for 5 minutes at 95°C before immunoblotting with the appropriate antibodies (Sánchez de Medina and Nava García, et al., 2024, BioRxiv).

Co-fractionation assays

Seven-day-old *A. thaliana* seedlings of the specified genotypes (Col-0, *atg5*, *cesar1cesar2*) were subjected to heat stress at 37ºC for 4 hours, followed by recovery under control conditions for either 4 hours (for AtCESAR1-mCherry or AtCESAR2-GFP fractionation assays) or 20 hours (for aggregate isolation). The seedlings were dried, weighed, flash-frozen in liquid nitrogen, and stored at -80ºC. The frozen tissue was ground into a fine powder using a pre-chilled cryo-mill (Vibrating Mill MM 400, Retsch) for 5 cycles at 30 Hz for 30 seconds, with liquid nitrogen cooling between cycles. Aggregate fractionation buffer (100 mM HEPES pH 7.4, 1% Triton X-

100, 300 mM NaCl) supplemented with Protease Inhibitor Cocktail (Roche) and 25 mM N-ethylmaleimide was added at a ratio of 3 volumes per unit mass of dried seedling weight. The lysate was filtered through Miracloth and centrifuged at 2,000 × g for 5 minutes at 4ºC. The supernatant was clarified by filtration through a 0.2 µm PVDF centrifugal filter, and the protein concentration of the flowthrough (referred to as the whole seedling extract) was determined using the BCA assay (ThermoFisher Scientific).

The whole seedling extract was then centrifuged at 20,000 × g for 1 hour at 4ºC. The supernatant was retained as the soluble fraction, and its total volume was used for normalization in subsequent steps. The pellet was washed twice by resuspension in aggregate isolation buffer and centrifuged again at 20,000 × g for 1 hour at 4ºC. The final pellet was boiled in 2X Laemmli buffer and analyzed, along with the soluble fraction, by western blotting (Sánchez de Medina and Nava García, et al., 2024, BioRxiv).

NanoLC-MS/MS Data acquisition and processing

NanoLC-MS/MS analysis was performed using a nano HPLC system (UltiMate 3000 RSLC nano system or Vanquish Neo UHPLC, Thermo Fisher Scientific) coupled to an Orbitrap Exploris 480 mass spectrometer equipped with a Nanospray Flex ion source (Thermo Fisher Scientific). Peptides were loaded onto a trap column (PepMap Acclaim C18, 5 mm × 300 µm ID, 5 µm particles, 100 Å pore size, Thermo Fisher Scientific) at a flow rate of 25 µL/min with 0.1% TFA as the mobile phase. The trap column was then switched in line with the analytical column (PepMap Acclaim C18, 500 mm × 75 µm ID, 2 µm particles, 100 Å pore size, Thermo Fisher Scientific). Peptides were eluted at a flow rate of 230 nL/min, starting with 98% mobile phase A (0.1% v/v formic acid in water) and 2% mobile phase B (80% v/v acetonitrile, 0.1% v/v formic acid), followed by a linear increase to 35% B over 120 minutes. This was followed by a steep gradient to 95% B in 5 minutes, a 5-minute incubation, and a ramp down to the starting conditions (98% A, 2% B) over 2 minutes for equilibration at 30ºC.

The Orbitrap Exploris 480 mass spectrometer was operated in data-dependent mode ("Cycle Time"), performing a full scan (m/z range 350–1,200, resolution 60,000,

normalized AGC target 100%, minimum intensity 25,000, and compensation voltages of -60V and -75V), followed by MS/MS scans of the most abundant ions for a cycle time of 0.9 seconds per compensation voltage. MS/MS spectra were acquired with an isolation width of 1.2 m/z, normalized AGC target 100%, HCD collision energy of 30, and orbitrap resolution of 15,000. Precursor ions with charge states 2–6 were selected for fragmentation and excluded for 45 seconds after selection. Monoisotopic precursor selection (MIPS) was set to "Peptide," and the "Exclude Isotopes" feature was enabled.

For peptide identification, RAW files were processed using Proteome Discoverer (version 2.5.0.400, ThermoScientific) and searched with MSAmanda v2.0.0.1612987 (Dorfer et al., 2014). The peptide mass tolerance was set to ±10 ppm, fragment mass tolerance to ±8 ppm, and the maximum number of missed cleavages to 2, using tryptic enzymatic specificity without proline restriction. Peptide and protein identification was performed in two steps. First, RAW files were searched against species-specific databases (*Chlamydomonas reinhardtii*, *Marchantia polymorpha*, *Physcomitrium patens*, *Arabidopsis thaliana*TAIR10, and *Nicotiana benthamiana* NbD dataset (Kourelis et al., 2019)) supplemented with common contaminants and sequences of tagged proteins of interest, using iodoacetamide as a fixed modification on cysteine. Results were filtered to a 1% false discovery rate (FDR) at the protein level using the Percolator algorithm (Käll et al., 2007) integrated into Proteome Discoverer. A sub-database of identified proteins was generated for further analysis.

In the second step, RAW files were searched against the sub-database using the same settings, with additional variable modifications including methionine oxidation, glutamine-to-pyroglutamate conversion at peptide N-termini, and protein N-terminal acetylation. Post-translational modification site localization was performed using ptmRS, based on phosphoRS (Taus et al., 2011). Identifications were filtered to a 1% FDR at both the protein and peptide spectrum match (PSM) levels, with an Amanda score cutoff of at least 150. Proteins were required to be identified by at least 2 PSMs in at least one sample. Protein areas were calculated in IMP-apQuant (Doblmann et al., 2018) by summing unique and razor peptides, normalized using iBAQ (Schwanhäusser et al., 2011), and further normalized across samples using sum normalization. Match-between-runs (MBR)

was applied for peptides with high-confidence peak areas identified by MS/MS in at least one run. Proteins were filtered to include at least 3 quantified peptide groups. Statistical significance of differentially expressed proteins was determined using the limma package (Smyth, 2004) (Sánchez de Medina and Nava García, et al., 2024, BioRxiv).

Differential protein enrichment analysis

The total number of MS/MS fragmentation spectra was used to quantify each protein. The Peptide-Spectrum Match (PSM) data matrix was analyzed using the R package **IPinquiry4** (https://github.com/hzuber67/IPinquiry4), which calculates Log2 Fold Change (LFC) and P values using the quasi-likelihood negative binomial generalized log-linear model implemented in the **edgeR** package (Kuhn et al., 2023). Only proteins identified with at least 2 PSMs were included in the analysis. Each genotype-treatment combination was performed in triplicate per experiment, except for the empty vector control immunoprecipitations (IPs), which were acquired as duplicates per treatment.

For the analysis of the AIM peptide effect in *A. thaliana* under control conditions, two filtering levels were applied: (1) Empty vector control vs. bait (Adjusted P value < 0.01 and LFC > 0) and (2) AIM wild type (wt) vs. AIM mutant (mut) (Adjusted P value < 0.01 and LFC > 0). All control reactions were pooled for pairwise comparisons. Protein annotations were retrieved using the TAIR bulk data retrieval gene description tool ((Popov et al., 1975)). Overlap analysis was performed using the biotools.fr online tool (https://www.biotools.fr/misc/venny) at the specified thresholds. Protein abundance was visualized in heatmaps as Log2 (Mean PSM + 1), normalized to the mean value per protein, using R. Rows were clustered based on Euclidean distance, and dendrograms were omitted from the figures. Metric multidimensional scaling (MDS) plots were generated by computing Euclidean distance matrices and using the cmdscale function in R.

For the analysis of the AIM peptide effect combined with heat stress (HS) and HS + CB5083 (HS+CB) treatment in *A. thaliana*, four filtering levels were applied: (1) Empty vector control vs. bait (Adjusted P value < 0.01 and LFC > 0, considering all treatments),

(2) AIM wt vs. AIM mut (Adjusted P value < 0.01 and LFC > 0, considering all treatments), (3) control condition vs. HS (Adjusted P value < 0.05 and LFC > 0), and (4) control condition vs. HS+CB (Adjusted P value < 0.05 and LFC > 0). These thresholds were applied to both mCherry-AtATG8A and mCherry-AtATG8E. Protein abundance was visualized in heatmaps as described above, including only proteins that passed the filtering criteria. To compare the effects of the AIM peptide with HS or HS+CB treatment, the LFC for each pairwise comparison was plotted on the x- and y-axes. Data points were separated into quadrants by calculating the centroid for both axes.

Overlap analysis was again performed using biotools.fr (https://www.biotools.fr/misc/venny) at the specified thresholds. Protein abundance was plotted in heatmaps as Log2 (Mean PSM + 1), normalized to the mean value per protein, using R. Rows were clustered based on Euclidean distance, and dendrograms were omitted from the figures (Sánchez de Medina and Nava García, et al., 2024, BioRxiv).

Statistical analysis

All quantification and statistical analyses were performed using GraphPad Prism 8 and 10 software. For co-localization microscopy analyses, a two-tailed Mann-Whitney test was used to assess the significance of differences in M1 and M2 values. For puncta quantification, two-tailed unpaired Student's t-tests with Welch's corrections were used to evaluate differences in the number of puncta between treatments and genotypes. The significance levels for differences between two experimental groups were denoted as follows: *, $P < 0.05$; **, $P < 0.01$;***, $P < 0.001$; ****, $P < 0.0001$; ns, not significant.

For rosette area quantification and Bortezomib-normalized survival rate analysis in Figure 17, an ordinary one-way ANOVA with Tukey's multiple comparisons test was used to assess differences in normalized rosette area and survival rates between genotypes. For Bortezomib-normalized survival rates in Figure S13, a Kruskal-Wallis test followed by Dunn's multiple comparisons test was used to evaluate differences between genotypes. The significance levels for multiple comparisons were marked as follows: Adjusted *P*

value < 0.05; **, Adjusted *P* value < 0.01; ***, Adjusted *P* value < 0.001; ****, Adjusted *P* value < 0.0001; ns, not significant.

For acquired thermotolerance assays, an unpaired one-tailed Student's t-test was used to assess differences between genotypes at different ACC times, with significance levels marked as *P* < 0.05 (*) (Sánchez de Medina and Nava García, et al., 2024, BioRxiv).

RESULTS

Part 1: Identification of CESAR as an AIM-dependent ATG8 interactor

Comparative analysis of ATG8 interactors across species uncovers new SAR candidates

To investigate the diversity of selective autophagy networks in plants, we conducted a cross-species analysis of ATG8 interactomes in five different plant model organisms (Figure 6). Plant lines expressing fluorescent protein fusions of ATG8 were generated and peptide competition-coupled AP-MS of ATG8 was performed in the green alga *Chlamydomonas reinhardtii*, the liverwort *Marchantia polymorpha* the moss *Physcomitrium patens*, and two angiosperms, *Arabidopsis thaliana* and *Nicotiana benthamiana*, encompassing nearly one billion years of evolution (Figure 6). This approach identified 289 ATG8-associated proteins in *C. reinhardtii*, 244 in *M. polymorpha*, 222 in *P. patens*, 339 in *A. thaliana*, and 56 in *N. benthamiana*. The peptide competition significantly reduced the ATG8 interactomes, with reductions of approximately 20-fold in *C. reinhardtii* (17 out of 289), 4-fold in both *M. polymorpha* (61 out of 244) and *P. patens* (59 out of 222), and about 2-fold in both *A. thaliana* (192 out of 339) (Figure S1) and *N. benthamiana* (27 out of 56) (Sánchez de Medina and Nava García, et al., 2024, BioRxiv).

Fig.6

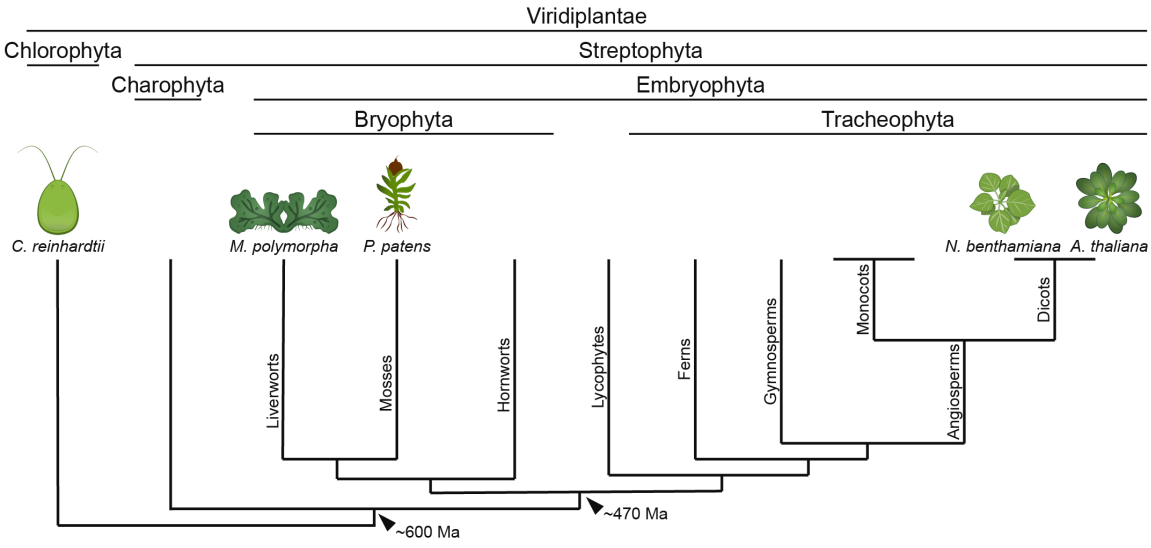

Figure 6. Phylogenetic relationships of species analyzed for ATG8 interactomes. A schematic phylogram illustrating the *Viridiplantae* lineage. The species included in the comparative AP-MS interactome analyses are highlighted.

To gain deeper insights into the evolutionary history of these outcompeted proteins, we used Orthofinder24 to identify their orthologues across all five species and visualized their intersections (Figure 7). While the majority of these proteins have orthologous sequences in all five species, we also observed instances where certain proteins were found in only one species. This likely reflects lineage-specific gains or losses of these proteins. Interestingly, only 12% of the candidate proteins were classified as species-specific orthologous groups, with *A. thaliana* and *P. patens* having the largest number of observations (Figure 7, upper panel). This suggests that most of these gene families were present in the last common ancestor of the *Viridiplantae* and were later adapted for autophagic functions in a lineage-specific manner.

To further test this hypothesis, we examined whether the AIM-dependent ATG8 interactors we experimentally recovered aligned with their orthology-based groupings. This time, we restricted the classification of orthogroups to those based on experimental validation, meaning that only orthologous proteins identified simultaneously in multiple species were grouped together (Figure 7, lower panel). However, some highly conserved orthologous sequences were experimentally identified as species-specific, such as MpYHBC. Notably, we identified a total of 4 proteins across all streptophytes, indicating their long-standing evolutionary conservation in both orthology and function as autophagy players. Among these proteins, we detected the known and conserved selective autophagy receptor NBR1 and a core autophagy protein VPS15. Interestingly, we found a previously uncharacterized and CUE (**C**oupling of **U**biquitin to **E**R degradation; ubiquitin binding domain) domain containing protein, that we named CESAR (**C**U**E**-domain containing **SAR** candidate) and two RING-finger domain-containing paralogous proteins RING1/2, with no previous reported functions in selective autophagy.

Fig.7

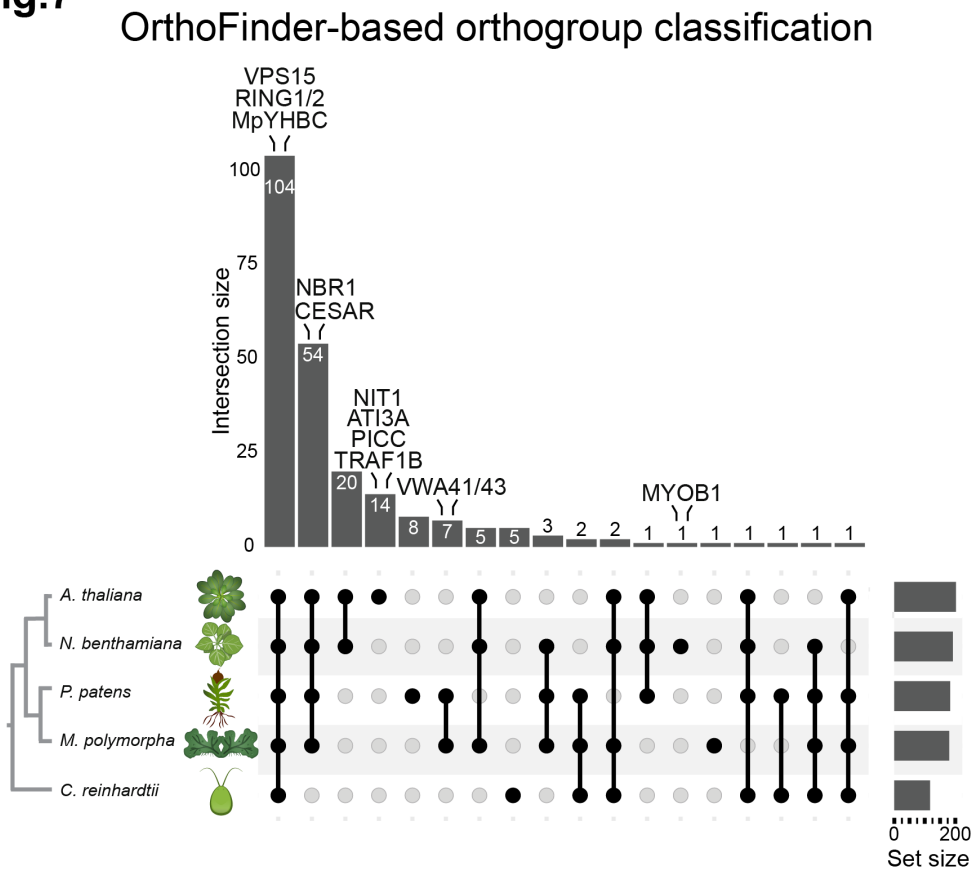
OrthoFinder-based orthogroup classification
VPS15
RING1/2
MpYHBC
NBR1
CESAR
NIT1
ATI3A
PICC
TRAF1B
VWA41/43
MYOB1
Intersection size
100
75
50
25
0
104
54
20
14
8
7
5
5
3
2
2
1
1
1
1
1
1
1
A. thaliana
N. benthamiana
P. patens
M. polymorpha
C. reinhardtii
0
200
Set size

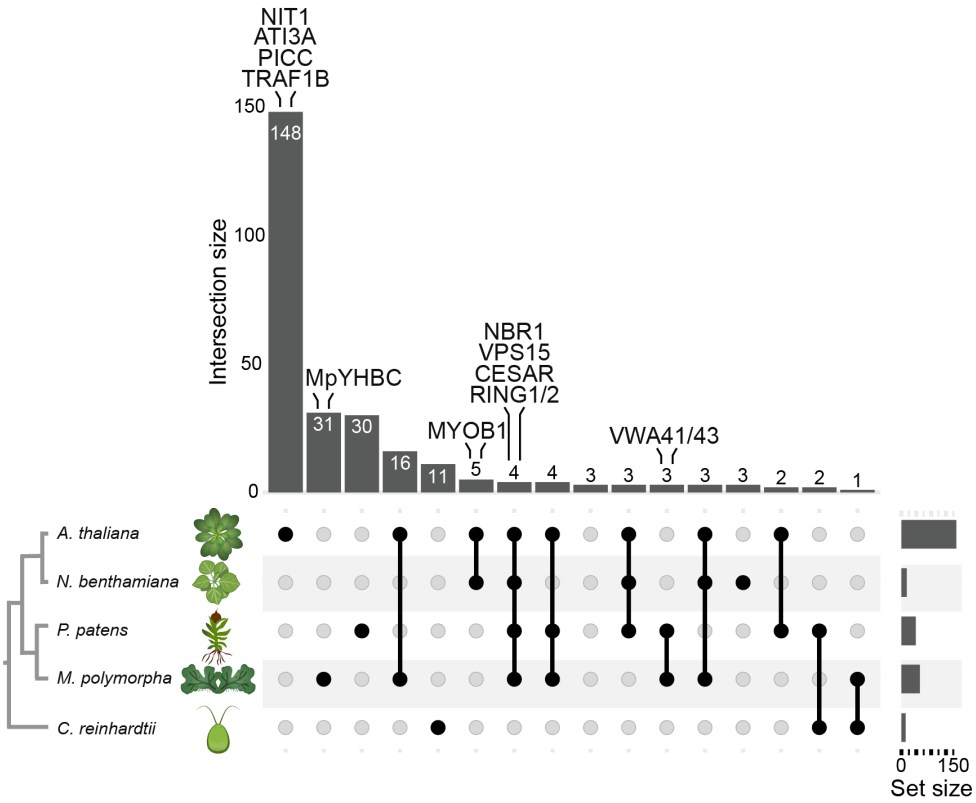
AP-MS-based orthogroup classification
NIT1
ATI3A
PICC
TRAF1B
MpYHBC
NBR1
VPS15
CESAR
RING1/2
MYOB1
VWA41/43
Intersection size
150
100
50
0
148
31
30
16
11
5
4
4
3
3
3
3
3
2
2
1
A. thaliana
N. benthamiana
P. patens
M. polymorpha
C. reinhardtii
0
150
Set size

Figure 7. Orthologous cluster analysis reveals the dynamic nature of autophagy pathways. UpSet plots showcasing unique and shared orthologous clusters identified by OrthoFinder across the species shown in the phylogenetic cladogram on the left. The vertical bar chart represents the intersection size, while the horizontal bar chart on the right indicates the set size. Ortholog groups are arranged by intersection size, with overlaps visualized using vertical lines. The top panel includes orthologous sequences identified from any outcompeted protein, while the bottom panel focuses exclusively on experimentally validated orthologous proteins in the analyzed species. Proteins of interest are highlighted above their respective clusters.

Furthermore, the AIM-dependent interactions between the *Marchantia polymorpha* RING1/2 and CESAR proteins with ATG8, as well as other identified interactions, were validated through *in vitro* pulldown assays and identified as high confidence interactors using AlphaFold predictions (data not shown but detailed in Sánchez de Medina and Nava García et al., 2024, BioRxiv). These findings confirm that the interactions between ATG8 and the listed proteins are direct protein-protein interactions.

In summary, our cross-species analysis of ATG8 interactomes reveals new AIM-dependent ATG8 interactors, highlighting the evolutionary diversity of the ATG8 interactome. Additionally, the use of peptide competition approach simplifies the identification of potential selective autophagy players and provides new opportunities for systematically studying ATG8 interactomes under different stress conditions (Sánchez de Medina and Nava García et.al., 2024, BioRxiv).

Identification of CESAR proteins as top AIM-dependent ATG8 interactors during heat stress recovery in *A. thaliana*

Since heat stress induces protein misfolding and organelle damage, we aimed to identify potential SARs involved in heat stress recovery. To this end, we analyzed ATG8 AIM-dependent interactions enriched during heat stress recovery in *Arabidopsis thaliana* by performing AP-MS on ATG8A and ATG8E isoforms, each belonging to different clades, coupled with peptide competition. For this, 7-d-old seedlings were subjected to 37°C heat

stress for 4 hours, followed by a 6-hour recovery period at 21°C. CB5083 inhibits CDC48, an essential AAA+ ATPase that delivers ubiquitinated proteins to the proteasome for degradation (Bodnar and Rapoport, 2017; Li et al., 2022). We hypothesized that blocking CDC48 would redirect ubiquitinated proteins to autophagy and, therefore, as an additional treatment, we supplemented the media with CB5083 during the recovery phase post-heat stress.

AP-MS analysis coupled to peptide competition of two *Arabidopsis thaliana* ATG8 isoforms (AtATG8A and AtATG8E) identified 33 AIM-dependent interactors that responded to heat stress and heat stress + CB treatments (Figures 8A, 8B, S1; Table S10 found in Sanchez de Medina and Nava García et.al., 2024, BioRxiv). CESAR2 (AT1G03290), emerged as one of the top candidate outcompeted proteins enriched in both ATG8A and ATG8E immunoprecipitation experiments under the tested conditions, a behavior shared with NBR1 (Figures 8C-F). Interestingly, CESAR1 (AT4G02880), a CESAR2 paralog, was similarly enriched as an AIM-dependent ATG8 interactor during heat stress but was not under heat stress + CB treatment (Figure 8A-F).

CESAR was identified as an ATG8 AIM-dependent interactor across all four land plant species included in the comparative analysis. Notably, it ranked among the top interactors detected during heat stress recovery in *Arabidopsis thaliana* and contains a ubiquitin-binding domain. These findings prompted us to focus on this protein to investigate its potential role as a SAR and to further characterize its function in heat stress recovery.

Fig.8

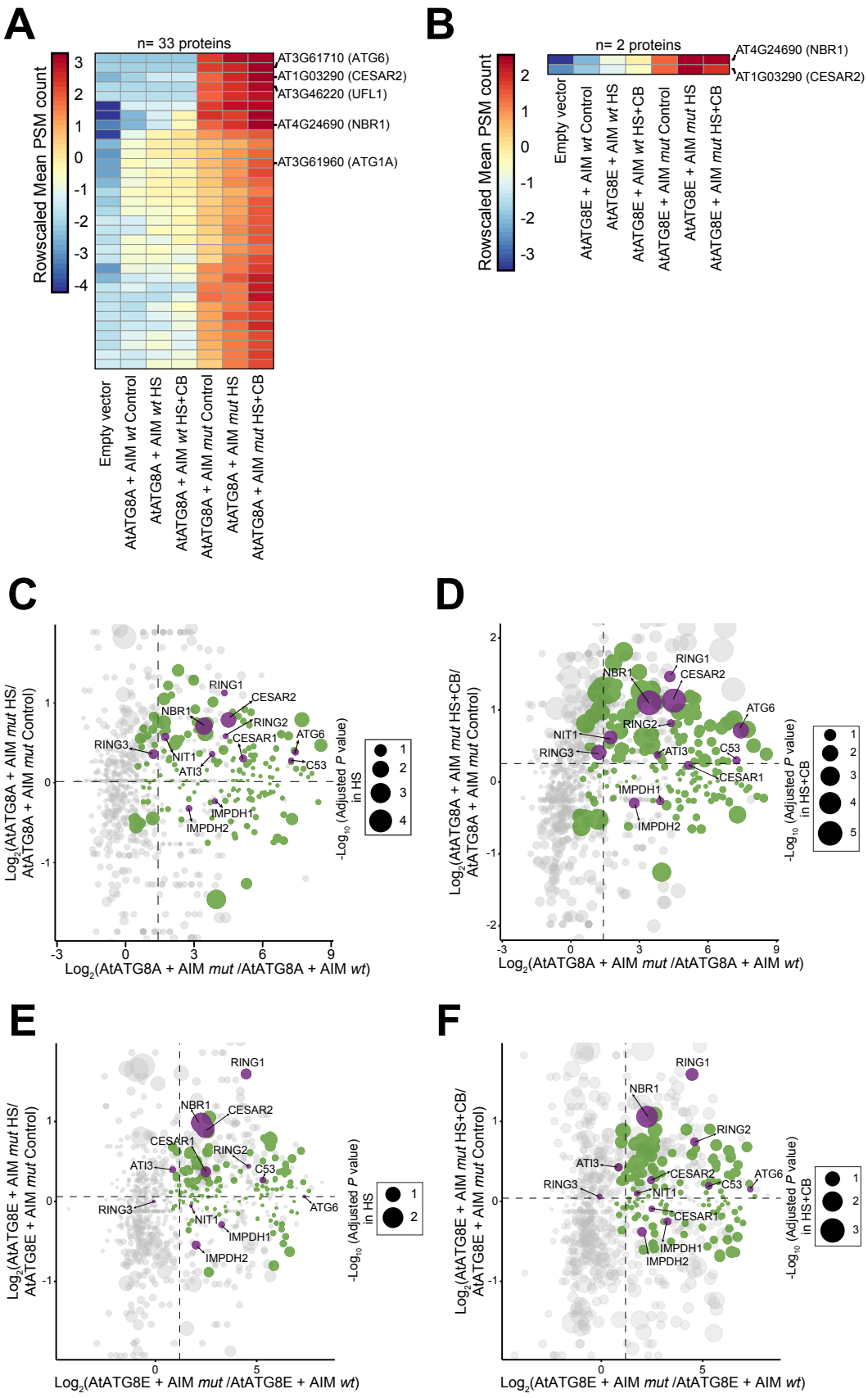
A
n= 33 proteins
Rowscaled Mean PSM count
AT3G61710 (ATG6)
AT1G03290 (CESAR2)
AT3G46220 (UFL1)
AT4G24690 (NBR1)
AT3G61960 (ATG1A)
Empty vector
AtATG8A + AIM wt Control
AtATG8A + AIM wt HS
AtATG8A + AIM wt HS+CB
AtATG8A + AIM mut Control
AtATG8A + AIM mut HS
AtATG8A + AIM mut HS+CB
B
n= 2 proteins
AT4G24690 (NBR1)
AT1G03290 (CESAR2)
C
Log2(AtATG8A + AIM mut HS/ AtATG8A + AIM mut Control)
Log2(AtATG8A + AIM mut /AtATG8A + AIM wt)
-Log10 (Adjusted P value) in HS
D
Log2(AtATG8A + AIM mut HS+CB/ AtATG8A + AIM mut Control)
-Log10 (Adjusted P value) in HS+CB
E
Log2(AtATG8E + AIM mut HS/ AtATG8E + AIM mut Control)
Log2(AtATG8E + AIM mut /AtATG8E + AIM wt)
F
Log2(AtATG8E + AIM mut HS+CB/ AtATG8E + AIM mut Control)

Figure 8. (A) AtATG8A interactome under HS+CB treatment. Heatmap displaying protein abundance patterns (Log2 (Mean PSM+1) – Mean PSM per protein) for 33 AtATG8A-associated and outcompeted proteins identified as induced by HS+CB. Each column represents the row-scaled mean PSM count from three independent biological replicates. **(B) HS+CB treatment promotes AIM-dependent interactions of AtCESAR2 and AtNBR1 with AtATG8E.** A heatmap shows protein abundance patterns (Log2 (Mean PSM+1) – Mean PSM per protein) for two AtATG8E-associated and outcompeted proteins induced by HS+CB. Each column represents the row-scaled mean PSM count from three independent biological replicates. **(C-D) AtATG8A interactome under HS and HS+CB treatments.** Dot plots represent protein abundance as Log2 (Fold change) for two pairwise comparisons: the peptide effect (AtATG8A+AIM mut vs. AtATG8A+AIM wt) on the x-axis and the treatment effect (AtATG8A+AIM mut HS vs. AtATG8A+AIM mut Control) on the y-axis. Dashed lines indicate the centroids for the x- and y-axes. Dot size reflects significant induction in heat-treated samples **(C)** or HS+CB-treated samples **(D),** represented as –Log2 (P value). The 172 AtATG8A-associated and outcompeted proteins (annotated as AIM-dependent in Fig. S1F) are color-coded in green, with proteins of interest highlighted in purple. **(E-F) AtATG8E interactome under HS and HS+CB treatments.** Dot plots display protein abundance as Log2 (Fold change) for two pairwise comparisons: the peptide effect (AtATG8E+AIM mut vs. AtATG8E+AIM wt) on the x-axis and the treatment effect (F: AtATG8E+AIM mut HS+CB vs. Control; G: AtATG8E+AIM mut HS vs. Control) on the y-axis. Dashed lines represent the centroids for the x- and y-axes. Dot size reflects significant induction in HS+CB-treated **(E)** or HS-treated **(F)** samples, represented as –Log2 (Adjusted P value). The 192 AtATG8E-associated and outcompeted proteins (annotated as AtATG8A unique in Fig. S1F) are color-coded in green, with proteins of interest highlighted in purple.

Part2: Characterization of CESAR as a Selective Autophagy Receptor

CESAR2 colocalizes to autophagosomes and undergoes autophagic degradation during prolonged post-heat stress recovery

Phylogenetic analysis suggests that CESAR first originated in Charophyta algae and subsequently underwent gene duplication events in mosses, followed by additional duplications and gene losses throughout plant evolution (Figure S2). In *Arabidopsis thaliana,* there are two gene copies of CESAR, AtCESAR1 (AT4G02880) and AtCESAR2

(AT1G03290), both identified as ATG8 AIM-dependent interactors during heat stress recovery (Figures 8C, 8E; Part1).

First, to determine the subcellular localization of these proteins, we generated transgenic lines co-expressing fluorescently tagged AtCESAR1 and AtCESAR2 under a constitutive promoter in *Arabidopsis thaliana*. Live-cell imaging of root cells from 5d old *Arabidopsis* seedlings revealed that AtCESAR1-mCherry and AtCESAR2-GFP colocalized in cytoplasmic puncta suggesting that CESAR1 and CESAR2 may associate to form a complex (Figure 9A, 9B). Given the high degree of colocalization between these proteins, we focused primarily on AtCESAR2 for further characterization.

Fig.9

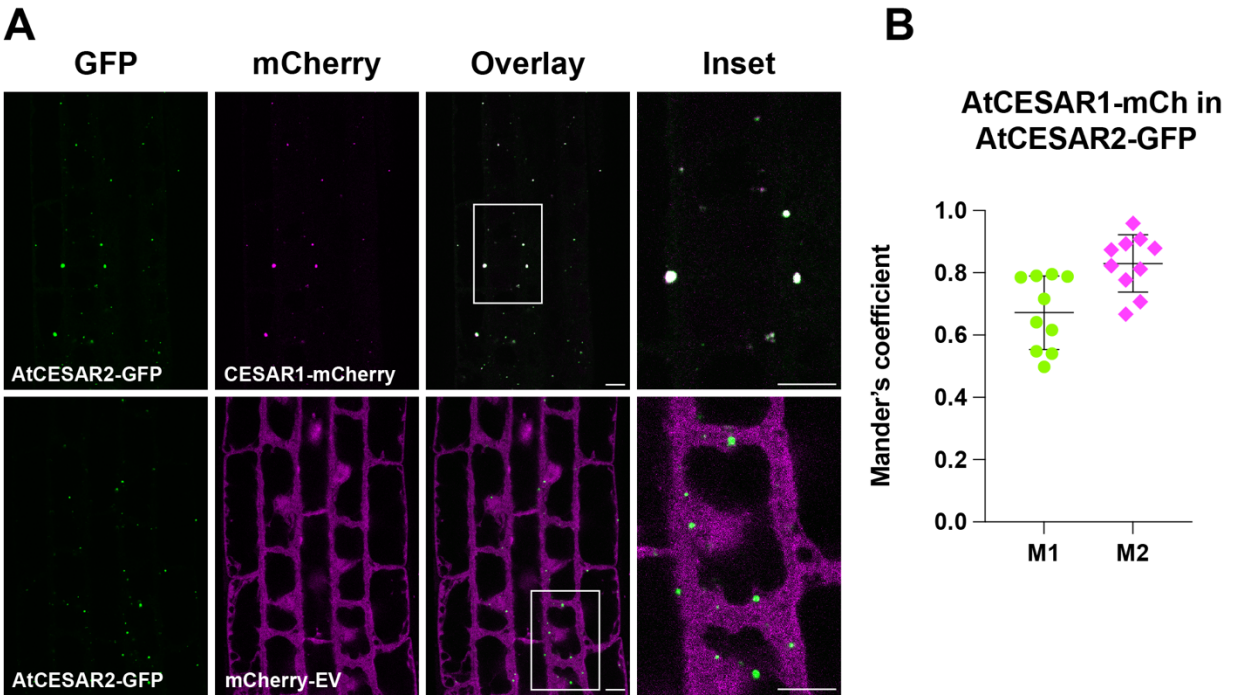

Figure 9. AtCESAR paralogs colocalize. (A) AtCESAR1 and AtCESAR2 co localize. Confocal microscopy images of *Arabidopsis thaliana* root epidermal cells co-expressing AtCESAR2-GFP with either AtCESAR1-mCherry or mCherry-EV (empty vector). Five-day-old *A. thaliana* seedlings were grown on 1% agar ½ MS + MES + 1% sucrose plates at 21°C (control conditions) before imaging. The white-boxed region in the merged panel is enlarged in the inset. Scale bars: 10 µm for both the main image and

inset. **(B) Quantification of colocalization experiments from Fig.9A.** Mander's colocalization coefficients were used to assess the overlap between AtCESAR2-GFP and AtCESAR1-mCherry signals. M1 represents the fraction of AtCESAR2-GFP signal overlapping with AtCESAR1-mCherry, while M2 represents the fraction of AtCESAR1-mCherry signal overlapping with AtCESAR2-GFP. Bars show the mean ± SD from 10 biological replicates.

The interaction between ATG8 and AtCESAR2 was validated through *in vitro* pulldown assays (Figure S3A). Furthermore, AIM mapping of the *A. thaliana* CESAR2 ortholog identified a functional AIM motif within the protein's C-terminal region (Figure S3B).

Next, to assess whether AtCESAR2 localizes to autophagosomes, we generated transgenic lines constitutively expressing AtCESAR2-GFP and mCherry-ATG8E and performed confocal microscopy on root cells of 5-day-old Arabidopsis seedlings. Already in untreated seedlings, some AtCESAR2-GFP puncta colocalized with mCherry-AtATG8E-decorated autophagosomes (Figures 10A, 10B). Upon heat stress recovery, the degree of colocalization between the two proteins further increased as indicated by increased Mander's coefficient M1 values (Figures 10A, 10B).

To examine AtCESAR2-GFP localization at the ultrastructural level, we conducted immunogold labeling transmission electron microscopy with two distinct gold particle sizes: 15 nm for AtCESAR2-GFP and 10 nm for mCherry-AtATG8E. Electron micrographs of *Arabidopsis* root cell sections confirmed that AtCESAR2-GFP colocalizes with double-membraned autophagosomes labeled with mCherry-AtATG8E, aligning with our observations from our live-cell imaging experiments (Figures 10C, S5).

To further validate the association between AtCESAR2 and AtATG8, we performed co-immunoprecipitation (Co-IP) assays under both control and heat stress conditions. This experiment confirmed that AtCESAR2 associates with AtATG8E in an AIM-dependent manner, with the interaction being enhanced during heat stress recovery, similar to NBR1 (Figures 10D, S6). Collectively, these findings demonstrate that the association between AtCESAR2 and ATG8 is upregulated in response to heat stress.

Fig.10

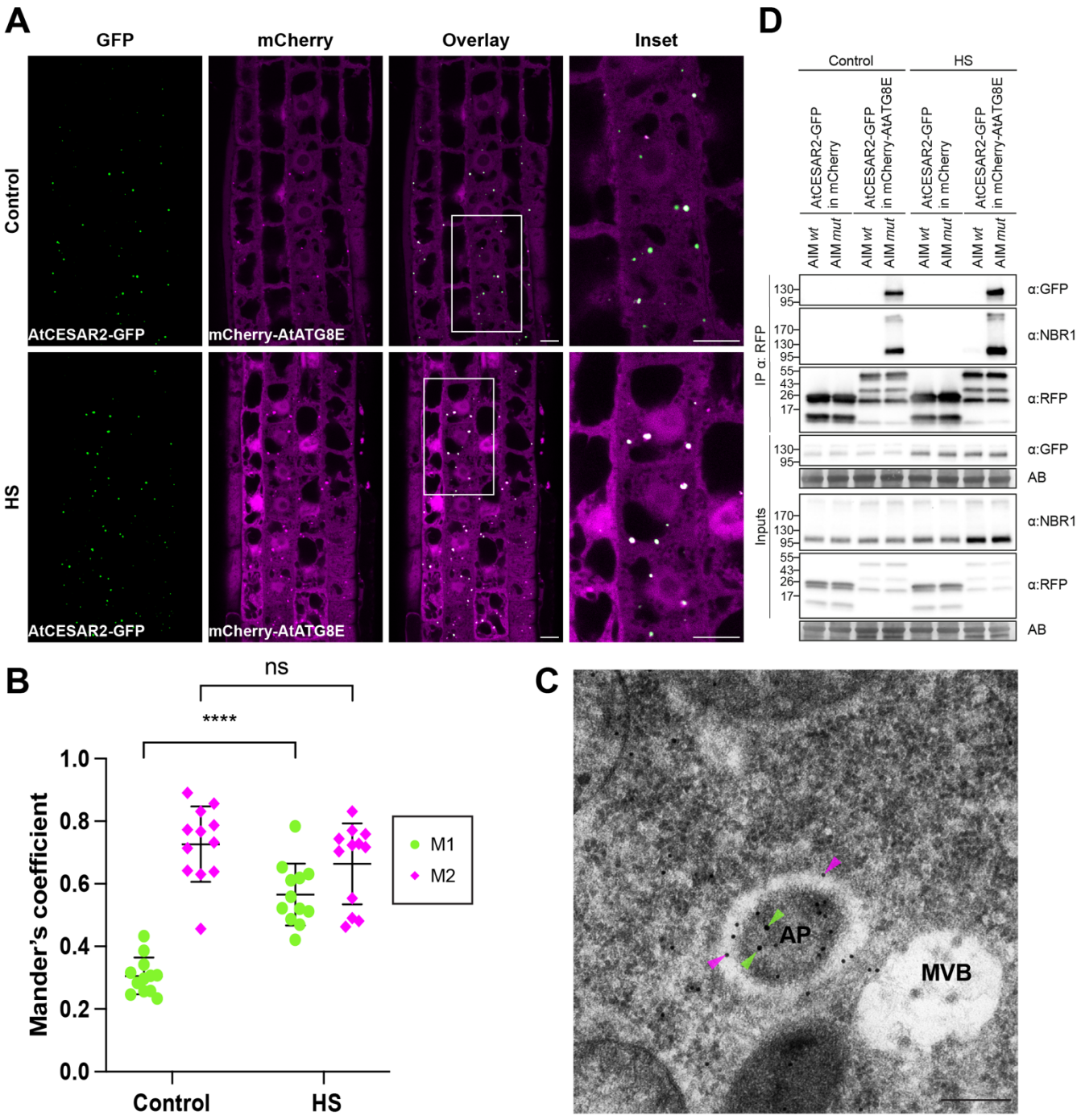

Figure 10. AtCESAR2 localizes to autophagosomes. (A) AtCESAR2 colocalizes with AtATG8E-labeled autophagosomes. Confocal microscopy images of *A. thaliana* root epidermal cells at the transition zone co-expressing AtCESAR2-GFP with mCherry-AtATG8E. Five-day-old *A. thaliana* seedlings were grown on 1% agar ½ MS + MES + 1%

sucrose plates and incubated at 21°C (Control) or 37°C (HS) for 3 hours, followed by a 3-hour recovery at 21°C before imaging. Representative images from 12 biological replicates are shown. The white-boxed region in the merged panel is enlarged in the inset. Scale bars: 10 µm for both the main image and inset. Negative control shown in Fig.S15A
(B) HS increases AtCESAR2 localization to autophagosomes. Quantification of confocal microscopy data from Fig. 10A, using Mander's colocalization coefficients to measure overlap between AtCESAR2-GFP and mCherry-AtATG8E signals. M1 represents the fraction of AtCESAR2-GFP signal overlapping with mCherry-AtATG8E, while M2 represents the fraction of mCherry-AtATG8E signal overlapping with AtCESAR2-GFP. Bars represent the mean ± SD from 12 biological replicates. A two-tailed Mann-Whitney test was used to assess the significance of differences in M1 and M2 values between Control (21°C) and HS (37°C) conditions. ****, $P < 0.0001$.
(C) AtCESAR2 localizes within autophagosomes. Transmission electron microscopy (TEM) images showing immune-gold labeling of AtCESAR2-GFP (15 nm gold particles) or mCherry-AtATG8E (10 nm gold particles) in autophagosomes of *A. thaliana* root cells. Five-day-old *A. thaliana* seedlings were grown at 21°C on 1% agar ½ MS + MES + 1% sucrose plates before cryofixation. Sections from samples co-expressing AtCESAR2-GFP and mCherry-AtATG8E were labeled with anti-GFP and anti-mCherry primary antibodies, followed by secondary antibodies conjugated to 15 nm (GFP, green arrows) or 10 nm (mCherry, magenta arrows) gold particles. Scale bars: 200 nm. AP, autophagosome; MVB, multivesicular body. Controls and replicates are shown in Fig. S5
(D) AtCESAR2 co-immunoprecipitates with AtATG8E *in vivo*. RFP-Trap co-immunoprecipitation coupled with peptide competition was performed on whole-seedling extracts from 7-day-old *A. thaliana* seedlings co-expressing AtCESAR2-GFP with either mCherry-AtATG8E or mCherry-EV (empty vector). Seedlings were incubated at either 21°C (Control) or 37°C (HS) for 6 hours, followed by a 4-hour recovery at 21°C in fresh ½ MS + MES + 1% sucrose media. AIM wild-type (wt) and mutant (mut) peptides were added at a final concentration of 100 µM. Protein extracts were analyzed via immunoblotting with anti-GFP and anti-RFP antibodies. Two independent biological replicates are shown in Fig. S6.

The increased association of AtCESAR2 with AtATG8-decorated autophagosomes during heat stress recovery suggests that AtCESAR2, may undergo autophagic degradation following stress, a feature characteristic of SARs. To investigate whether AtCESAR2 is degraded via autophagy, we treated 5-day-old seedlings with Concanamycin A, an inhibitor of vacuolar acidification. This treatment stabilizes autophagosomes within the vacuole, allowing us to assess the involvement of autophagy in AtCESAR2 degradation.

Inhibition of vacuolar degradation by Concanamycin A in seedlings under control conditions (21ºC) led to the stabilization of AtCESAR2-GFP-decorated autophagosomes within the mature vacuoles of root cells in the elongation zone of the WT genetic background (Figure 11A). Concanamycin A treatment during the 3-hour recovery period after heat stress also resulted in the stabilization of AtCESAR2-GFP puncta within vacuoles (Figure 11A). However, the ratio of vacuolar puncta to total puncta per normalized area (10,000 μm²) was higher in control samples compared to those subjected to heat stress (Figure 11B, left panel). Consistently, the cytoplasmic-to-total puncta ratio was higher in seedlings exposed to heat stress (Figure 11B, right panel). These findings suggest that AtCESAR2 undergoes vacuolar degradation and that during the 3-hour recovery period following heat stress, vacuolar degradation of AtCESAR2 puncta decreases relative to basal conditions at 21ºC, leading to the stabilization of cytoplasmic puncta.

To further investigate the autophagic degradation of AtCESAR2, we analyzed the ratio of vacuolar-to-total AtCESAR2-GFP puncta in the autophagy-deficient mutant *atg5*. In this mutant, no AtCESAR2-GFP puncta were detected inside the vacuole, confirming that AtCESAR2 delivery to the vacuole depends on a functional autophagy machinery and that AtCESAR2 undergoes autophagic degradation (Figure 11A, 11B).

To complement our microscopy-based flux assays, we performed western blot-based autophagic flux assays to further investigate AtCESAR2 dynamics. First, we assessed how AtCESAR2 protein levels respond to different heat stress conditions. Heat stress led to the stabilization of the full-length AtCESAR2-GFP protein after 1 hour, as shown by increased levels of the full-length protein and the absence of free GFP (Figure 12A). This stabilization reached its peak after a 4-hour incubation at 37ºC and was further enhanced following a 4-hour recovery under control conditions (Figure 12A-C), consistent with our microscopy observations.

When we extended the recovery period overnight post-heat stress, we detected a free GFP band, indicating vacuolar degradation of AtCESAR2 (Figure 12C, Figure S7). This free GFP band was stabilized by Concanamycin A treatment and was absent in the *atg5*

mutant, confirming that AtCESAR2 degradation is dependent on autophagy (Figure 12C, Figure S7). Similar degradation kinetics were observed for the endogenous NBR1 and GFP-AtATG8A autophagic fluxes (Figure 12C, Figure S7). Notably, despite the enhanced degradation of CESAR2-GFP during prolonged recovery, full-length CESAR2-GFP levels remained elevated compared to control conditions (Figure 12C, Figure S7).

To determine whether the *CESAR1* and *CESAR2* genes respond to heat stress, we analyzed the endogenous transcript levels of *CESAR1* and *CESAR2* in both the WT and *atg5* mutant backgrounds. Our results showed that *CESAR1* was upregulated under heat stress conditions, whereas *CESAR2* was not (Figure S8A). Interestingly, when we analyzed the expression of the *CESAR2-GFP* transgene driven by a constitutive promoter, we observed that the transcript was stabilized under heat stress (Figure S8B). This suggests that *CESAR2* may be subject to additional regulation at the post-transcriptional level, leading to transcript stabilization during heat stress. However, further investigation is needed to confirm and understand this regulatory mechanism.

In conclusion, these results demonstrate that AtCESAR2 localizes to autophagosomes and undergoes autophagic degradation. Heat stress induces the accumulation of AtCESAR2, which is subsequently degraded via autophagy during extended recovery under control condition.

Fig.11

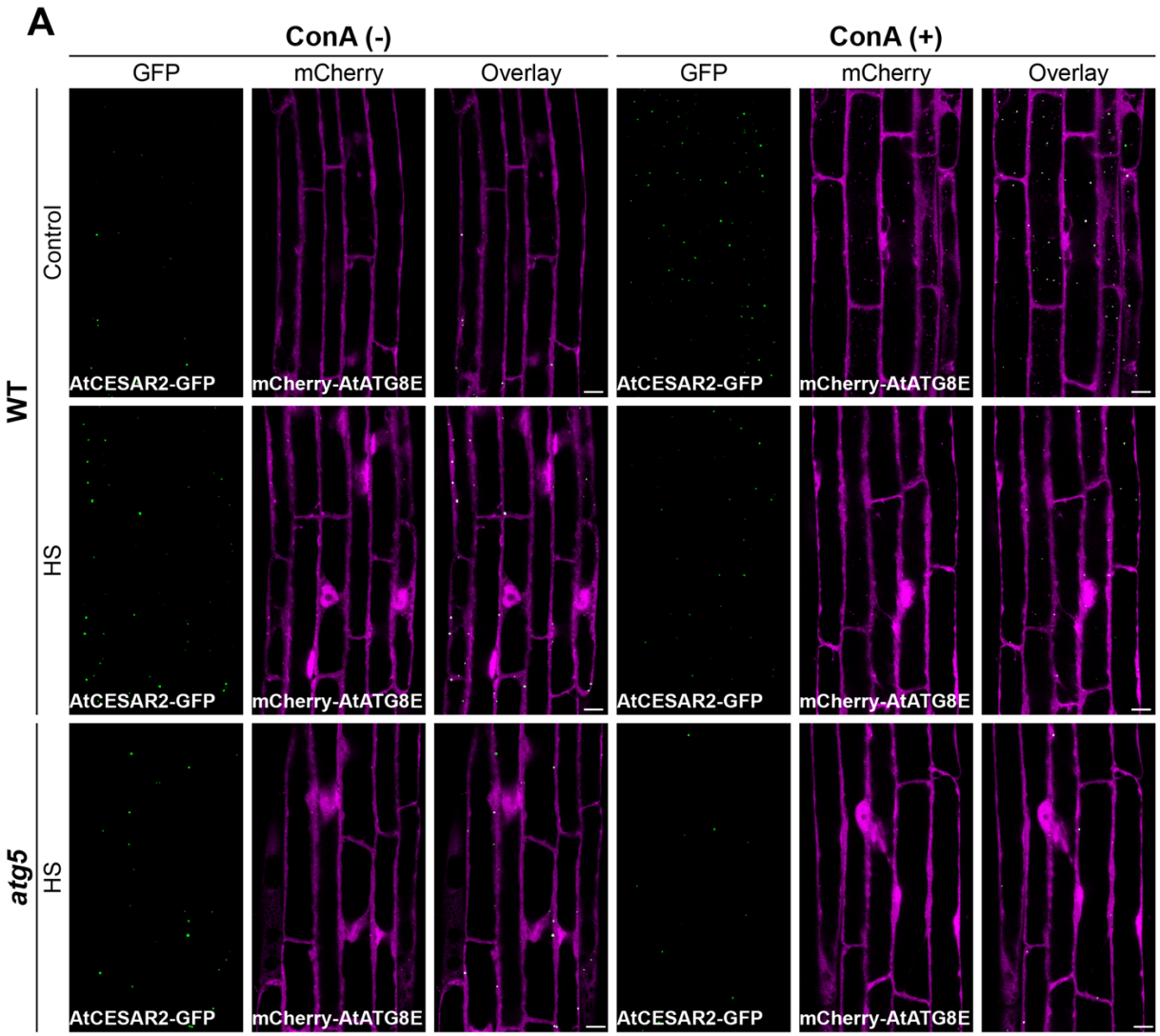
A
ConA (-)
ConA (+)
GFP
mCherry
Overlay
WT
atg5
Control
HS
AtCESAR2-GFP
mCherry-AtATG8E

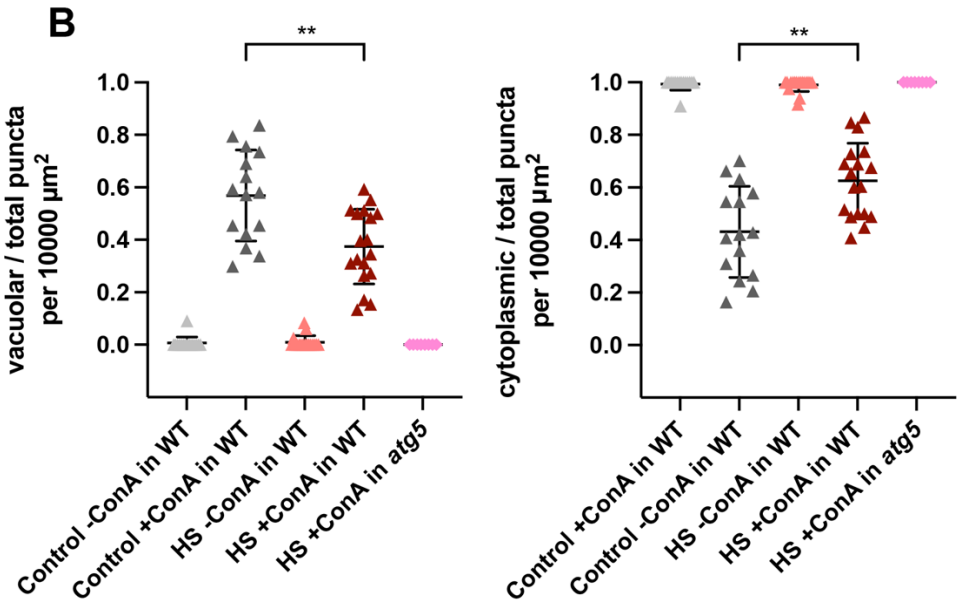
B
**
vacuolar / total puncta per 10000 µm²
cytoplasmic / total puncta per 10000 µm²
1.0
0.8
0.6
0.4
0.2
0.0
Control -ConA in WT
Control +ConA in WT
HS -ConA in WT
HS +ConA in WT
HS +ConA in atg5

Figure 11. AtCESAR2 undergoes autophagic degradation. (A) AtCESAR2 is degraded via autophagy. Confocal microscopy images of *A. thaliana* root epidermal cells at the elongation zone co-expressing AtCESAR2-GFP with mCherry-AtATG8E in wild-type (WT) and *atg5* mutant backgrounds. Five-day-old *A. thaliana* seedlings were incubated at 21°C (Control) or 37°C (HS) for 3 hours, followed by a 3-hour recovery at 21°C in fresh ½ MS + MES + 1% sucrose media with or without 1 μM ConA. Representative images are shown. Scale bars: 10 μm. **(B) HS reduces the rate of autophagic degradation.** Quantification of AtCESAR2-GFP puncta within the vacuole (upper panel) or cytoplasm (lower panel) per normalized area (10,000 μm²). Bars represent the mean ± SD of 15 biological replicates for Control ± ConA in WT, 17 for HS –ConA in WT, 18 for HS + ConA in WT, and 8 for HS + ConA in *atg5*. Two-tailed unpaired Student's t-tests with Welch's corrections were used to analyze differences in puncta ratios between Control and HS recovery conditions. **, P < 0.01 (0.0017).

Fig.12

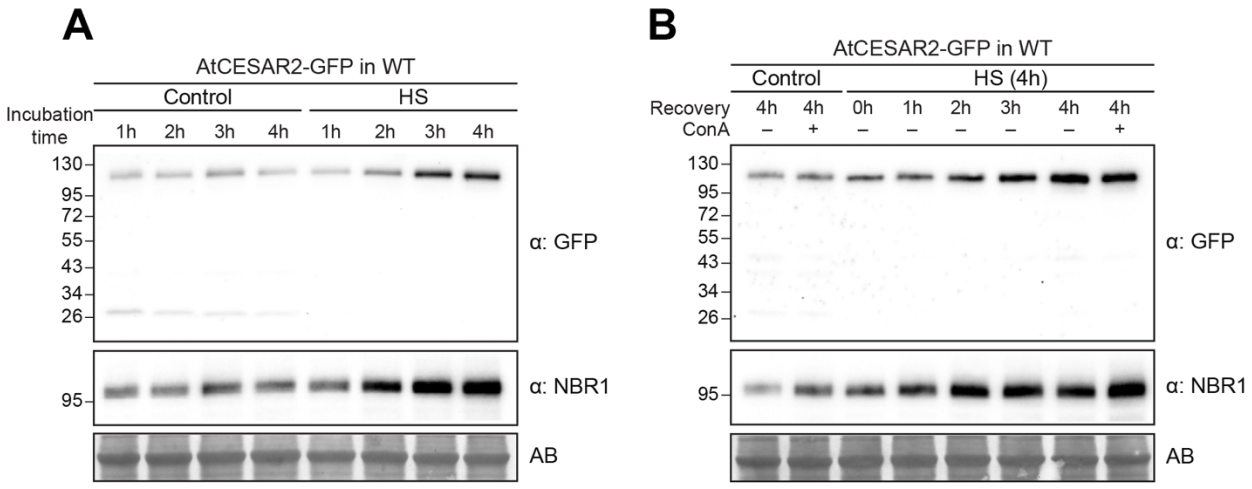

Figure 12. AtCESAR2 protein levels are sensitive to HS. (A) HS stabilizes AtCESAR2 levels. Western blot analysis was performed to detect AtCESAR2-GFP protein levels and endogenous NBR1 levels. Arabidopsis thaliana seedlings were cultivated for 7 days at 21°C on 1/2 MS medium supplemented with MES and 1% sucrose. The seedlings were then subjected to either 21°C (Control) or 37°C (Heat Stress, HS) for the specified durations. **(B) HS followed by recovery stabilizes AtCESAR2 levels.** Western blot was conducted to examine AtCESAR2-GFP and endogenous NBR1 protein levels. Arabidopsis thaliana seedlings were grown for 7 days on 1/2 MS medium

supplemented with MES and 1% sucrose. The seedlings were then exposed to either 21°C (Control) or 37°C (Heat Stress, HS) for 4 hours, followed by the specified recovery periods at 21°C in fresh media with or without 1 µM Concanamycin A (ConA). For both panels, a total of 20 µg of protein extract was loaded per lane and analyzed using immunoblotting with anti-GFP and anti-NBR1 antibodies. The molecular weights of reference proteins (in kDa) are marked on the left side of the blots. Total protein loading was verified through Amidoblack (AB) staining.

Fig.12

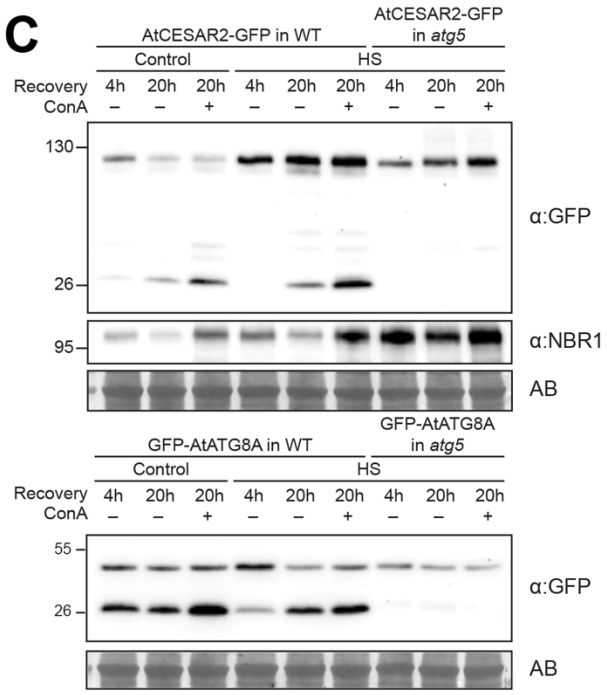

Figure 12 (C) AtCESAR2 undergoes autophagic degradation during extended recovery after HS. Western blot analysis of AtCESAR2-GFP (upper panel) and GFP-AtATG8A (lower panel) autophagic flux assays during recovery from heat stress. *A. thaliana* seedlings were grown in ½ MS + MES + 1% sucrose media for 7 days, then incubated at 21°C (Control) or 37°C (HS) for 4 hours, followed by recovery at 21°C for either 4 or 20 hours in fresh media with or without 1 µM ConA. A total of 20 µg of protein extract was loaded and analyzed via immunoblotting with the indicated antibodies. Two independent biological replicates are shown (see Fig. S7). Protein size markers (kDa) are shown on the left of the blots. Total protein loading was assessed using Amidoblack (AB) staining.

Proteasome inhibition induces AtCESAR2 autophagic flux

Since heat stress disrupts protein homeostasis by promoting protein misfolding in plants, we investigated whether proteotoxic stress induced by proteasome inhibition would similarly affect the autophagic flux of CESAR2-GFP. To explore this, we conducted time-course experiments using Bortezomib, a proteasome inhibitor, to assess its impact on AtCESAR2-GFP protein levels. Remarkably, treatment with 50 μM Bortezomib induced rapid degradation of AtCESAR2-GFP, peaking after 4 hours of incubation, further decreasing after 4 hours of recovery, and disappearing completely after 20 hours (Figures 13A-C, S9A).

To determine whether this degradation is autophagy-dependent and to examine the behavior of CESAR2-GFP puncta in root cells, we combined Bortezomib treatments with Concanamycin A (ConA) in both wild-type and *atg5* mutant plants. In the wild-type background, Bortezomib treatment significantly reduced both the total number and size of CESAR2-GFP puncta in root cells, consistent with protein-level observations (Figures 14A-C).

Fig.13

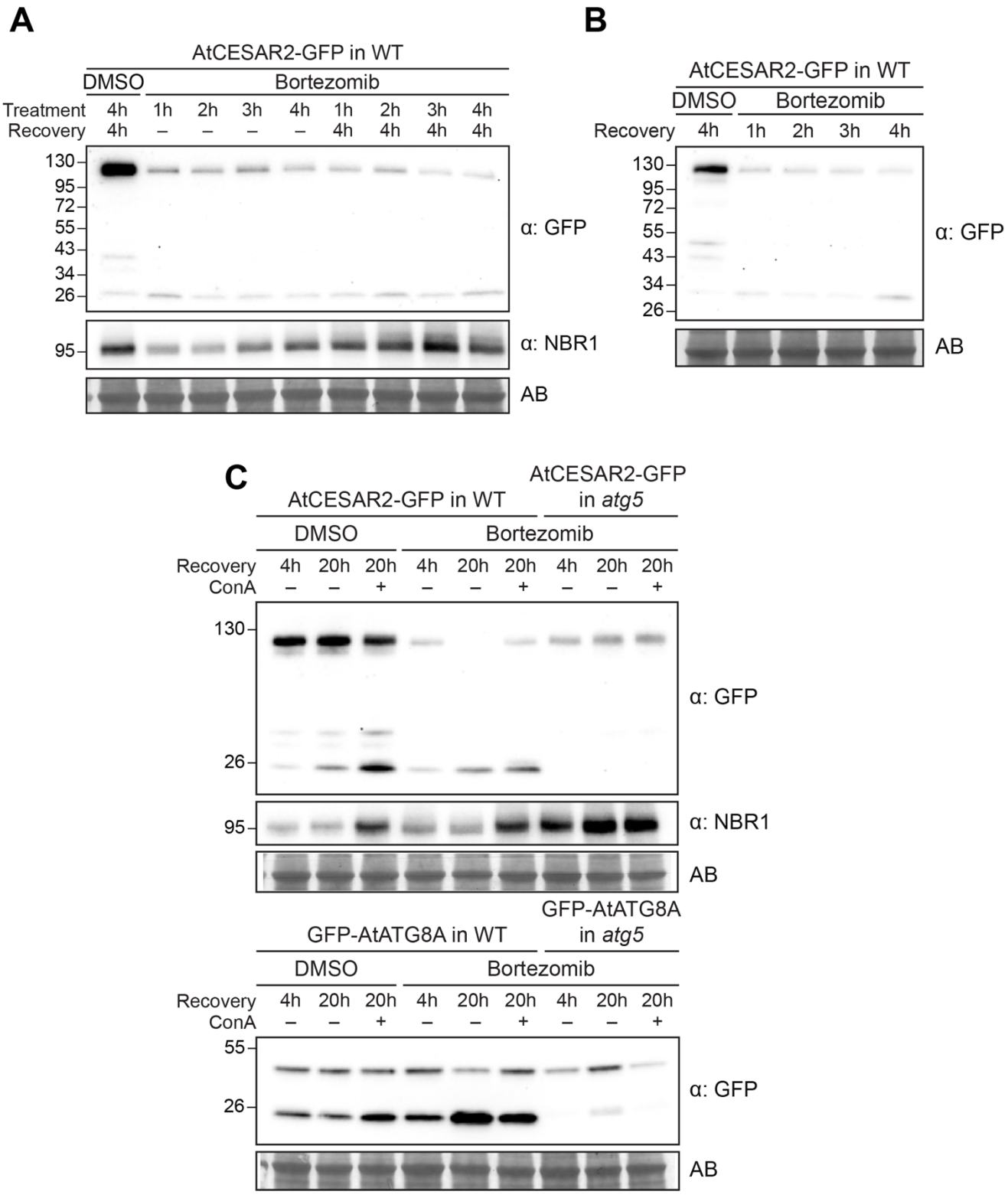
A
AtCESAR2-GFP in WT
DMSO
Bortezomib
Treatment 4h 1h 2h 3h 4h 1h 2h 3h 4h
Recovery 4h – – – – 4h 4h 4h 4h
130
95
72
55
43
34
26
α: GFP
95
α: NBR1
AB
B
AtCESAR2-GFP in WT
DMSO
Bortezomib
Recovery 4h 1h 2h 3h 4h
130
95
72
55
43
34
26
α: GFP
AB
C
AtCESAR2-GFP in WT
AtCESAR2-GFP in atg5
DMSO
Bortezomib
Recovery 4h 20h 20h 4h 20h 20h 4h 20h 20h
ConA – – + – – + – – +
130
26
α: GFP
95
α: NBR1
AB
GFP-AtATG8A in WT
GFP-AtATG8A in atg5
DMSO
Bortezomib
Recovery 4h 20h 20h 4h 20h 20h 4h 20h 20h
ConA – – + – – + – – +
55
26
α: GFP
AB

Figure 13. AtCESAR2 protein levels decrease upon proteasome inhibition in an autophagy-dependent manner. (A) Proteasome inhibition triggers AtCESAR2 degradation. Western blot analysis of AtCESAR2-GFP protein levels and endogenous NBR1 levels following bortezomib treatment. *Arabidopsis thaliana* seedlings were grown in ½ MS + MES + 1% sucrose media for 7 days and incubated at 21°C in media supplemented with either DMSO (Control) for 4 hours followed by a 4-hour recovery in fresh media, or with 50 µM bortezomib for the indicated durations, followed by either no recovery or a 4-hour recovery in fresh media. A total of 20 µg of protein extract was loaded and analyzed via immunoblotting with anti-GFP and anti-NBR1 antibodies. Protein size markers (kDa) are shown on the left of the blots. Total protein loading was assessed using Amidoblack (AB) staining. **(B) AtCESAR2 levels fail to recover after proteasome inhibition.** Western blot analysis of AtCESAR2-GFP protein levels after a 4-hour bortezomib treatment followed by recovery periods ranging from 1 to 4 hours. *A. thaliana* seedlings were grown in ½ MS + MES + 1% sucrose media for 7 days and incubated at 21°C in media supplemented with either DMSO (Control) or 50 µM bortezomib for 4 hours, followed by the indicated recovery times in fresh media. A total of 20 µg of protein extract was loaded and analyzed via immunoblotting with anti-GFP antibody. Protein size markers (kDa) are shown on the left of the blots. Total protein loading was assessed using Amidoblack (AB) staining. **(C) AtCESAR2 undergoes autophagic degradation following proteasome inhibition.** Western blot analyses showing AtCESAR2-GFP (upper panel) and GFP-AtATG8A (lower panel) autophagic flux assays during recovery from proteasome inhibition. *A. thaliana* seedlings were grown in ½ MS + MES + 1% sucrose media for 7 days and incubated in media supplemented with either DMSO or 50 µM bortezomib for 4 hours, followed by recovery periods of either 4 or 20 hours in fresh media with or without 1 µM Concanamycin A (ConA). A total of 20 µg of protein extract was loaded and analyzed via immunoblotting with anti-GFP and anti-NBR1 antibodies. Protein size markers (kDa) are shown on the left of the blots. Total protein loading was assessed using Amidoblack (AB) staining. Biological replicates are found in Fig.S9.

In contrast, in the *atg5* mutant background, the total number of puncta remained unchanged, but puncta size increased significantly (Figures 14A-14C). This was accompanied by the absence of free GFP in autophagic flux assays and the lack of vacuolar puncta, suggesting that impaired vacuolar delivery led to the formation of enlarged cytoplasmic CESAR2 puncta (Figures 13C, S9A, 14A, 14C). A similar trend was observed for GFP-ATG8A in Western blot-based autophagic flux assays in response to Bortezomib (Figures 13C, S9A).

Fig.14

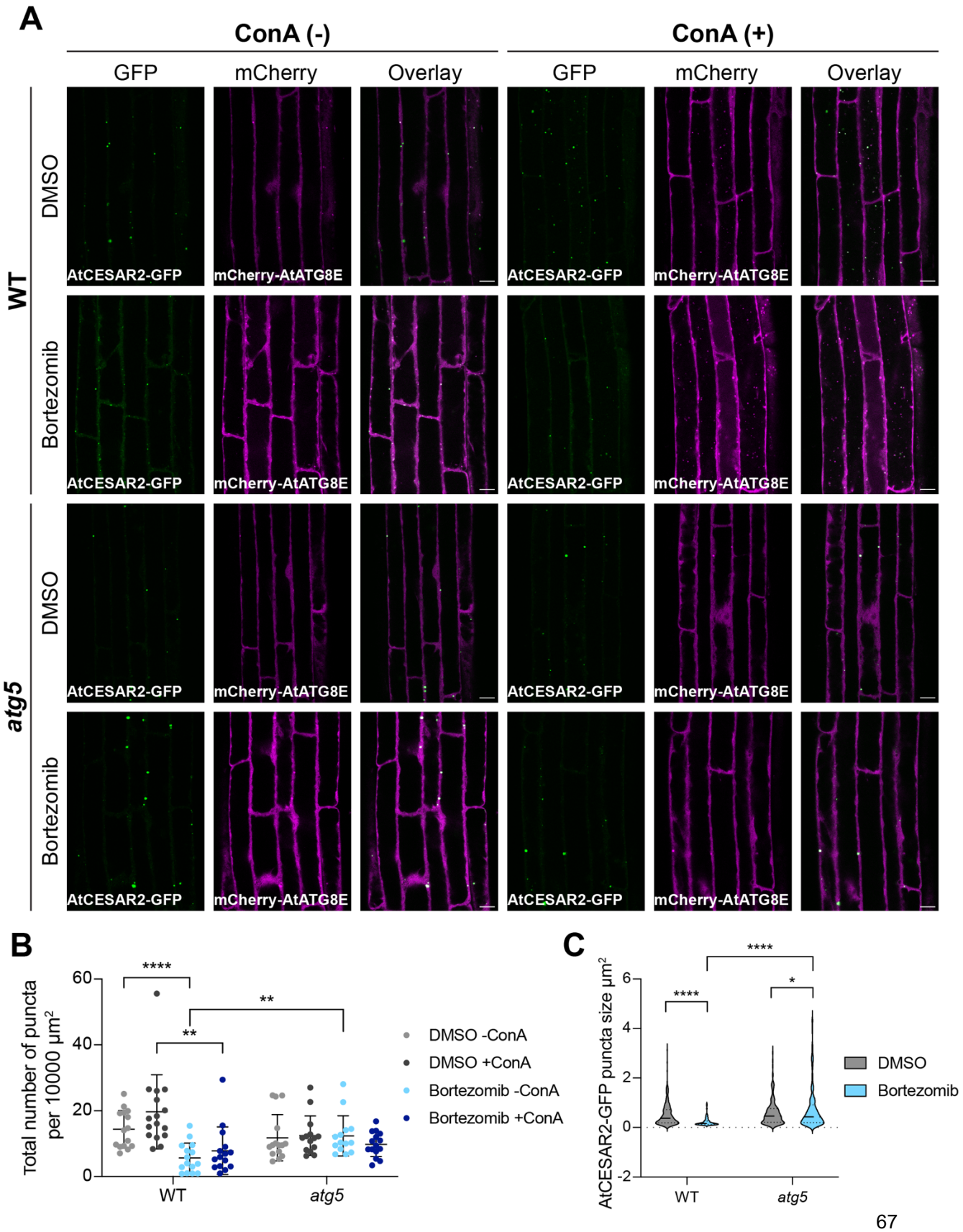
A
ConA (-)
ConA (+)
GFP
mCherry
Overlay
WT
atg5
DMSO
Bortezomib
AtCESAR2-GFP
mCherry-AtATG8E
B
Total number of puncta per 10000 μm²
DMSO -ConA
DMSO +ConA
Bortezomib -ConA
Bortezomib +ConA
WT
atg5
C
AtCESAR2-GFP puncta size μm²
DMSO
Bortezomib

Figure 14. (A) Proteasome inhibition induces AtCESAR2 degradation in an autophagy-dependent manner. Confocal microscopy images of *A. thaliana* root epidermal cells co-expressing AtCESAR2-GFP with mCherry-AtATG8E in wild-type (WT) and *atg5* mutant backgrounds. Five-day-old *A. thaliana* seedlings were incubated for 2 hours at 21°C in ½ MS + MES + 1% sucrose media supplemented with either 50 µM bortezomib or DMSO, followed by a 2.5-hour recovery in fresh media with or without 1 µM Concanamycin A (ConA). Representative images from 14–16 replicates per condition are shown. Scale bars: 10 µm. **(B) Proteasome inhibition reduces the number of AtCESAR2 puncta.** Quantification of confocal microscopy data from Fig. 14A showing the total number of AtCESAR2-GFP puncta per normalized area (10,000 µm²). Bars represent the mean ± SD of 15 replicates for both WT and *atg5* (DMSO – ConA); 16 replicates for WT and 14 for *atg5* (DMSO + ConA); 15 replicates for WT and 14 for *atg5* (bortezomib – ConA); and 15 replicates for WT and *atg5* (bortezomib + ConA). Two-tailed unpaired Student's t-tests with Welch's corrections were used to analyze differences in puncta numbers between DMSO and bortezomib treatments within and between genotypes ± 1 µM ConA. ****, $P < 0.0001$; **, $P < 0.005$ (0.0028). **(C) Proteasome inhibition decreases the size of AtCESAR2 puncta.** Quantification of confocal microscopy data from Fig. 14A showing the area size (µm²) of AtCESAR2-GFP puncta. A total of 218 and 191 puncta were quantified for WT and *atg5*, respectively, under DMSO treatment, and 94 and 192 puncta for WT and *atg5*, respectively, under bortezomib treatment. Two-tailed unpaired Student's t-tests with Welch's corrections were used to analyze differences in puncta sizes between WT and *atg5* backgrounds under bortezomib and DMSO treatments. ****, $P < 0.0001$; *, $P < 0.05$ (0.0228).

To explore the effects of proteasome inhibition in *CESAR1* and *CESAR2* gene expression, we analyzed the levels of *CESAR1* and *CESAR2* gene transcripts in response to this treatment. Bortezomib treatment upregulated the expression of both genes in both wild-type and *atg5* mutant backgrounds, revealing a clear divergence between their responses at the mRNA and protein levels (Figure S9B).

Finally, we tested whether CB treatment could also induce AtCESAR2 flux. Time-course experiments showed a significant increase in AtCESAR2 flux, consistent with our findings from proteasome inhibition assays (S10).

In summary, these results demonstrate that the autophagic degradation of AtCESAR2 is activated in response to proteotoxic stress.

CESAR potentially functions as an aggrephagy receptor

Our results so far suggested that CESAR functions as a SAR. Consequently, we sought to identify the cargo and elucidate the mechanism underlying CESAR-mediated autophagy. Structural predictions using AF2 indicated the presence of a highly conserved three-helix bundle domain, a feature typical of CUE (Coupling of Ubiquitin to ER degradation) domains, in the N-terminal region of the protein (Figure 16A).

Since previous research has shown that CUE domains from various organisms can bind ubiquitin, we hypothesized that CESAR functions as an aggrephagy receptor, targeting ubiquitinated misfolded proteins for degradation. To test this hypothesis, we performed *in vitro* pulldown assays using MpCESAR, as *M. polymorpha* contains only a single CESAR protein. Truncation experiments revealed that MpCESAR interacts with monoubiquitin as well as M1-linked di- and tetra-ubiquitin chains in a CUE domain-dependent manner (Figure 16B, 16C). To determine its specificity for different ubiquitin chain linkages, we purified the MpCESAR CUE domain and found that it binds to all seven linkage types (M1, K6, K11, K29, K33, K48, and K63), indicating no apparent specificity *in vitro* (Figure 16D).

Next, we investigated whether CESAR associates with ubiquitinated proteins in vivo using Tandem Ubiquitin Binding Entities (TUBE) technology (Hjerpe et al., 2009). For this assay, we compared two treatment conditions: heat stress (HS) and Bortezomib (B). To achieve this, we optimized a short-term, low-dose Bortezomib shorter treatment that did not cause acute degradation of AtCESAR2-GFP but stabilized polyubiquitin chains (Figure S11A, S11B). TUBE pull-down assays revealed that both AtCESAR1 and AtCESAR2 associated with soluble ubiquitinated species, with enhanced association observed under the stress conditions tested (Figure 16E-H). As expected, we also observed an interaction between NBR1 and the TUBEs (Figure S11C-F).

Collectively, these findings demonstrate that CESAR binds ubiquitin via its CUE domain and is recruited to ubiquitinated proteins during proteotoxic stress.

Heat stress and proteasomal inhibition lead to the buildup of misfolded proteins, which frequently aggregate and are generally insoluble (Hyun et al., 2003; Zhou et al., 2013). We therefore examined whether CESAR associates with insoluble ubiquitinated species. Using ultracentrifugation, we fractionated soluble and insoluble protein fractions and analyzed CESAR partitioning through western blotting. These experiments showed that both AtCESAR paralogs were enriched in the insoluble fraction under heat stress, alongside ubiquitinated proteins and NBR1 (Figure 16I, Figure 16J). Notably, this process was reversible upon sonication, indicating active recruitment of CESAR to the insoluble fraction rather than passive aggregation (Figure 16K). Taken together, these results suggest that CESAR may target insoluble ubiquitinated protein aggregates for autophagic degradation.

To visualize protein aggregates *in vivo* and evaluate their colocalization with AtCESAR2, we utilized the PROTEOSTAT Aggregation Assay (Enzo), which emits enhanced red fluorescence upon binding to aggregated proteins, in Arabidopsis seedlings expressing AtCESAR2-GFP. However, the observed signal appeared nonspecific (data not shown). Additionally, we attempted to generate lines co-expressing AtCESAR2-mCherry with the GFP-FL2ΔSP aggregate reporter (Jung et al., 2020a). Despite this effort, no detectable reporter signal was observed under either heat stress or Bortezomib treatment (data not shown).

Therefore, while our results indicate that CESAR may act as an aggrephagy receptor, additional *in vivo* experiments are required to confirm this role and to further elucidate the mechanistic details of the process.

Fig.16

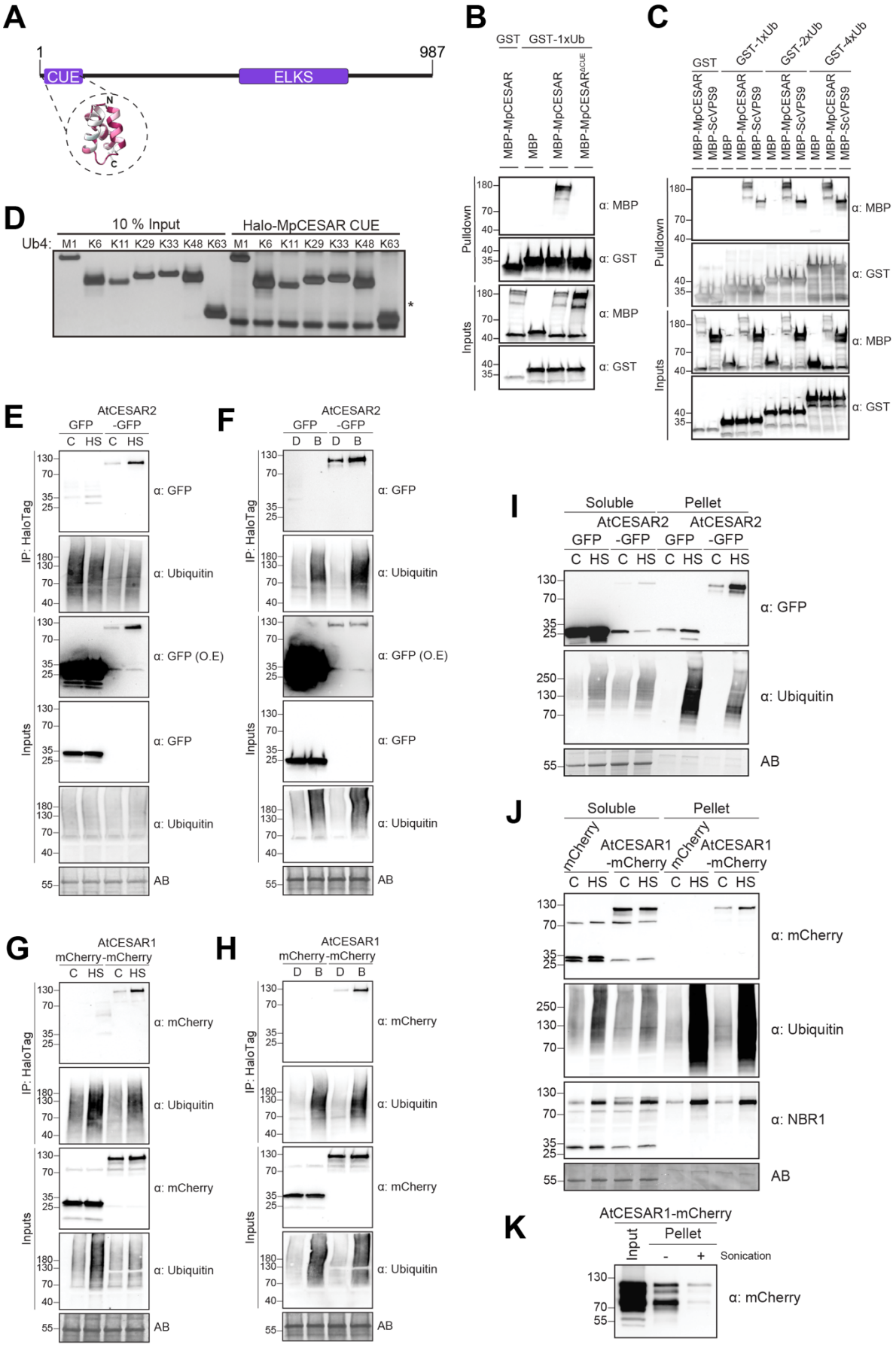
A
1
987
CUE
ELKS
N
C
B
GST
GST-1xUb
MBP-MpCESAR
MBP
MBP-MpCESAR
MBP-MpCESARΔCUE
Pulldown
Inputs
α: MBP
α: GST
C
GST
GST-1xUb
GST-2xUb
GST-4xUb
MBP-MpCESAR
MBP-ScVPS9
MBP
D
10 % Input
Halo-MpCESAR CUE
Ub4:
M1 K6 K11 K29 K33 K48 K63
E
AtCESAR2
GFP
-GFP
C HS C HS
IP: HaloTag
Inputs
α: GFP
α: Ubiquitin
α: GFP (O.E)
AB
F
AtCESAR2
D B D B
G
AtCESAR1
mCherry-mCherry
α: mCherry
H
I
Soluble
Pellet
AtCESAR2
GFP
-GFP
J
mCherry
AtCESAR1
-mCherry
α: NBR1
K
AtCESAR1-mCherry
Input
Pellet
-
+
Sonication

Figure 16. (A) CESAR has a conserved CUE domain. Protein domain architecture of MpCESAR. The CUE and ELKS-Rab6 interacting/CAST family member 1 (ELKS) domains are highlighted in purple. (B-C) **MpCESAR binds ubiquitin *in vitro via its CUE domain*.** MpCESARΔCUE=MpCESAR47-987. Bacterial lysates containing recombinant protein were mixed and pulled down with glutathione magnetic agarose beads. Input and bound proteins were visualized by immunoblotting with anti-GST or anti-MBP antibodies. *S. cerevisiae* (Sc) VPS9 was used as positive control (C). **(D) MpCESAR CUE binds different ubiquitin chain linkages with similar affinities.** Halo-tagged MpCESAR CUE coupled to HaloLink resin was incubated with tetra-ubiquitin (Ub4) of the indicated linkage types. The captured materials were separated on 4-12% SDS-PAGE gel and silver stained. The asterisk indicates non-specific bands from Halo-MpCESAR CUE which have a similar electrophoretic mobility as K63-Ub4 chains. (**E-F) Proteotoxic stress enhances AtCESAR2 association with TUBEs.** 5-d-old *A. thaliana* seedlings expressing GFP-EV (GFP) or AtCESAR2-GFP in wild-*type* (Col-0) background were incubated in liquid ½ MS medium with 1% sucrose for 4h at 21ºC (Control, C) or 37ºC (Heat stress, HS) followed by 4h recovery phase at 21ºC (panel E) or for 1h at 21ºC in DMSO (D)-supplemented or 5 µM Bortezomib (B)-supplemented media followed by 1h recovery phase in fresh media (panel F) and used for co-immunoprecipitation. Plant lysates were incubated with Magne® HaloTag ® Beads conjugated with HaloTag-TUBE. Input and bound proteins were detected by immunoblotting using the respective antibodies as indicated. Total protein loading control was analysed by Amidoblack (AB) staining. Immunoblotting for bait is shown in Fig. S11C (related to Fig. 16E) and Fig. S11D (related to Fig. 16F). **(G-H) Proteotoxic stress enhances AtCESAR1 association with TUBEs.** 5-d-old *A. thaliana* seedlings expressing mCherry-EV (mCherry) or AtCESAR1-mCherry in wild-*type* (Col-0) background were incubated in liquid ½ MS medium with 1% sucrose for 4h at 21ºC (Control, C) or 37ºC (Heat stress, HS) followed by 4h recovery phase at 21ºC (panel G) or for 1h at 21ºC in DMSO (D)-supplemented or 5 µM Bortezomib (B)-supplemented media followed by 1h recovery phase in fresh media (panel H) and used for co-immunoprecipitation. Plant lysates were incubated with Magne® HaloTag ® Beads conjugated with HaloTag TUBE. Input and bound proteins were detected by immunoblotting using the respective antibodies as indicated. Total protein loading control was analysed by Amidoblack (AB) staining. Immunoblotting for bait is shown in Fig. S11E (related to Fig. 16G) and Fig. S11F (related to Fig. 16H). **(I-J) HS increases CESAR localization to the insoluble fraction.** 5-d-old *A. thaliana* seedlings expressing either GFP-EV (GFP) or AtCESAR2-GFP (panel I), either mCherry-EV (mCherry) or AtCESAR1-mCherry (panel J) in wild-*type* (Col-0) background were incubated in liquid ½ MS medium with 1% sucrose for 4h at 21ºC (Control, C) or 37ºC (Heat stress, HS) followed by 4h recovery phase at 21ºC. Soluble and pellet fractions were separated by centrifugation and normalized before immunoblotting using the respective antibodies as indicated. Total protein loading control was analysed by Amidoblack (AB) staining. **(K)**

CESAR partitioning to the insoluble fraction is reversible. 5-d-old *A. thaliana* seedlings expressing AtCESAR1-mCherry in wild-*type* (Col-0) background were incubated in liquid ½ MS medium with 1% sucrose for 4h at 37ºC followed by a 4-hour recovery phase at 21ºC. Soluble (input) and pellet fractions were separated by centrifugation, and pellet fraction was further sonicated in a water bath before immunoblotting using the respective antibodies as indicated.

Part 3: The physiological role of CESAR in organismal homeostasis

CESAR is necessary for proteotoxic stress tolerance

Our results suggested that CESAR has a role in restoring protein homeostasis, particularly during proteotoxic stress recovery. To investigate the physiological significance of CESAR-mediated autophagy during heat stress, we generated a double mutant, *cesar1cesar2*. Homozygous plants were identified through genotyping PCR, and the expression of *CESAR1* and *CESAR2* transcripts in the double mutant was analyzed using qPCR with primers designed downstream of the T-DNA insertion sites. The analysis revealed that *CESAR1* expression was undetectable, while *CESAR2* expression was reduced by approximately 75%, suggesting that *cesar1cesar2* functions as a knockout mutant for *CESAR1* and a knockdown for *CESAR2* (Figure S12). Although we were unable to evaluate CESAR protein levels due to the lack of an antibody capable of detecting endogenous CESAR proteins, the qPCR results provided sufficient evidence to proceeding with phenotypic assays on the identified double mutant.

Initially, we assessed the sensitivity of the *cesar1 cesar2* mutant to carbon and nitrogen starvation, as nutrient starvation typically induces bulk degradation rather than selective autophagy (Ren et al., 2014). Unlike the *atg5* mutant, in which autophagy is inhibited, the *cesar1 cesar2* mutant did not exhibit increased sensitivity to either carbon or nitrogen starvation (Figure 17A, Figure S13A). As expected, the *nbr1* mutant also showed no sensitivity to these starvation conditions (Figure 17A, Figure S13A).

Next, we investigated the response of *cesar1 cesar2* plants to two types of proteotoxic stress: heat stress and proteasome inhibition, using *nbr1* and *atg5* mutants as positive controls. Under normal growth conditions, *cesar1 cesar2* plants were noticeably smaller than wild-type plants, indicating that CESAR-mediated autophagy is essential for maintaining cellular homeostasis in control conditions (Figure 17B, upper panel; Figure 17C). After exposure to heat stress, *cesar1 cesar2* plants were unable to restore growth, with their rosette area reduced by 3.3-fold relative to control plants (Figure 17B, lower panel; Figure 17C, right panel). Furthermore, *cesar1 cesar2* plants exhibited greater sensitivity to heat stress than *nbr1* mutants (Figures 17B, 17C). These findings highlight the critical role of CESAR in heat stress tolerance.

Given the reported crosstalk between the Ubiquitin Proteasome System (UPS) and selective autophagy (Raffeiner et al., 2023), we investigated whether proteasome activity is affected in *cesar1 cesar2* plants during heat stress recovery. Proteasome activity was measured under both normal and heat stress conditions. The results revealed that cesar1 cesar2 plants exhibited constitutively higher trypsin-like proteasome activity compared to wild-type plants (Figure S13B), suggesting that proteasomal activity was upregulated as a compensatory mechanism for impaired selective autophagy.

Altogether, these results suggest that the absence of CESAR may lead to the accumulation of misfolded or aggregated proteins, which negatively impacts plant growth and triggers compensatory proteasome activation.

To validate the proteasome activity findings, we tested the sensitivity of *cesar1 cesar2* plants to proteasome inhibition. On Bortezomib-containing plates, the survival rates of *cesar1 cesar2* and *atg5* mutants were significantly lower than those of wild-type plants. The *nbr1* mutant also showed reduced survival, albeit to a lesser extent (Figures 17D, 17E, S13C, S13D).

In conclusion, our results demonstrate that CESAR-mediated autophagy is crucial for plant survival under proteotoxic stress. It plays a key role in maintaining protein homeostasis, likely by facilitating the degradation of ubiquitinated hydrophobic proteins.

Fig.17

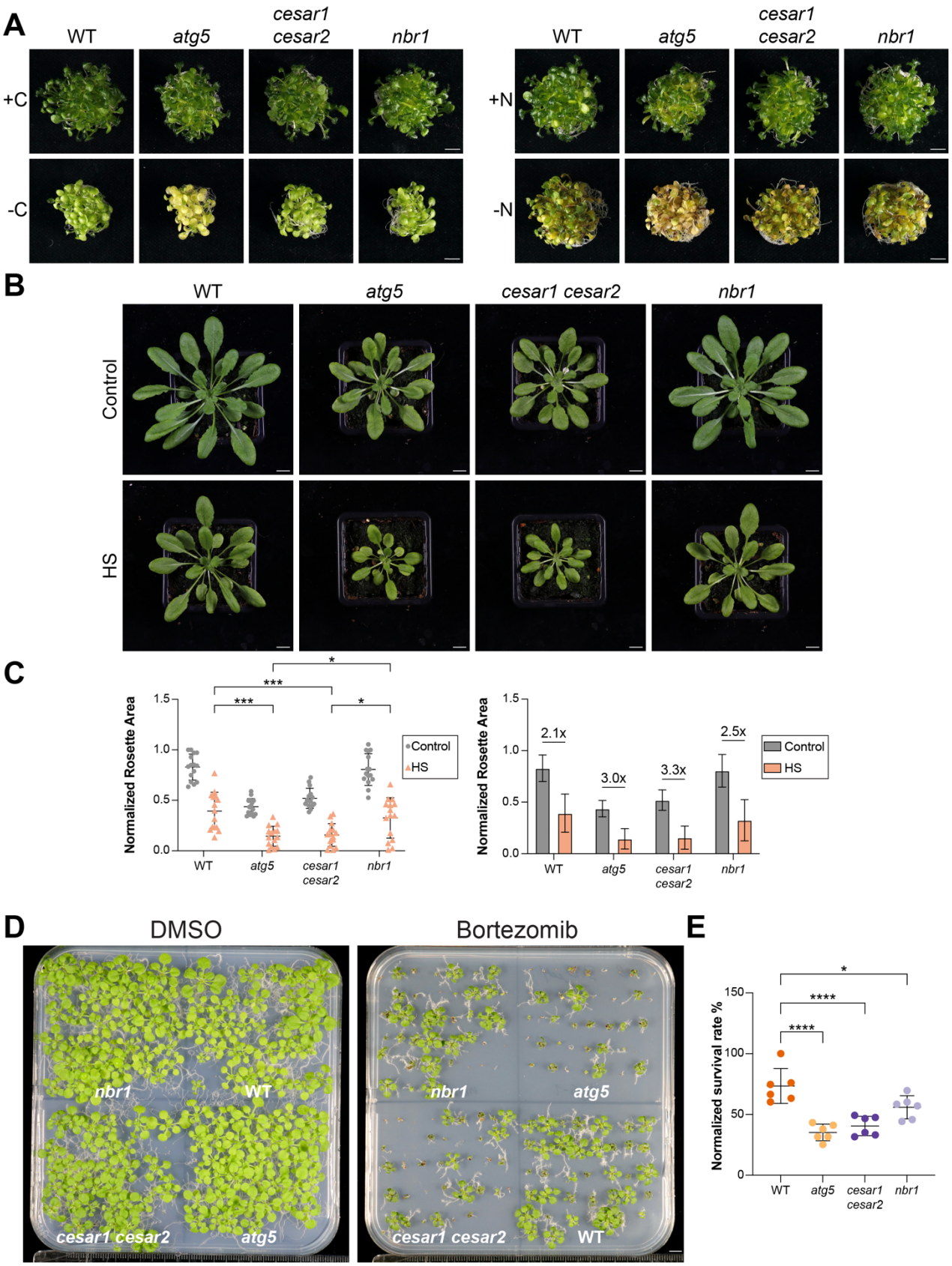
A
WT
atg5
cesar1 cesar2
nbr1
+C
-C
+N
-N
B
Control
HS
C
Normalized Rosette Area
Control
HS
2.1x
3.0x
3.3x
2.5x
D
DMSO
Bortezomib
nbr1
WT
atg5
cesar1 cesar2
E
Normalized survival rate %

Figure 17. CESAR is essential for proteotoxic stress tolerance. (A) The cesar1cesar2 mutant is not hypersensitive to carbon or nitrogen starvation. Nine-day-old *Arabidopsis thaliana* seedlings of the indicated genotypes were grown in ½ MS + MES + 1% sucrose for 9 days, followed by either 4 days of carbon starvation (-C, left) or 6 days of nitrogen starvation (-N, right). Images show seedlings at 13 and 15 days old, respectively. Representative images from three independent biological replicates per genotype are shown (see Fig. S13A). Scale bar: 1 cm. **(B) The cesar1cesar2 mutant is sensitive to heat stress.** *A. thaliana* plants of the indicated genotypes were grown in soil under an 8-hour light/16-hour dark photoperiod at 21°C for 3 weeks. Plants were then subjected to either 21°C (Control) or 37°C (Heat stress, HS) for 3 days without watering, followed by an 18-day recovery period at 21°C. Images were taken of 42-day-old plants. Representative images for each genotype are shown. Scale bar: 1 cm. **(C) Rosette area quantification and statistical analysis. Left panel:** Rosette areas were measured for each plant and normalized to the maximum rosette area of wild-type (Col-0) plants at 21°C. An ordinary one-way ANOVA with Tukey's multiple comparisons test was used to evaluate differences in normalized rosette area between genotypes at 37°C (HS). ***, Adjusted P < 0.001 (0.0003 for WT vs *atg5*; 0.0006 for WT vs *cesar1cesar2*); *, Adjusted P < 0.05 (0.0121 for *atg5* vs *nbr1*; 0.0219 for *cesar1cesar2* vs *nbr1*). Non-significant differences are not shown. **Right panel:** Size factor differences between normalized rosette areas for the indicated genotypes are shown. **(D) The cesar1cesar2 mutant is sensitive to proteasome inhibition.** *A. thaliana* seedlings of the indicated genotypes were grown on 1% agar ½ MS + MES + 1% sucrose plates supplemented with either DMSO (left plate) or 3.75 µM bortezomib (right plate) for 18 days before imaging. Representative images from six independent biological replicates are shown (n = 40 seeds per genotype per replicate). Scale bar: 1 cm. **(E) Quantification of the survival rate of seedlings grown on bortezomib-containing plates.** The normalized survival rate for the bortezomib plate assay shown in Fig. 17D is presented. The survival rate for each replicate was calculated by dividing the number of seedlings with a phenotype of size greater than 0.3 cm and green coloration by the total number of seeds sown per genotype (40). This value was then normalized to the highest survival rate observed for the wild-type (Col-0) background across all six biological replicates (n = 240; each dot represents a replicate with 40 seeds per genotype per plate). An ordinary one-way ANOVA with Tukey's multiple comparisons test was used to evaluate differences in survival rates between genotypes. ****, Adjusted P < 0.0001; *, Adjusted P < 0.05 (0.0322). Non-significant differences are not shown.

Part 4: CESAR2 and NBR1 crosstalk

CESAR2 colocalizes with NBR1 under control and heat stress conditions

Our interactome analysis and TUBE-pulldown assays revealed that CESAR1/2 proteins exhibit an enrichment pattern similar to NBR1. This led us to hypothesize that CESAR1/2 and NBR1 function within the same autophagic pathway to facilitate protein aggregate clearance.

To test this, we generated transgenic *Arabidopsis thaliana* lines co-expressing fluorescently tagged AtCESAR2 and AtNBR1 and subjected them to heat stress. Confocal microscopy of root cells showed a high degree of colocalization between AtCESAR2-mCherry and GFP-NBR1 puncta under both control and heat stress recovery conditions, with no significant differences between treatments (Figures 18A, 18B). This suggests a potential association between AtCESAR2 and AtNBR1, possibly alongside AtCESAR1, which we previously demonstrated to colocalize with AtCESAR2 (Figure 9).

Further structural predictions using AlphaFold2 (AF2) identified a potential interaction interface between the ubiquitin-binding domains of AtCESAR2 and AtNBR1, CUE domain and UBA2 domain, respectively (Figure 18C). If accurate, this spatial proximity could enhance cooperative binding affinities for ubiquitinated cargo.

The autophagic degradation of AtCESAR2 upon proteasome inhibition is impaired by the absence of NBR1

We hypothesized that if AtCESAR2 and AtNBR1 operate within the same autophagic pathway, the absence of AtNBR1 could alter AtCESAR2 autophagic flux and *vice versa*. We conducted autophagic flux assays under heat stress and proteasome inhibition treatments in both WT and *nbr1* mutant backgrounds expressing AtCESAR2-GFP.

A slight reduction in AtCESAR2-GFP flux was observed in *nbr1* mutants under both control and heat stress conditions compared to WT (Figures 19A and S14A). However, upon Bortezomib treatment, AtCESAR2 autophagic degradation was significantly impaired in the *nbr1* mutant, indicating that NBR1 is essential for efficient autophagic

degradation of CESAR2 (Figures 19B and S14B). These findings suggest that CESAR2 and NBR1 likely function within the same autophagic pathway and cooperate to efficiently degrade shared cargo, particularly when proteasomal activity is compromised.

Fig.18

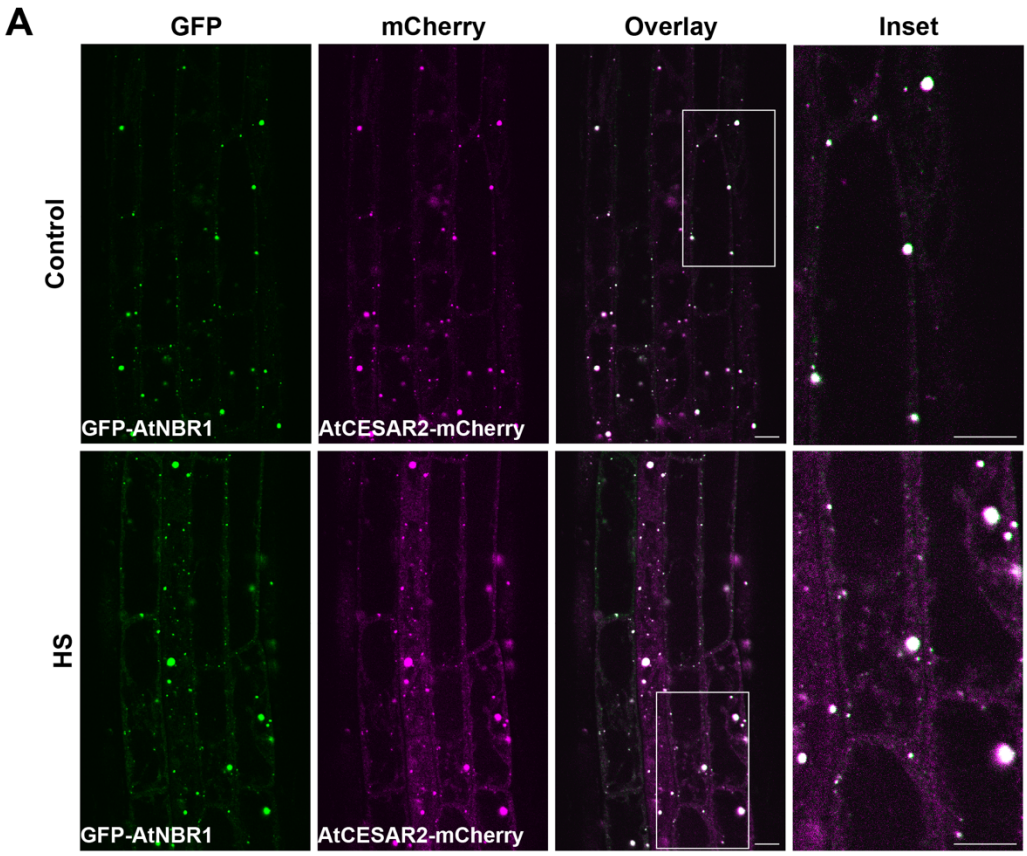

Figure 18. (A) AtCESAR2 colocalizes with AtNBR1. Confocal microscopy images of *Arabidopsis thaliana* root epidermal cells co-expressing AtCESAR2-mCherry with GFP-NBR1 or GFP-EV (empty vector) (shown in Figure S15B). Five-day-old *A. thaliana* seedlings were grown on 1% agar ½ MS + MES + 1% sucrose plates and incubated at 21°C (Control) or 37°C (HS) for 3 hours, followed by a 3-hour recovery at 21°C before imaging. Representative images from 13 biological replicates are shown. The white-boxed region in the merged panel is enlarged in the inset. Scale bars: 10 μm for both the main image and inset. The white-boxed region in the merged panel is enlarged in the inset. Scale bars: 10 μm for both the main image and inset.

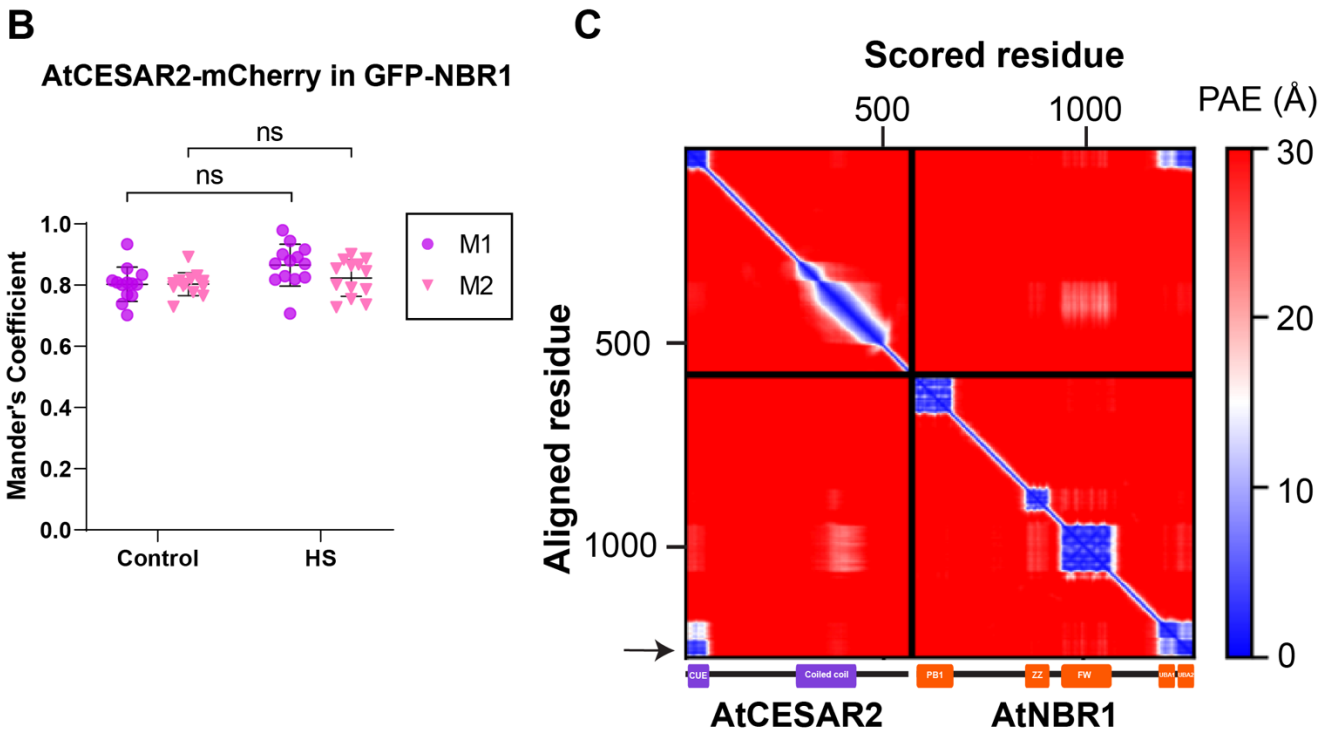

Figure 18. (B) AtCESAR2 and AtNBR1 show a high degree of colocalization in control and heat stress conditions. Quantification of confocal microscopy data from Fig. 18A, using Mander's colocalization coefficients to measure overlap between AtCESAR2-mCherry and GFP-AtNBR1 signals. M1 represents the fraction of GFP-AtNBR1 signal overlapping with AtCESAR2-mCherry, while M2 represents the fraction of AtCESAR2-mCherry signal overlapping with GRP-NBR1. Bars represent the mean ± SD from 13 biological replicates. Two-tailed unpaired Student's t-tests was performed to assess the significance of differences in M1 and M2 values between Control (21°C) and HS (37°C) conditions. ns, no significant. **(C) AF2 predicts CESAR2 and NBR1 interaction, via their respective ubiquitin binding domains CUE (N-term) and UBA2, respectively (C-term)**. Predicted interaction interfaces of CESAR2 and NBR1, generated using AlphaFold multimer. The graphs depict inter-residue predicted aligned error (PAE) values, where lower scores indicate higher confidence in the interaction. Interface residues are highlighted in blue, with non-interface residues in red. Black arrow indicates predicted interface.

Fig.19

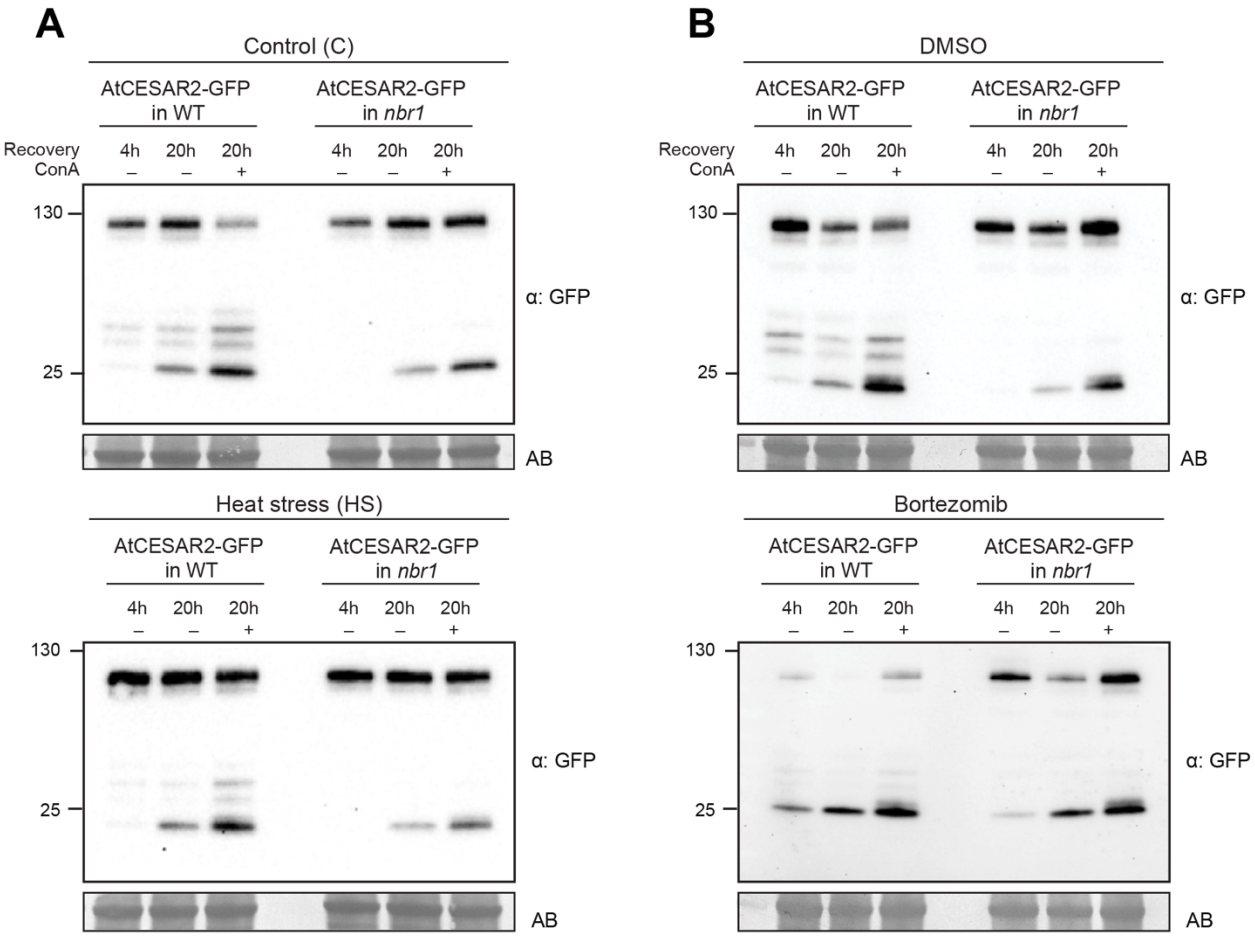

Figure 19. (A) AtCESAR2 autophagic flux decreases in the absence of NBR1. Western blot analyses showing AtCESAR2-GFP autophagic flux assays under control (upper panel) and heat stress (lower panel) in WT and *nbr1* mutant backgrounds. **(B) AtCESAR2 autophagic flux is impaired in the absence of NBR1 upon proteasomal inhibition.** Western blot analyses showing AtCESAR2-GFP autophagic flux assays under DMSO (upper panel) and Bortezomib (lower panel) treatments in WT and nbr1 mutant backgrounds. *A. thaliana* seedlings were grown in ½ MS + MES + 1% sucrose media for 7 days and incubated with the respective treatments for 4 hours, followed by recovery periods of either 4 or 20 hours in fresh media with or without 1 µM Concanamycin A (ConA). A total of 20 µg of protein extract was loaded and analyzed via immunoblotting with anti-GFP antibodies. Protein size markers (kDa) are shown on the left of the blots. Total protein loading was assessed using Amidoblack (AB) staining. Biological replicates are found in Fig.S14.

DISCUSSION

CESAR as a novel selective autophagy receptor

In this study, thanks to a comparative interactome approach we identified CESAR, a conserved AIM-dependent ATG8 interactor, and characterized its role as a SAR essential for heat stress tolerance in *Arabidopsis thaliana*. Our findings suggest that CESAR, via its CUE domain binds to and targets ubiquitinated protein aggregates for degradation, thereby maintaining protein homeostasis. However, additional experiments, such as assessing the enrichment of ubiquitinated proteins in the absence of CESAR and employing *in vivo* approaches to visualize protein aggregates (e.g., aggregate reporters), are necessary to confirm this mechanism.

In a recent preprint, it was proposed that AtCESAR1 (identified as ERC1 in that study) phase-separates into membraneless condensates that act as scaffolds during autophagosome formation, suggesting a role in autophagosome biogenesis initiation (Chung et al., 2024). However, the ability to form protein condensates and induce autophagosome biogenesis has also been described for SARs such as p62 and NBR1 (Adriaenssens et al., 2022). These findings could indicate that CESAR proteins condensate to initially sequester misfolded proteins and subsequently recruit the autophagy machinery around them.

The growth defects observed in the *cesar1cesar2* mutant could potentially be attributed to the accumulation of protein aggregates. To further validate that the observed phenotype results from impaired autophagic degradation of misfolded proteins and protein aggregates, complementation assays using CESAR variants lacking the AIM motif or CUE domain should be performed. Additionally, we cannot rule out the possibility that the observed phenotype may be due to autophagy-independent functions of CESAR. In addition, it would be valuable to investigate whether CESAR1 and CESAR2 can function as SARs independently of one another and to uncover any paralog-specific functions.

Notably, consistent with our findings, Chung and colleagues reported heat stress sensitivity in the *cesar1* mutant, while no significant effect was observed in the *cesar2* mutant (Chung et al., 2024). To determine the primary driver of the observed phenotype in our assays, it is crucial to evaluate heat stress tolerance in the single mutants used to generate the *cesar1 cesar2* double mutant. Additionally, the use of different T-DNA insertion lines in that study compared to those tested by us, further supports the validity of the heat stress phenotype.

CESAR undergoes autophagic degradation following extended recovery post-heat stress

Our findings show that CESAR2 and ATG8 levels are stabilized in the cytoplasm following heat stress treatments, with increased co-localization between CESAR2 and AtATG8 puncta. Autophagic flux resumes only after prolonged recovery, as observed through Western blot-based assays. These results align with previous studies, which also reported delayed autophagic degradation after heat stress and its reestablishment during extended recovery (Jung et al., 2020b).

A recent study further dissected autophagy induction post-heat stress, revealing that autophagosomes transition from solid to circular structures between 6 and 9 hours of recovery, with autophagic bodies significantly increasing in vacuoles by 9–12 hours (Li et al., 2024). These findings are consistent with our Western-based autophagic flux assays and explain the low number of CESAR2 puncta inside vacuoles upon Concanamycin treatment after 3 hours of recovery following heat stress (Figures 11A and 11B).

This suggests that cargo autophagosome biogenesis is temporally uncoupled from autophagosome maturation and degradation, likely due to a temporary slowdown or halt in autophagic activity following heat stress. The delay in autophagic degradation was recently attributed to the translocation of key autophagy components, to heat stress-induced stress granules. These granules disassemble and release ATG proteins as recovery progresses, allowing autophagy to resume and degrade heat-induced ubiquitinated aggregates (Li et al., 2024).

These findings highlight the complexity of the heat stress response, which relies on the coordinated action of multiple factors, including stress granules, alongside key quality control pathways to efficiently restore cellular homeostasis during recovery. Furthermore, they highlight the precise regulation of selective autophagy as an essential component of the cellular stress response. Understanding the signaling mechanisms that regulate the different steps of selective autophagy is critical to uncovering how this system executes responses with spatiotemporal precision.

Proteasome inhibition triggers rapid CESAR2 autophagic degradation as opposed to heat stress

In response to heat stress, CESAR2 was initially stabilized and subsequently degraded during prolonged recovery. In contrast, proteasomal inhibition resulted in rapid and extensive CESAR degradation via autophagy, accompanied by a significant reduction in both the number and size of CESAR puncta.

We propose that proteasome inhibition causes a faster and more pronounced accumulation of misfolded species and protein aggregates compared to the heat stress conditions examined. This, combined with the upregulation of selective autophagy triggered by proteasome inhibition, could drive a stronger and more rapid CESAR-mediated autophagic response.

These results also suggest that selective autophagy is regulated by distinct mechanisms depending on the type of stress encountered, underscoring the importance of understanding how stress signals are detected and integrated by selective autophagy components.

Furthermore, the enlarged CESAR2 puncta observed in the autophagy mutant following Bortezomib treatment likely reflect the accumulation of protein aggregates, supporting the hypothesis that CESAR targets protein aggregates for degradation.

NBR1 and CESAR1/2 functioning together?

Our results demonstrated that NBR1 and CESAR2 puncta colocalize in *Arabidopsis* root cells under both control and heat stress conditions, suggesting that these proteins may associate to form heterooligomers. AlphaFold predictions indicate that the CUE domain of CESAR2 interacts with the UBA domains of NBR1, primarily UBA2. The same was observed for CESAR1 and NBR1 (data not shown). This interaction may enhance ubiquitin-binding affinity through cooperative action of both ubiquitin-binding domains, potentially resulting in more efficient ubiquitinated cargo binding, as previously proposed for p62 and NBR1 (Turco et al., 2021). However, the direct interaction between CESAR proteins and NBR1 should be validated through *in vitro* pulldown assays. While the interaction between the UBA domain of NBR1 and CESAR1 has been confirmed (Chung et al., 2024), further studies are needed to assess the interaction between their ubiquitin-binding domains and determine their affinity for ubiquitin.

To determine whether the ubiquitin-binding domains are required for protein colocalization *in vivo*, *nbr1* mutants should be complemented with a truncated version of NBR1 lacking the UBA domains (ΔUBA) to test its ability to associate with CESAR proteins.

Notably, we observed a decreased autophagic flux of CESAR2 in the absence of NBR1, particularly under proteasome inhibition. This finding suggests that NBR1 and CESAR2 function within the same autophagic pathway and that their association may be necessary for the efficient degradation of shared cargo. To investigate whether autophagy machinery recruitment is impaired in the absence of NBR1, CESAR colocalization with ATG8 should be assessed in the *nbr1* mutant background. Similarly, the colocalization of NBR1 with ATG8 should be evaluated in the absence of CESAR1/2 proteins. Additionally, the autophagic flux of ATG8 should be evaluated in the absence of these proteins.

Reciprocal experiments should also assess the autophagic flux of NBR1 in *cesar1 cesar2* mutants. Preliminary data (data not shown) and recent findings (Chung et al., 2024) suggest that NBR1 is upregulated in the absence of CESAR proteins. However, to

confirm whether this regulation occurs at the protein level, and to perform autophagic flux assays, transgenic lines expressing GFP-NBR1 under a constitutive promoter should be generated.

Finally, *in vitro* reconstitution assays should be conducted to elucidate the interactions and recruitment hierarchy among CESAR1, CESAR2, and NBR1, as well as their interactions with other components of the selective autophagy machinery, such as ATG11. These experiments would provide valuable mechanistic insights into CESAR- and NBR1-mediated degradation.

CONCLUSION

In conclusion, comparative approaches across species serve as a powerful strategy for identifying novel autophagy players. Through a peptide competition approach, we identified potential SARs, among which CESAR was validated and characterized as a selective autophagy receptor. Our findings establish CESAR as a key regulator of protein quality control and cellular homeostasis in plants.

Mechanistically, we propose the following model based on our results: under normal conditions, CESAR contributes to cellular homeostasis. Following heat stress and a short recovery period, CESAR is upregulated and associates with ATG8 to mediate the engulfment of heat stress-induced cargo into autophagosomes. During the late recovery phase, CESAR and its associated cargo, sequestered by autophagosomes, are degraded in the vacuole via autophagy. This CESAR-mediated autophagic degradation restores protein homeostasis after heat stress, thereby promoting plant survival, growth, and heat stress resistance (Figure 20).

Furthermore, we propose that the interaction between CESAR and NBR1 facilitates the efficient targeting of misfolded proteins and protein aggregates for autophagic degradation, functioning through a cooperative mechanism (Figure 21).

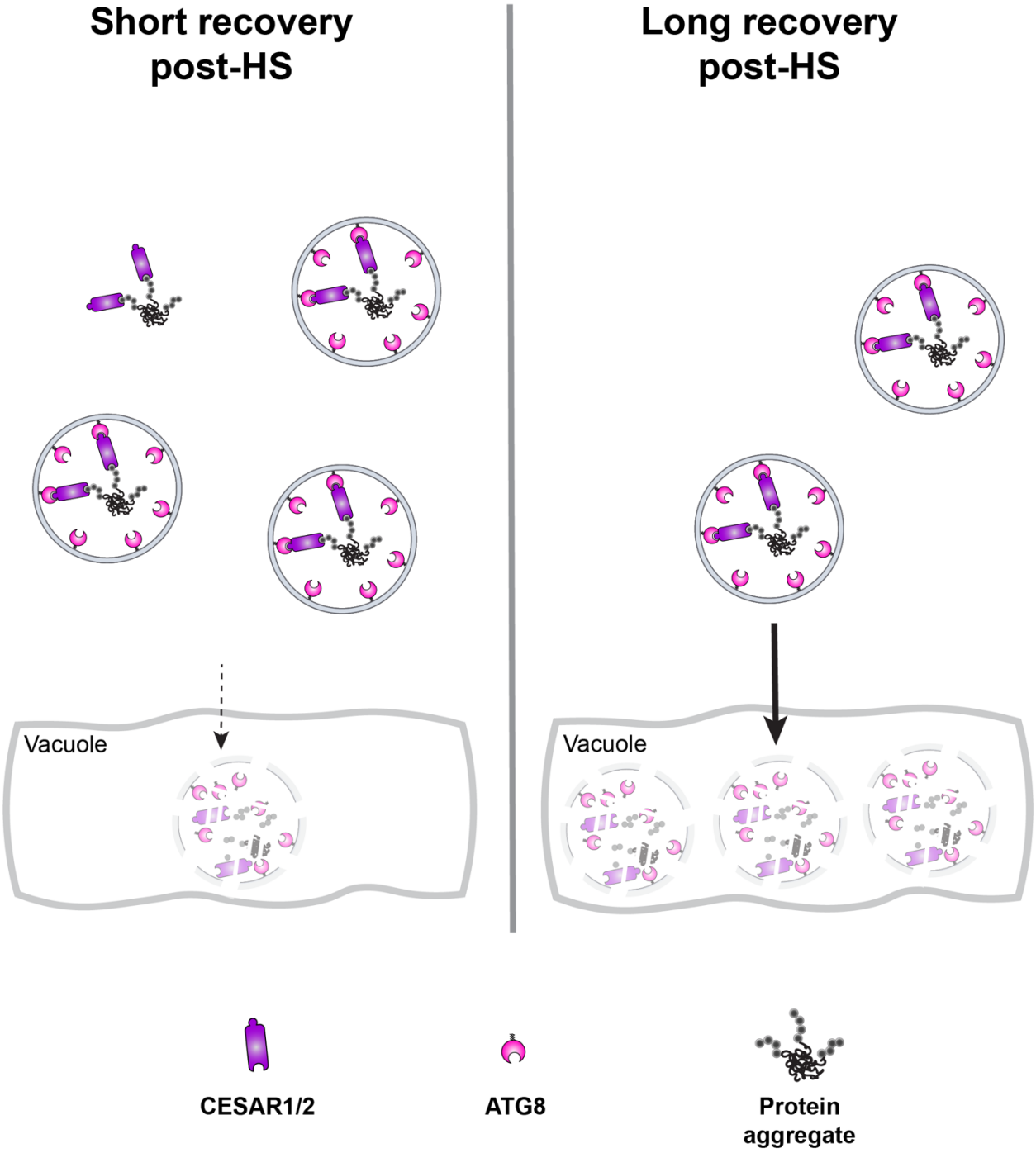

Figure 20. Proposed model of CESAR-mediated autophagy upon heat stressed followed by short and a prolonged recovery post-heat stress (post-HS). CESAR is shown in purple and ATG8 in pink.

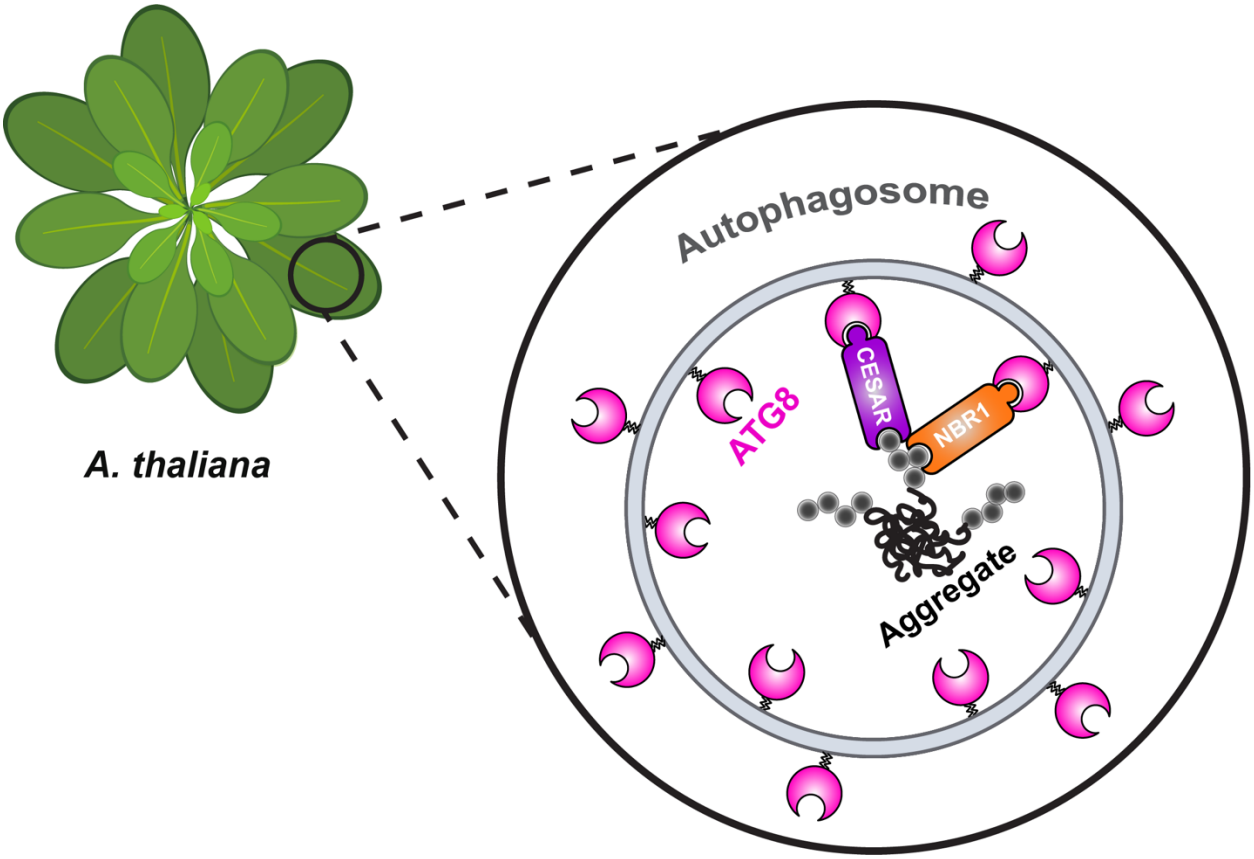

Figure 21. Proposed model of the synergistic function of CESAR and NBR1 in efficient protein aggregate autophagic degradation.

REFERENCES

The results of this thesis, except the CESAR-NBR1 crosstalk part, ended up in the following manuscript:

Sánchez de Medina, V. S. and Nava García, M.M., et al (2024). Cross-species interactome analysis uncovers a conserved selective autophagy mechanism for protein quality control in plants. *bioRxiv*. https://doi.org/10.1101/2024.09.08.611708

Adriaenssens, E., Ferrari, L., Martens, S., 2022. Orchestration of selective autophagy by cargo receptors. Curr. Biol. 32, R1357–R1371. https://doi.org/10.1016/j.cub.2022.11.002

Bauer, B., Idinger, J., Schuschnig, M., Ferrari, L., Martens, S., 2024. Recruitment of autophagy initiator TAX1BP1 advances aggrephagy from cargo collection to sequestration. EMBO J. 43, 5910–5940. https://doi.org/10.1038/s44318-024-00280-5

Bauer, B., Martens, S., Ferrari, L., 2023. Aggrephagy at a glance. J. Cell Sci. 136, jcs260888. https://doi.org/10.1242/jcs.260888

Birgisdottir, Å.B., Lamark, T., Johansen, T., 2013. The LIR motif – crucial for selective autophagy. J. Cell Sci. 126, 3237–3247. https://doi.org/10.1242/jcs.126128

Bodnar, N.O., Rapoport, T.A., 2017. Molecular Mechanism of Substrate Processing by the Cdc48 ATPase Complex. Cell 169, 722-735.e9. https://doi.org/10.1016/j.cell.2017.04.020

Chen, R.-H., Chen, Y.-H., Huang, T.-Y., 2019. Ubiquitin-mediated regulation of autophagy. J. Biomed. Sci. 26, 80. https://doi.org/10.1186/s12929-019-0569-y

Chung, K.K., Zhao, Z., Law, K.C., Ma, J., Chiang, C.H., Leung, K.H., Shrestha, R., Wu, Y., Li, C., Lee, K.M., Feng, L., Li, X., Wong, K.B., Xu, S.-L., Gao, C., Zhuang, X., 2024. Biomolecular condensation of ERC1 recruits ATG8 and NBR1 to drive autophagosome formation for plant heat tolerance. https://doi.org/10.1101/2024.09.09.611939

Ciuffa, R., Lamark, T., Tarafder, A.K., Guesdon, A., Rybina, S., Hagen, W.J.H., Johansen, T., Sachse, C., 2015. The Selective Autophagy Receptor p62 Forms a Flexible Filamentous Helical Scaffold. Cell Rep. 11, 748–758. https://doi.org/10.1016/j.celrep.2015.03.062

Doblmann, J., Dusberger, F., Imre, R., Hudecz, O., Stanek, F., Mechtler, K., Dürnberger, G., 2018. apQuant: Accurate Label-Free Quantification by Quality Filtering. J. Proteome Res. acs.jproteome.8b00113. https://doi.org/10.1021/acs.jproteome.8b00113

Dorfer, V., Pichler, P., Stranzl, T., Stadlmann, J., Taus, T., Winkler, S., Mechtler, K., 2014. MS Amanda, a Universal Identification Algorithm Optimized for High Accuracy

Tandem Mass Spectra. J. Proteome Res. 13, 3679–3684. https://doi.org/10.1021/pr500202e

Dósa, A., Csizmadia, T., 2022. The role of K63-linked polyubiquitin in several types of autophagy. Biol. Futura 73, 137–148. https://doi.org/10.1007/s42977-022-00117-4

Ebstrup, E., Ansbøl, J., Paez-Garcia, A., Culp, H., Chevalier, J., Clemmens, P., Coll, N.S., Moreno-Risueno, M.A., Rodriguez, E., 2024. NBR1-mediated selective autophagy of ARF7 modulates root branching. EMBO Rep. 25, 2571–2591. https://doi.org/10.1038/s44319-024-00142-5

Ellis, J., 1987. Proteins as molecular chaperones. Nature 328, 378–379. https://doi.org/10.1038/328378a0

Emms, D.M., Kelly, S., 2020. Benchmarking Orthogroup Inference Accuracy: Revisiting Orthobench. Genome Biol. Evol. 12, 2258–2266. https://doi.org/10.1093/gbe/evaa211

Feng, Y., He, D., Yao, Z., Klionsky, D.J., 2014. The machinery of macroautophagy. Cell Res. 24, 24–41. https://doi.org/10.1038/cr.2013.168

Gatica, D., Lahiri, V., Klionsky, D.J., 2018a. Cargo recognition and degradation by selective autophagy. Nat. Cell Biol. 20, 233–242. https://doi.org/10.1038/s41556-018-0037-z

Gatica, D., Lahiri, V., Klionsky, D.J., 2018b. Cargo recognition and degradation by selective autophagy. Nat. Cell Biol. 20, 233–242. https://doi.org/10.1038/s41556-018-0037-z

Germain, K., So, R.W.L., DiGiovanni, L.F., Watts, J.C., Bandsma, R.H.J., Kim, P.K., 2024. Upregulated pexophagy limits the capacity of selective autophagy. Nat. Commun. 15, 375. https://doi.org/10.1038/s41467-023-44005-4

Goebel, T., Mausbach, S., Tuermer, A., Eltahir, H., Winter, D., Gieselmann, V., Thelen, M., 2020. Proteaphagy in Mammalian Cells Can Function Independent of ATG5/ATG7. Mol. Cell. Proteomics 19, 1120–1131. https://doi.org/10.1074/mcp.RA120.001983

Gómez-Sánchez, R., Rose, J., Guimarães, R., Mari, M., Papinski, D., Rieter, E., Geerts, W.J., Hardenberg, R., Kraft, C., Ungermann, C., Reggiori, F., 2018. Atg9 establishes Atg2-dependent contact sites between the endoplasmic reticulum and phagophores. J. Cell Biol. 217, 2743–2763. https://doi.org/10.1083/jcb.201710116

Gross, A.S., Raffeiner, M., Zeng, Y., Üstün, S., Dagdas, Y., 2025. Autophagy in Plant Health and Disease. Annu. Rev. Plant Biol. https://doi.org/10.1146/annurev-arplant-060324-094912

Gubas, A., Dikic, I., 2022. A guide to the regulation of selective autophagy receptors. FEBS J. 289, 75–89. https://doi.org/10.1111/febs.15824

Hafrén, A., Macia, J.-L., Love, A.J., Milner, J.J., Drucker, M., Hofius, D., 2017. Selective autophagy limits cauliflower mosaic virus infection by NBR1-mediated targeting of viral capsid protein and particles. Proc. Natl. Acad. Sci. 114. https://doi.org/10.1073/pnas.1610687114

Harper, J.W., Bennett, E.J., 2016. Proteome complexity and the forces that drive proteome imbalance. Nature 537, 328–338. https://doi.org/10.1038/nature19947

Hartl, F.U., Bracher, A., Hayer-Hartl, M., 2011. Molecular chaperones in protein folding and proteostasis. Nature 475, 324–332. https://doi.org/10.1038/nature10317

Hartl, F.U., Hayer-Hartl, M., 2009. Converging concepts of protein folding in vitro and in vivo. Nat. Struct. Mol. Biol. 16, 574–581. https://doi.org/10.1038/nsmb.1591

Hendrick, J.P., Hartl, F.-U., 1993. MOLECULAR CHAPERONE FUNCTIONS OF HEAT-SHOCK PROTEINS. Annu. Rev. Biochem. 62, 349–384. https://doi.org/10.1146/annurev.bi.62.070193.002025

Henne, W.M., 2021. Organelle homeostasis principles: How organelle quality control and inter-organelle crosstalk promote cell survival. Dev. Cell 56, 878–880. https://doi.org/10.1016/j.devcel.2021.03.012

Hinkson, I.V., Elias, J.E., 2011. The dynamic state of protein turnover: It's about time. Trends Cell Biol. 21, 293–303. https://doi.org/10.1016/j.tcb.2011.02.002

Hipp, M.S., Kasturi, P., Hartl, F.U., 2019. The proteostasis network and its decline in ageing. Nat. Rev. Mol. Cell Biol. 20, 421–435. https://doi.org/10.1038/s41580-019-0101-y

Hjerpe, R., Aillet, F., Lopitz-Otsoa, F., Lang, V., England, P., Rodriguez, M.S., 2009. Efficient protection and isolation of ubiquitylated proteins using tandem ubiquitin-binding entities. EMBO Rep. 10, 1250–1258. https://doi.org/10.1038/embor.2009.192

Hurley, J.H., Young, L.N., 2017. Mechanisms of Autophagy Initiation. Annu. Rev. Biochem. 86, 225–244. https://doi.org/10.1146/annurev-biochem-061516-044820

Hyun, D., Lee, M., Halliwell, B., Jenner, P., 2003. Proteasomal inhibition causes the formation of protein aggregates containing a wide range of proteins, including nitrated proteins. J. Neurochem. 86, 363–373. https://doi.org/10.1046/j.1471-4159.2003.01841.x

Ikeda, F., Dikic, I., 2008. Atypical ubiquitin chains: new molecular signals. EMBO Rep. 9, 536–542. https://doi.org/10.1038/embor.2008.93

Iwata, A., Riley, B.E., Johnston, J.A., Kopito, R.R., 2005. HDAC6 and Microtubules Are Required for Autophagic Degradation of Aggregated Huntingtin. J. Biol. Chem. 280, 40282–40292. https://doi.org/10.1074/jbc.M508786200

Janse Van Rensburg, H.C., Van Den Ende, W., Signorelli, S., 2019. Autophagy in Plants: Both a Puppet and a Puppet Master of Sugars. Front. Plant Sci. 10, 14. https://doi.org/10.3389/fpls.2019.00014

Jayaraj, G.G., Hipp, M.S., Hartl, F.U., 2020. Functional Modules of the Proteostasis Network. Cold Spring Harb. Perspect. Biol. 12, a033951. https://doi.org/10.1101/cshperspect.a033951

Ji, C.H., Kwon, Y.T., 2017. Crosstalk and Interplay between the Ubiquitin-Proteasome System and Autophagy. Mol. Cells 40, 441–449. https://doi.org/10.14348/molcells.2017.0115

Jung, H., Lee, H.N., Marshall, R.S., Lomax, A.W., Yoon, M.J., Kim, J., Kim, J.H., Vierstra, R.D., Chung, T., 2020a. Arabidopsis cargo receptor NBR1 mediates selective autophagy of defective proteins. J. Exp. Bot. 71, 73–89. https://doi.org/10.1093/jxb/erz404

Jung, H., Lee, H.N., Marshall, R.S., Lomax, A.W., Yoon, M.J., Kim, J., Kim, J.H., Vierstra, R.D., Chung, T., 2020b. Arabidopsis cargo receptor NBR1 mediates selective autophagy of defective proteins. J. Exp. Bot. 71, 73–89. https://doi.org/10.1093/jxb/erz404

Käll, L., Canterbury, J.D., Weston, J., Noble, W.S., MacCoss, M.J., 2007. Semi-supervised learning for peptide identification from shotgun proteomics datasets. Nat. Methods 4, 923–925. https://doi.org/10.1038/nmeth1113

Kan, Y., Mu, X.-R., Gao, J., Lin, H.-X., Lin, Y., 2023. The molecular basis of heat stress responses in plants. Mol. Plant 16, 1612–1634. https://doi.org/10.1016/j.molp.2023.09.013

Kandel, R., Jung, J., Neal, S., 2024. Proteotoxic stress and the ubiquitin proteasome system. Semin. Cell Dev. Biol. 156, 107–120. https://doi.org/10.1016/j.semcdb.2023.08.002

Kang, B.-H., 2010. Electron Microscopy and High-Pressure Freezing of Arabidopsis, in: Methods in Cell Biology. Elsevier, pp. 259–283. https://doi.org/10.1016/S0091-679X(10)96012-3

Kanki, T., Wang, K., Cao, Y., Baba, M., Klionsky, D.J., 2009. Atg32 Is a Mitochondrial Protein that Confers Selectivity during Mitophagy. Dev. Cell 17, 98–109. https://doi.org/10.1016/j.devcel.2009.06.014

Kim, Y.E., Hipp, M.S., Bracher, A., Hayer-Hartl, M., Ulrich Hartl, F., 2013. Molecular Chaperone Functions in Protein Folding and Proteostasis. Annu. Rev. Biochem. 82, 323–355. https://doi.org/10.1146/annurev-biochem-060208-092442

Kirkin, V., Lamark, T., Sou, Y.S., Bjørkøy, G., Nunn, J.L., Bruun, J.A., Shvets, E., McEwan, D.G., Clausen, T.H., Wild, P., Bilusic, I., Theurillat, J.P., Øvervatn, A., Ishii, T., Elazar, Z., Komatsu, M., Dikic, I., Johansen, T., 2009. A Role for NBR1 in Autophagosomal Degradation of Ubiquitinated Substrates. Mol. Cell 33, 505–516. https://doi.org/10.1016/j.molcel.2009.01.020

Korolchuk, V.I., Mansilla, A., Menzies, F.M., Rubinsztein, D.C., 2009. Autophagy Inhibition Compromises Degradation of Ubiquitin-Proteasome Pathway Substrates. Mol. Cell 33, 517–527. https://doi.org/10.1016/j.molcel.2009.01.021

Kourelis, J., Kaschani, F., Grosse-Holz, F.M., Homma, F., Kaiser, M., Van Der Hoorn, R.A.L., 2019. A homology-guided, genome-based proteome for improved proteomics in the alloploid Nicotiana benthamiana. BMC Genomics 20, 722. https://doi.org/10.1186/s12864-019-6058-6

Kuhn, L., Vincent, T., Hammann, P., Zuber, H., 2023. Exploring Protein Interactome Data with IPinquiry: Statistical Analysis and Data Visualization by Spectral Counts, in: Burger, T. (Ed.), Statistical Analysis of Proteomic Data, Methods in Molecular

Biology. Springer US, New York, NY, pp. 243–265. https://doi.org/10.1007/978-1-0716-1967-4_11

Lamark, T., Johansen, T., 2021. Mechanisms of Selective Autophagy.

Lamark, T., Johansen, T., 2012. Aggrephagy: Selective Disposal of Protein Aggregates by Macroautophagy. Int. J. Cell Biol. 2012, 1–21. https://doi.org/10.1155/2012/736905

Lamark, T., Perander, M., Outzen, H., Kristiansen, K., Øvervatn, A., Michaelsen, E., Bjørkøy, G., Johansen, T., 2003. Interaction Codes within the Family of Mammalian Phox and Bem1p Domain-containing Proteins. J. Biol. Chem. 278, 34568–34581. https://doi.org/10.1074/jbc.M303221200

Lee, C.-W., Wilfling, F., Ronchi, P., Allegretti, M., Mosalaganti, S., Jentsch, S., Beck, M., Pfander, B., 2020. Selective autophagy degrades nuclear pore complexes. Nat. Cell Biol. 22, 159–166. https://doi.org/10.1038/s41556-019-0459-2

Lee, H.N., Chacko, J.V., Gonzalez Solís, A., Chen, K.-E., Barros, J.A., Signorelli, S., Millar, A.H., Vierstra, R.D., Eliceiri, K.W., Otegui, M.S., 2023. The autophagy receptor NBR1 directs the clearance of photodamaged chloroplasts. eLife 12, e86030. https://doi.org/10.7554/eLife.86030

Li, J., Yuan, J., Li, Y., Sun, H., Ma, T., Huai, J., Yang, W., Zhang, W., Lin, R., 2022. The CDC48 complex mediates ubiquitin-dependent degradation of intra-chloroplast proteins in plants. Cell Rep. 39, 110664. https://doi.org/10.1016/j.celrep.2022.110664

Li, W., He, P., Huang, Y., Li, Y.-F., Lu, J., Li, M., Kurihara, H., Luo, Z., Meng, T., Onishi, M., Ma, C., Jiang, L., Hu, Y., Gong, Q., Zhu, D., Xu, Y., Liu, R., Liu, L., Yi, C., Zhu, Y., Ma, N., Okamoto, K., Xie, Z., Liu, J., He, R.-R., Feng, D., 2021. Selective autophagy of intracellular organelles: Recent research advances. Theranostics 11, 222–256. https://doi.org/10.7150/thno.49860

Li, X., Liao, J., Chung, K.K., Feng, L., Liao, Y., Yang, Z., Liu, C., Zhou, J., Shen, W., Li, H., Yang, C., Zhuang, X., Gao, C., 2024. Stress granules sequester autophagy proteins to facilitate plant recovery from heat stress. Nat. Commun. 15, 10910. https://doi.org/10.1038/s41467-024-55292-w

Lois, L.M., Trujillo, M. (Eds.), 2023. Plant Proteostasis: Methods and Protocols, Methods in Molecular Biology. Springer US, New York, NY. https://doi.org/10.1007/978-1-0716-2784-6

Long, J., Garner, T.P., Pandya, M.J., Craven, C.J., Chen, P., Shaw, B., Williamson, M.P., Layfield, R., Searle, M.S., 2010. Dimerisation of the UBA Domain of p62 Inhibits Ubiquitin Binding and Regulates NF-κB Signalling. J. Mol. Biol. 396, 178–194. https://doi.org/10.1016/j.jmb.2009.11.032

Lu, K., Psakhye, I., Jentsch, S., 2014. Autophagic Clearance of PolyQ Proteins Mediated by Ubiquitin-Atg8 Adaptors of the Conserved CUET Protein Family. Cell 158, 549–563. https://doi.org/10.1016/j.cell.2014.05.048

Ma, X., Lu, C., Chen, Y., Li, S., Ma, N., Tao, X., Li, Y., Wang, J., Zhou, M., Yan, Y.-B., Li, P., Heydari, K., Deng, H., Zhang, M., Yi, C., Ge, L., 2022. CCT2 is an aggrephagy receptor for clearance of solid protein aggregates. Cell 185, 1325-1345.e22. https://doi.org/10.1016/j.cell.2022.03.005

Mancias, J.D., Wang, X., Gygi, S.P., Harper, J.W., Kimmelman, A.C., 2014. Quantitative proteomics identifies NCOA4 as the cargo receptor mediating ferritinophagy. Nature 509, 105–109. https://doi.org/10.1038/nature13148

Mao, K., Klionsky, D.J., 2017. Xenophagy: A battlefield between host and microbe, and a possible avenue for cancer treatment. Autophagy 13, 223–224. https://doi.org/10.1080/15548627.2016.1267075

Marshall, R.S., Li, F., Gemperline, D.C., Book, A.J., Vierstra, R.D., 2015. Autophagic Degradation of the 26S Proteasome Is Mediated by the Dual ATG8/Ubiquitin Receptor RPN10 in Arabidopsis. Mol. Cell 58, 1053–1066. https://doi.org/10.1016/j.molcel.2015.04.023

Marshall, R.S., Vierstra, R.D., 2019. Dynamic Regulation of the 26S Proteasome: From Synthesis to Degradation. Front. Mol. Biosci. 6, 40. https://doi.org/10.3389/fmolb.2019.00040

Mizushima, N., Komatsu, M., 2011. Autophagy: Renovation of Cells and Tissues. Cell 147, 728–741. https://doi.org/10.1016/j.cell.2011.10.026

Nakatogawa, H., 2020. Mechanisms governing autophagosome biogenesis. Nat. Rev. Mol. Cell Biol. 21, 439–458. https://doi.org/10.1038/s41580-020-0241-0

Nawaz, M., Sun, J., Shabbir, S., Khattak, W.A., Ren, G., Nie, X., Bo, Y., Javed, Q., Du, D., Sonne, C., 2023. A review of plants strategies to resist biotic and abiotic environmental stressors. Sci. Total Environ. 900, 165832. https://doi.org/10.1016/j.scitotenv.2023.165832

Nillegoda, N.B., Bukau, B., 2015. Metazoan Hsp70-based protein disaggregases: emergence and mechanisms. Front. Mol. Biosci. 2. https://doi.org/10.3389/fmolb.2015.00057

Nishimura, T., Tooze, S.A., 2020. Emerging roles of ATG proteins and membrane lipids in autophagosome formation. Cell Discov. 6, 32. https://doi.org/10.1038/s41421-020-0161-3

Noda, N.N., Ohsumi, Y., Inagaki, F., 2010. Atg8-family interacting motif crucial for selective autophagy. FEBS Lett. 584, 1379–1385. https://doi.org/10.1016/j.febslet.2010.01.018

Ohnstad, A.E., Delgado, J.M., North, B.J., Nasa, I., Kettenbach, A.N., Schultz, S.W., Shoemaker, C.J., 2020. Receptor-mediated clustering of FIP200 bypasses the role of LC3 lipidation in autophagy. EMBO J. 39, e104948. https://doi.org/10.15252/embj.2020104948

Ohsumi, Y., 2014. Historical landmarks of autophagy research. Cell Res. 24, 9–23. https://doi.org/10.1038/cr.2013.169

Pandey, U.B., Nie, Z., Batlevi, Y., McCray, B.A., Ritson, G.P., Nedelsky, N.B., Schwartz, S.L., DiProspero, N.A., Knight, M.A., Schuldiner, O., Padmanabhan, R., Hild, M., Berry, D.L., Garza, D., Hubbert, C.C., Yao, T.-P., Baehrecke, E.H., Taylor, J.P., 2007. HDAC6 rescues neurodegeneration and provides an essential link between autophagy and the UPS. Nature 447, 860–864. https://doi.org/10.1038/nature05853

Pilla, E., Schneider, K., Bertolotti, A., 2017. Coping with Protein Quality Control Failure. Annu. Rev. Cell Dev. Biol. 33, 439–465. https://doi.org/10.1146/annurev-cellbio-111315-125334

Pohl, C., Dikic, I., 2019. Cellular quality control by the ubiquitin-proteasome system and autophagy. Science 366, 818–822. https://doi.org/10.1126/science.aax3769

Popov, N., Schmitt, M., Schulzeck, S., Matthies, H., 1975. [Reliable micromethod for determination of the protein content in tissue homogenates]. Acta Biol. Med. Ger. 34, 1441–1446.

Raffeiner, M., Zhu, S., González-Fuente, M., Üstün, S., 2023. Interplay between autophagy and proteasome during protein turnover. Trends Plant Sci. 28, 698–714. https://doi.org/10.1016/j.tplants.2023.01.013

Richter, K., Haslbeck, M., Buchner, J., 2010. The Heat Shock Response: Life on the Verge of Death. Mol. Cell 40, 253–266. https://doi.org/10.1016/j.molcel.2010.10.006

Rolfs, Z., Frey, B.L., Shi, X., Kawai, Y., Smith, L.M., Welham, N.V., 2021. An atlas of protein turnover rates in mouse tissues. Nat. Commun. 12, 6778. https://doi.org/10.1038/s41467-021-26842-3

Ross, A.B., Langer, J.D., Jovanovic, M., 2021. Proteome Turnover in the Spotlight: Approaches, Applications, and Perspectives. Mol. Cell. Proteomics 20, 100016. https://doi.org/10.1074/mcp.R120.002190

Sarraf, S.A., Shah, H.V., Kanfer, G., Pickrell, A.M., Holtzclaw, L.A., Ward, M.E., Youle, R.J., 2020. Loss of TAX1BP1-Directed Autophagy Results in Protein Aggregate Accumulation in the Brain. Mol. Cell 80, 779-795.e10. https://doi.org/10.1016/j.molcel.2020.10.041

Sawa-Makarska, J., Baumann, V., Coudevylle, N., Von Bülow, S., Nogellova, V., Abert, C., Schuschnig, M., Graef, M., Hummer, G., Martens, S., 2020. Reconstitution of autophagosome nucleation defines Atg9 vesicles as seeds for membrane formation. Science 369, eaaz7714. https://doi.org/10.1126/science.aaz7714

Schreiber, A., Peter, M., 2014. Substrate recognition in selective autophagy and the ubiquitin–proteasome system. Biochim. Biophys. Acta BBA - Mol. Cell Res. 1843, 163–181. https://doi.org/10.1016/j.bbamcr.2013.03.019

Schwanhäusser, B., Busse, D., Li, N., Dittmar, G., Schuchhardt, J., Wolf, J., Chen, W., Selbach, M., 2011. Global quantification of mammalian gene expression control. Nature 473, 337–342. https://doi.org/10.1038/nature10098

Smyth, G.K., 2004. Linear Models and Empirical Bayes Methods for Assessing Differential Expression in Microarray Experiments. Stat. Appl. Genet. Mol. Biol. 3, 1–25. https://doi.org/10.2202/1544-6115.1027

Song, L., Luo, Z.-Q., 2019. Post-translational regulation of ubiquitin signaling. J. Cell Biol. 218, 1776–1786. https://doi.org/10.1083/jcb.201902074

Sontag, E.M., Vonk, W.I., Frydman, J., 2014. Sorting out the trash: the spatial nature of eukaryotic protein quality control. Curr. Opin. Cell Biol. 26, 139–146. https://doi.org/10.1016/j.ceb.2013.12.006

Stephani, M., Picchianti, L., Gajic, A., Beveridge, R., Skarwan, E., Hernandez, V.S. de M., Mohseni, A., Clavel, M., Zeng, Y., Naumann, C., Matuszkiewicz, M., Turco, E., Loefke, C., Li, B., Durnberger, G., Schutzbier, M., Chen, H.T., Abdrakhmanov, A., Savova, A., Chia, K.S., Djamei, A., Schaffner, I., Abel, S., Jiang, L., Mechtler, K., Ikeda, F., Martens, S., Clausen, T., Dagdas, Y., 2020. A cross-kingdom conserved er-phagy receptor maintains endoplasmic reticulum homeostasis during stress. eLife 9, 1–105. https://doi.org/10.7554/ELIFE.58396

Su, T., Li, X., Yang, M., Shao, Q., Zhao, Y., Ma, C., Wang, P., 2020. Autophagy: An Intracellular Degradation Pathway Regulating Plant Survival and Stress Response. Front. Plant Sci. https://doi.org/10.3389/fpls.2020.00164

Svenning, S., Lamark, T., Krause, K., Johansen, T., 2011. Plant NBR1 is a selective autophagy substrate and a functional hybrid of the mammalian autophagic adapters NBR1 and p62/SQSTM1. Autophagy 7, 993–1010. https://doi.org/10.4161/auto.7.9.16389

Taus, T., Köcher, T., Pichler, P., Paschke, C., Schmidt, A., Henrich, C., Mechtler, K., 2011. Universal and Confident Phosphorylation Site Localization Using phosphoRS. J. Proteome Res. 10, 5354–5362. https://doi.org/10.1021/pr200611n

Thirumalaikumar, V.P., Gorka, M., Schulz, K., Masclaux-Daubresse, C., Sampathkumar, A., Skirycz, A., Vierstra, R.D., Balazadeh, S., 2021. Selective autophagy regulates heat stress memory in Arabidopsis by NBR1-mediated targeting of HSP90.1 and ROF1. Autophagy 17, 2184–2199. https://doi.org/10.1080/15548627.2020.1820778

Thompson, A.R., Doelling, J.H., Suttangkakul, A., Vierstra, R.D., 2005. Autophagic Nutrient Recycling in Arabidopsis Directed by the ATG8 and ATG12 Conjugation Pathways. Plant Physiol. 138, 2097–2110. https://doi.org/10.1104/pp.105.060673

Thrower, J.S., 2000. Recognition of the polyubiquitin proteolytic signal. EMBO J. 19, 94–102. https://doi.org/10.1093/emboj/19.1.94

Tomioka, Y., Kotani, T., Kirisako, H., Oikawa, Y., Kimura, Y., Hirano, H., Ohsumi, Y., Nakatogawa, H., 2020. TORC1 inactivation stimulates autophagy of nucleoporin and nuclear pore complexes. J. Cell Biol. 219, e201910063. https://doi.org/10.1083/jcb.201910063

Turco, E., Savova, A., Gere, F., Ferrari, L., Romanov, J., Schuschnig, M., Martens, S., 2021. Reconstitution defines the roles of p62, NBR1 and TAX1BP1 in ubiquitin condensate formation and autophagy initiation. Nat. Commun. 12, 1–16. https://doi.org/10.1038/s41467-021-25572-w

Vabulas, R.M., Raychaudhuri, S., Hayer-Hartl, M., Hartl, F.U., 2010. Protein Folding in the Cytoplasm and the Heat Shock Response. Cold Spring Harb. Perspect. Biol. 2, a004390–a004390. https://doi.org/10.1101/cshperspect.a004390

Vainshtein, A., Grumati, P., 2020. Selective Autophagy by Close Encounters of the Ubiquitin Kind. Cells 9, 2349. https://doi.org/10.3390/cells9112349

Vargas, J.N.S., Hamasaki, M., Kawabata, T., Youle, R.J., Yoshimori, T., 2023. The mechanisms and roles of selective autophagy in mammals. Nat. Rev. Mol. Cell Biol. 24, 167–185. https://doi.org/10.1038/s41580-022-00542-2

Vega-Lugo, J., Da Rocha-Azevedo, B., Dasgupta, A., Jaqaman, K., 2022. Analysis of conditional colocalization relationships and hierarchies in three-color microscopy images. J. Cell Biol. 221, e202106129. https://doi.org/10.1083/jcb.202106129

Walinda, E., Morimoto, D., Sugase, K., Konuma, T., Tochio, H., Shirakawa, M., 2014. Solution Structure of the Ubiquitin-associated (UBA) Domain of Human Autophagy Receptor NBR1 and Its Interaction with Ubiquitin and Polyubiquitin. J. Biol. Chem. 289, 13890–13902. https://doi.org/10.1074/jbc.M114.555441

Wang, D., Xu, Q., Yuan, Q., Jia, M., Niu, H., Liu, X., Zhang, J., Young, C.Y., Yuan, H., 2019. Proteasome inhibition boosts autophagic degradation of ubiquitinated-AGR2 and enhances the antitumor efficiency of bevacizumab. Oncogene 38, 3458–3474. https://doi.org/10.1038/s41388-019-0675-z

Wang, P., Chen, X., Goldbeck, C., Chung, E., Kang, B., 2017. A distinct class of vesicles derived from the *trans* -Golgi mediates secretion of xylogalacturonan in the root border cell. Plant J. 92, 596–610. https://doi.org/10.1111/tpj.13704

Weids, A.J., Ibstedt, S., Tamás, M.J., Grant, C.M., 2016. Distinct stress conditions result in aggregation of proteins with similar properties. Sci. Rep.

Zhang, H., Ling, Q., 2024. NBR1-mediated selective chloroplast autophagy is important to plant stress tolerance. Autophagy 20, 205–206. https://doi.org/10.1080/15548627.2023.2251324

Zhao, J., Bui, M.T., Ma, J., Künzl, F., Picchianti, L., De La Concepcion, J.C., Chen, Y., Petsangouraki, S., Mohseni, A., García-Leon, M., Gomez, M.S., Giannini, C., Gwennogan, D., Kobylinska, R., Clavel, M., Schellmann, S., Jaillais, Y., Friml, J., Kang, B.-H., Dagdas, Y., 2022. Plant autophagosomes mature into amphisomes prior to their delivery to the central vacuole. J. Cell Biol. 221, e202203139. https://doi.org/10.1083/jcb.202203139

Zhao, J., Lu, Z., Wang, L., Jin, B., 2020. Plant Responses to Heat Stress: Physiology, Transcription, Noncoding RNAs, and Epigenetics. Int. J. Mol. Sci. 22, 117. https://doi.org/10.3390/ijms22010117

Zhou, J., Wang, J., Cheng, Y., Chi, Y.-J., Fan, B., Yu, J.-Q., Chen, Z., 2013. NBR1-Mediated Selective Autophagy Targets Insoluble Ubiquitinated Protein Aggregates in Plant Stress Responses. PLoS Genet. 9, e1003196. https://doi.org/10.1371/journal.pgen.1003196

SUPPLEMENTARY FIGURES

Fig.S1

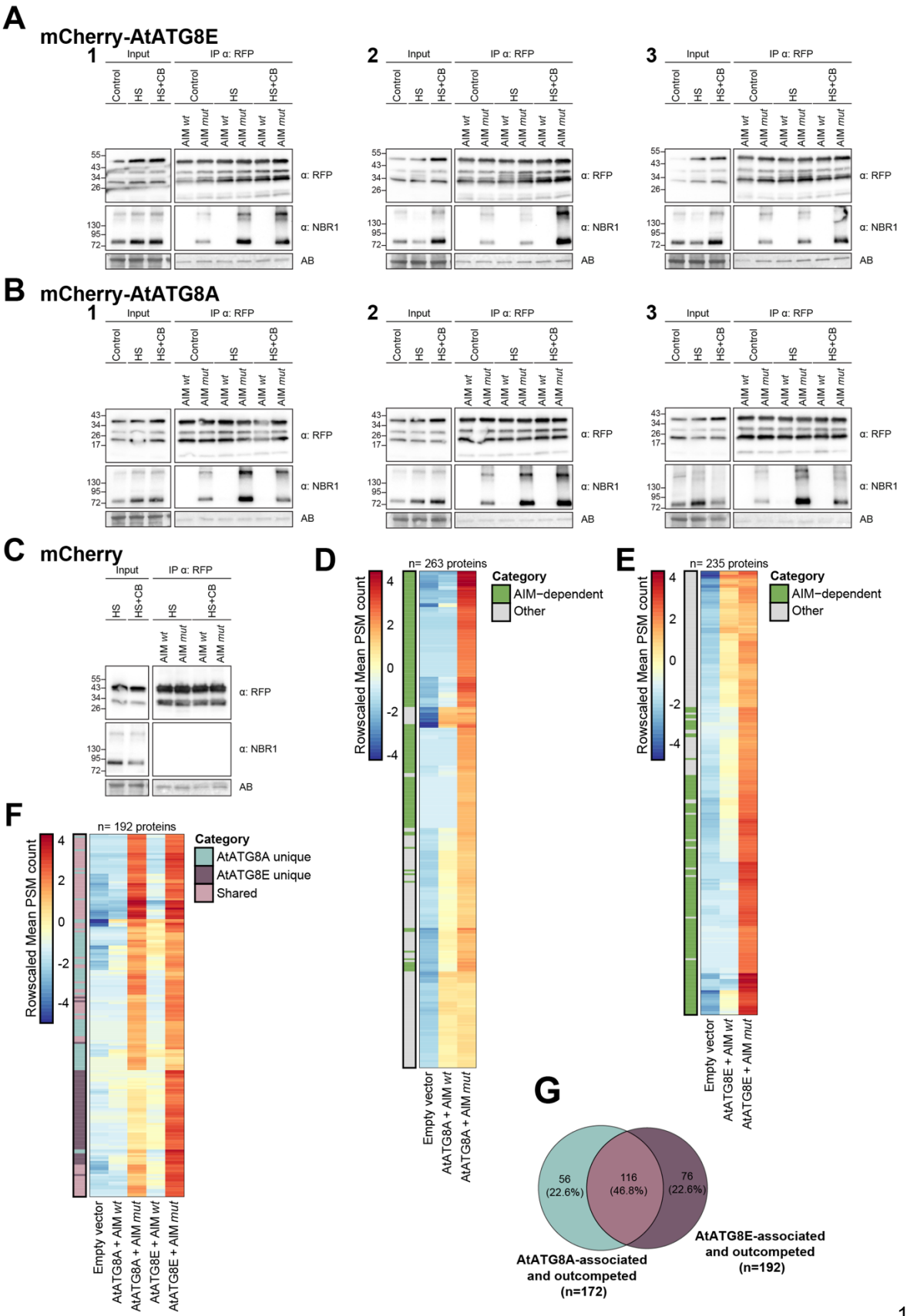
A
mCherry-AtATG8E
1
2
3
Input
IP α: RFP
Control
HS
HS+CB
AIM wt
AIM mut
55
43
34
26
130
95
72
α: RFP
α: NBR1
AB
B
mCherry-AtATG8A
17
C
mCherry
D
n= 263 proteins
Rowscaled Mean PSM count
4
2
0
-2
-4
Category
AIM−dependent
Other
Empty vector
AtATG8A + AIM wt
AtATG8A + AIM mut
E
n= 235 proteins
AtATG8E + AIM wt
AtATG8E + AIM mut
F
n= 192 proteins
AtATG8A unique
AtATG8E unique
Shared
AtATG8E + AIM wt
AtATG8E + AIM mut
G
56
(22.6%)
116
(46.8%)
76
(22.6%)
AtATG8A-associated
and outcompeted
(n=172)
AtATG8E-associated
and outcompeted
(n=192)

Figure S1. AtATG8 interactome analysis using peptide competition and AP-MS. (A-C) Immunoprecipitation of AtATG8 under heat stress (HS) and HS combined with CB5083 (HS+CB) treatment. Seven-day-old *Arabidopsis thaliana* seedlings expressing mCherry-AtATG8E (A), mCherry-AtATG8A (B), or mCherry-EV (C) were subjected to 21°C (control) or 37°C (HS) for 6 hours, followed by a 4-hour recovery at 21°C in fresh ½ MS + MES + 1% sucrose media with either DMSO or 50 µM CB5083 (HS+CB). AIM wild-type (wt) and mutant (mut) peptides were added to a final concentration of 100 µM. Protein extracts were analyzed via immunoblotting with anti-RFP and anti-NBR1 antibodies. Protein size markers (kDa) are shown on the left of the blots. Total protein loading was assessed using Amidoblack (AB) staining. (D) Peptide competition enriches direct interactors of AtATG8A. A heatmap displays protein abundance patterns (Log2 (Mean PSM+1) – Mean PSM per protein) for 263 proteins associated with AtATG8A. Proteins retained in the AIM mut vs. AIM wt comparison are annotated as AIM-dependent. Each column represents the row-scaled mean PSM count from three independent biological replicates. (E) Peptide competition enriches direct interactors of AtATG8E. A heatmap shows protein abundance patterns (Log2 (Mean PSM+1) – Mean PSM per protein) for 235 proteins associated with AtATG8E. Proteins retained in the AIM mut vs. AIM wt comparison are annotated as AIM-dependent. Each column represents the row-scaled mean PSM count from three independent biological replicates. (F) Comparison of AIM-dependent interactors between AtATG8A and AtATG8E. A heatmap illustrates protein abundance patterns (Log2 (Mean PSM+1) – Mean PSM per protein) for 192 outcompeted proteins identified as AIM-dependent for either or both AtATG8 isoforms. Proteins are categorized based on their enrichment in one isoform (AtATG8A/E unique) or multiple isoforms (shared). Each column represents the row-scaled mean PSM count from three independent biological replicates. (G) **Comparison of AtATG8A and AtATG8E interactomes.** A Venn diagram illustrates the overlap between two pairwise comparisons. Proteins associated with and outcompeted by AtATG8A (yellow circle) are defined as AIM-dependent in Fig. S1D, while those associated with and outcompeted by AtATG8E (pink circle) are defined as AIM-dependent in Fig. S1E.

Fig.S2

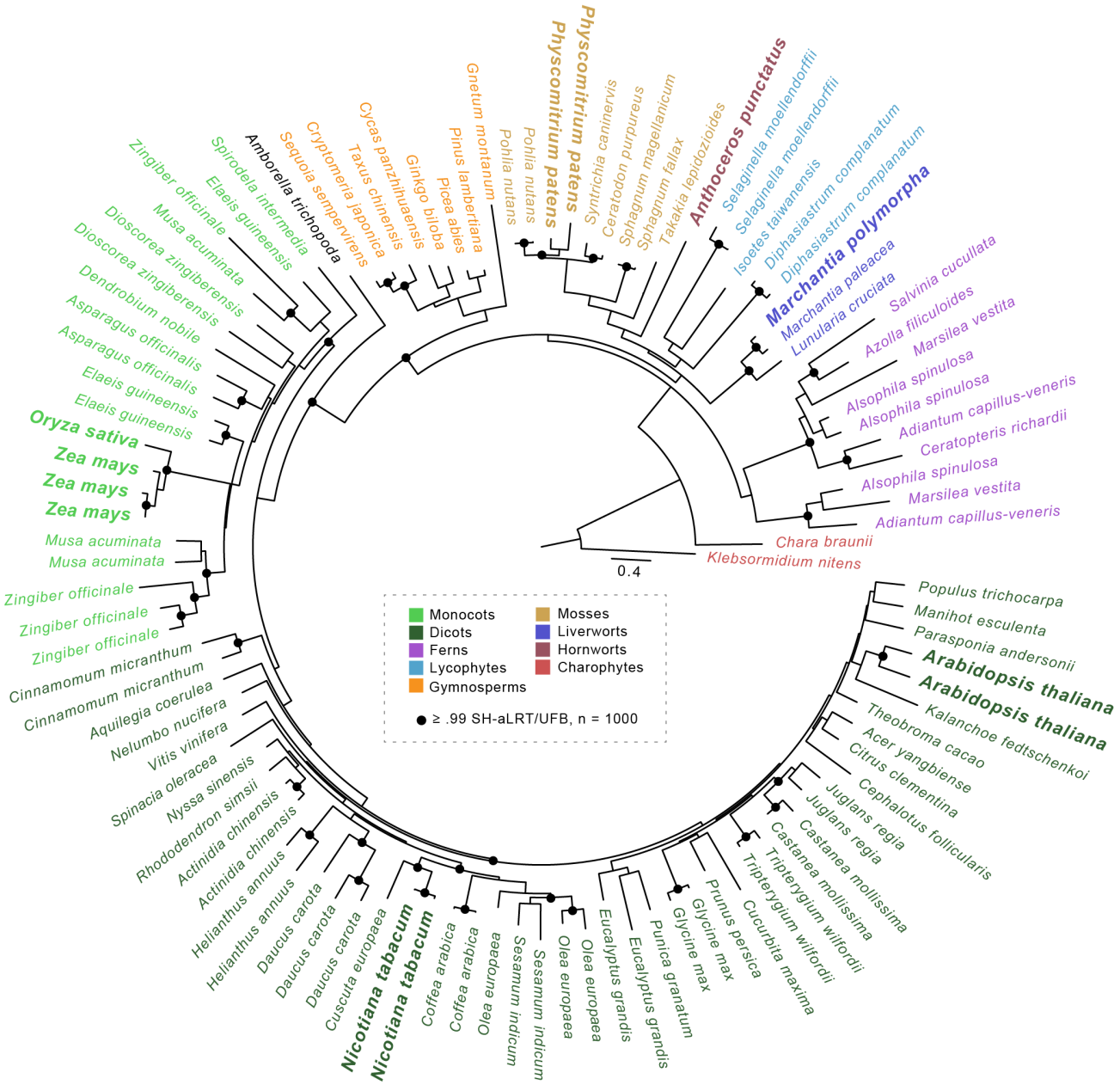

Figure S2. Evolution of CESAR in Streptophyta. A maximum likelihood phylogenetic tree was constructed for 107 non-redundant CESAR homologs from 72 plant and algal species using the LG4M+F+R6 substitution model in IQ-TREE. Charophytes were used to root the tree. Branches are color-coded to represent sequences from specific clades or families, with *Amborella trichopoda* shown in black. CESAR orthologs from species used in the biochemical assays in Figures 2 and S7 are highlighted in bold. Branches with Shimodaira-Hasegawa approximate likelihood-ratio test (SH-aLRT) and ultrafast bootstrap support (UFB) values greater than 99% (n = 1,000) are marked with black circles.

Fig.S3

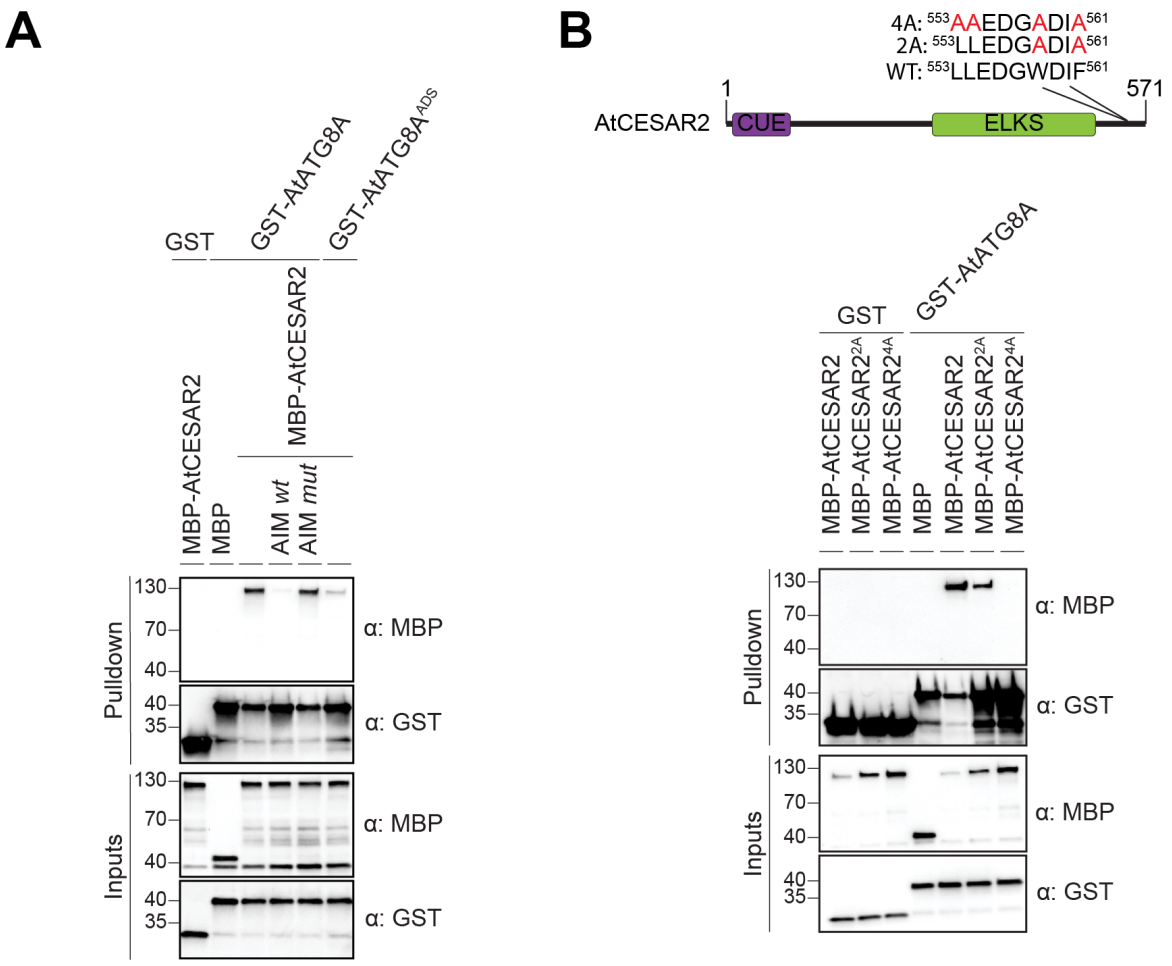

Figure S3. (A-B) AtCESAR2 interacts with ATG8 in an AIM-dependent manner in vitro. AtATG8AADS refers to AtATG8A(Y50A, L51A). AIM wild-type (wt) and mutant (mut) peptides were added at a final concentration of 200 μM. AtCESAR2 contains an AIM motif in its C-terminal region. The protein domain structure of AtCESAR2 is shown, with the CUE and ELKS domains highlighted in purple and green, respectively. The positions of AIM residues, along with their mutagenesis, are indicated. Mutating the AIM motif in AtCESAR2 disrupts its interaction with AtATG8A. AtCESAR22A corresponds to AtCESAR2(W558A, F561A), while AtCESAR24A corresponds to AtCESAR2(L553A, L554A, W558A, F561A). Recombinant proteins from bacterial lysates were mixed and pulled down using glutathione magnetic agarose beads. Input and bound proteins were detected via immunoblotting with anti-GST and anti-MBP antibodies.

Fig.S5

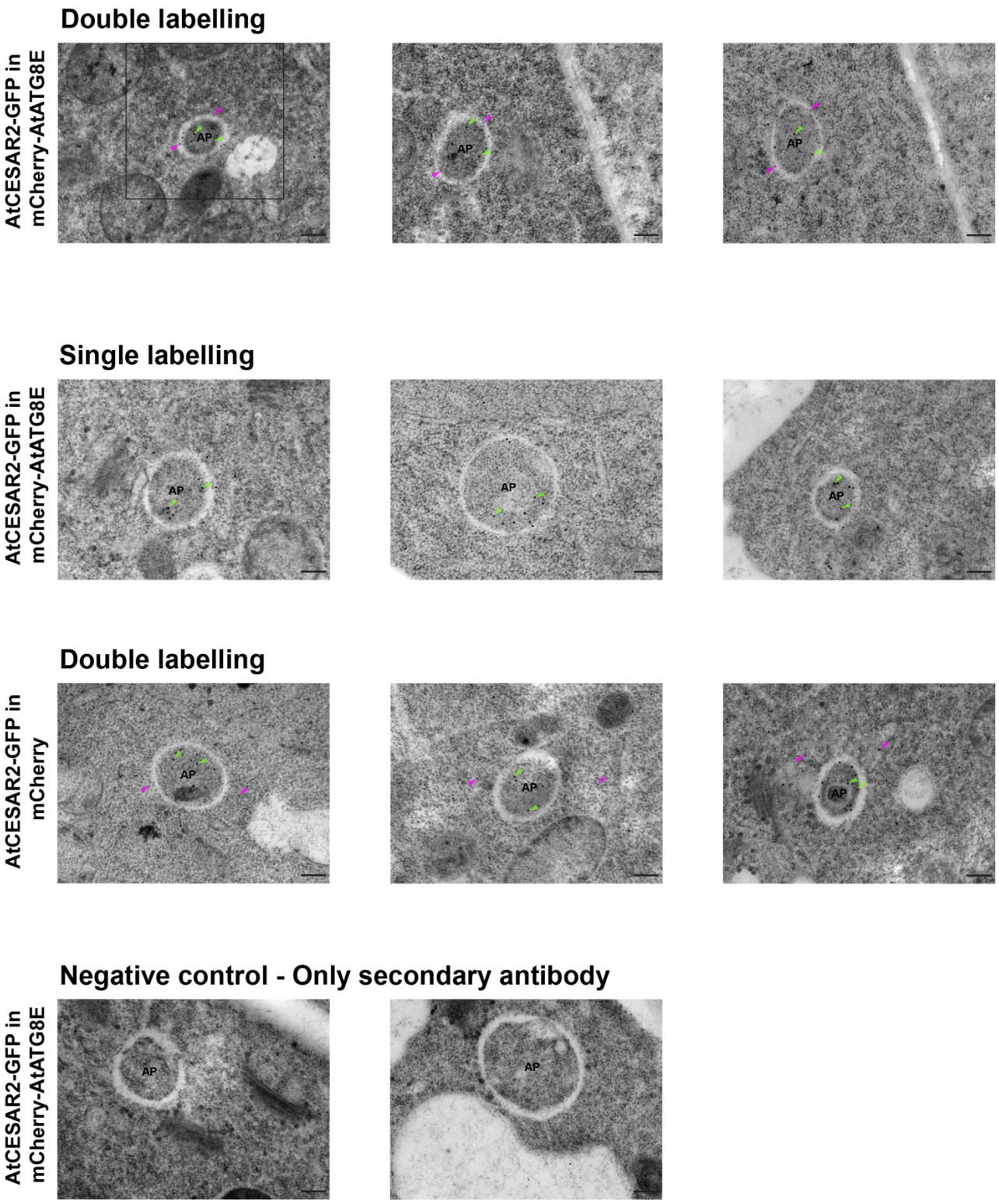
Double labelling
AtCESAR2-GFP in mCherry-AtATG8E
AP
Single labelling
AtCESAR2-GFP in mCherry-AtATG8E
AP
Double labelling
AtCESAR2-GFP in mCherry
AP
Negative control - Only secondary antibody
AtCESAR2-GFP in mCherry-AtATG8E
AP

Figure S5. Transmission electron microscopy reveals CESAR localization within autophagosomes. (A-D) CESAR is localized to the autophagosome lumen. Transmission electron microscopy (TEM) images show immune-gold labeling of AtCESAR2-GFP (15 nm gold particles, green arrows) and mCherry-AtATG8E or mCherry-EV (10 nm gold particles, magenta arrows) in the cytoplasm of *A. thaliana* root cells. Five-day-old *A. thaliana* seedlings were grown at 21°C on 1% agar ½ MS + MES + 1% sucrose plates before cryofixation. Sections were labeled with anti-GFP and anti-mCherry primary antibodies, followed by secondary antibodies conjugated to 15 nm gold particles (for GFP, green arrows) or 10 nm gold particles (for mCherry, magenta arrows). The area highlighted in the first panel serves as a representative image in the main figure. Scale bars: 200 nm. AP, autophagosome.

Fig.S6

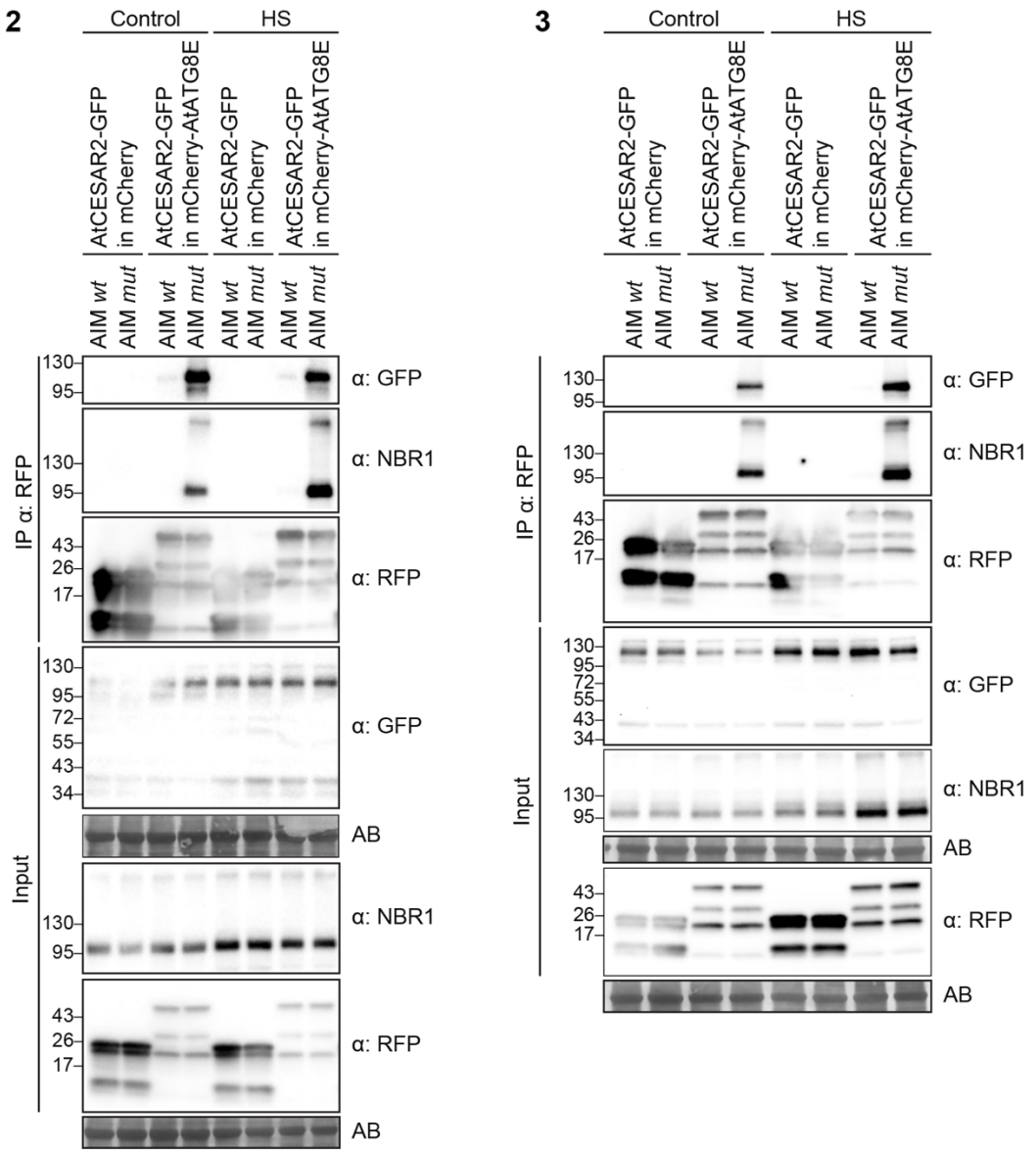

Figure S6. AtCESAR2 co-immunoprecipitates with AtATG8E in vivo. Two independent biological replicates (Replicates 2 and 3) of RFP-Trap co-immunoprecipitation coupled with peptide competition were performed on whole-seedling extracts from 7-day-old *A. thaliana* seedlings co-expressing AtCESAR2-GFP with either mCherry-AtATG8E or mCherry-EV. Replicate 1 is shown in Figure 3H. Seedlings were incubated at either 21°C (Control) or 37°C (HS) for 6 hours, followed by a 4-hour recovery at 21°C in fresh ½ MS + MES + 1% sucrose media. AIM wild-type (wt) and mutant (mut) peptides were added at a final concentration of 100 µM. Protein extracts were analyzed via immunoblotting with the indicated antibodies. Protein size markers (kDa) are shown on the left of the blots. Total protein loading was assessed using Amidoblack (AB) staining.

Fig.S7

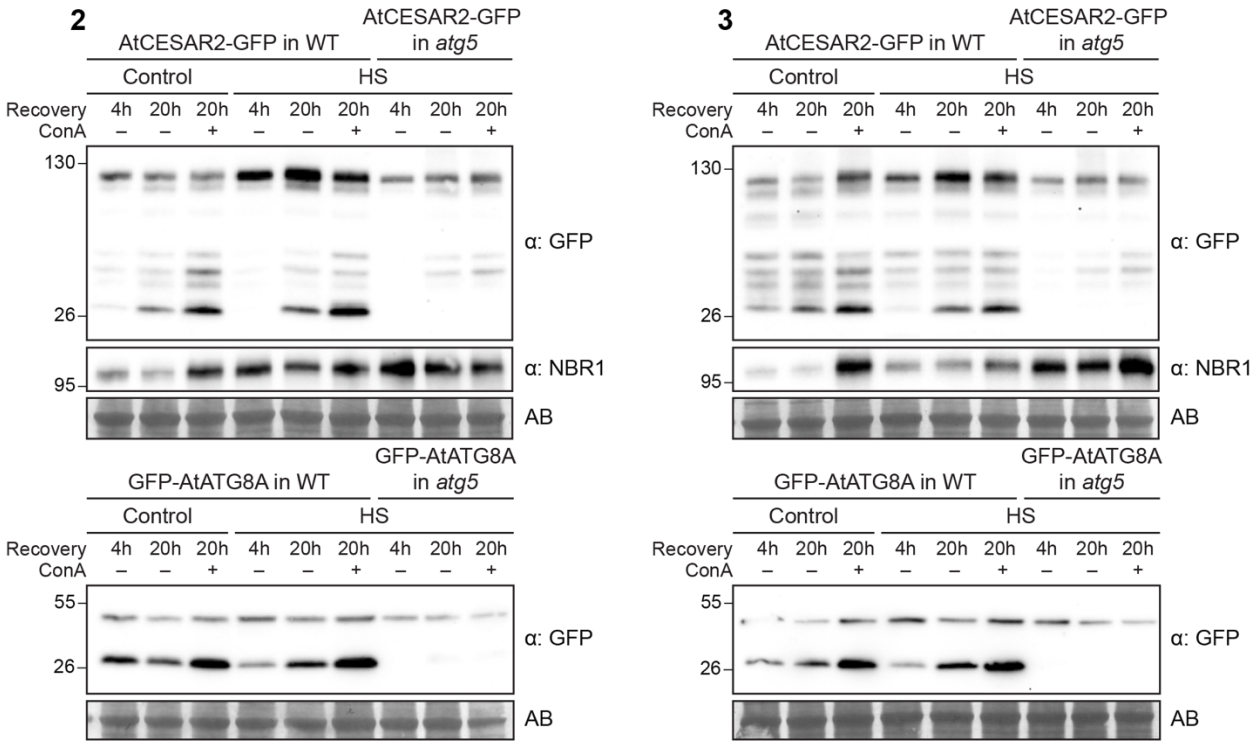

Figure S7. (A) AtCESAR2 undergoes autophagic degradation during extended recovery after heat stress. Two independent biological replicates (Replicates 2 and 3) from the experiment shown in Figure 12C. *A. thaliana* seedlings were grown in ½ MS media for 7 days and incubated at either 21°C (Control) or 37°C (HS) for 4 hours, followed by recovery at 21°C for either 4 or 20 hours in fresh ½ MS + MES + 1% sucrose media with or without 1 µM Concanamycin A (ConA). A total of 20 µg of protein extract was loaded and analyzed via immunoblotting with the indicated antibodies. Protein size markers (kDa) are shown on the left of the blots. Total protein loading was assessed using Amidoblack (AB) staining.

Fig.S8

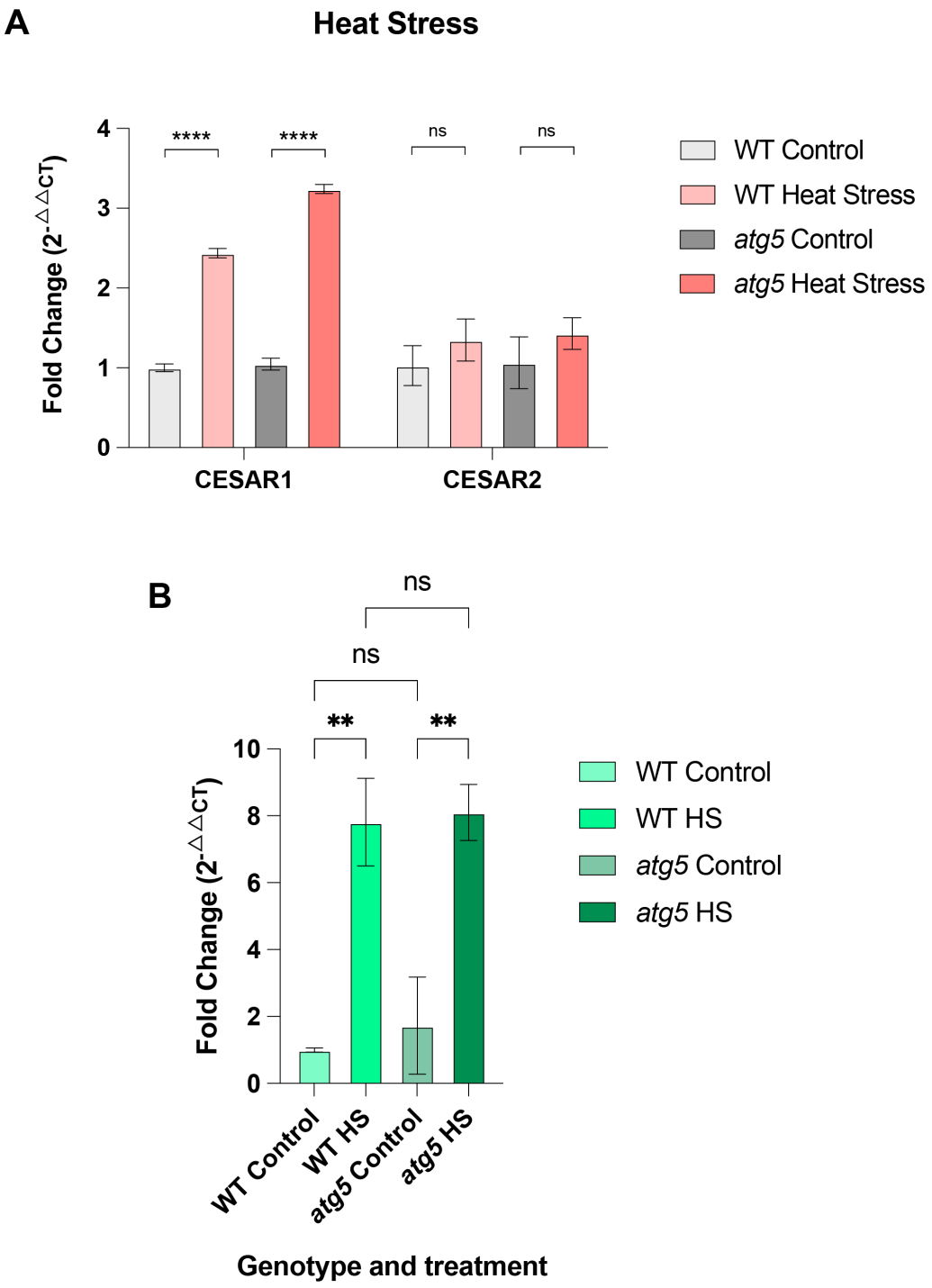
A
Heat Stress
Fold Change (2-△△CT)
4
3
2
1
0
****
****
ns
ns
CESAR1
CESAR2
WT Control
WT Heat Stress
atg5 Control
atg5 Heat Stress
B
ns
ns
**
**
10
8
6
4
2
0
Fold Change (2-△△CT)
WT Control
WT HS
atg5 Control
atg5 HS
Genotype and treatment

Figure S8. (A) Relative expression of CESAR1 and CESAR2 genes in WT and *atg5* under Heat Stress. The relative expression levels of **CESAR1** and **CESAR2** were analyzed in 7d old seedlings of **wild-type (WT)** and ***atg5* mutant genotypes** under control and heat stress (4h followed by a 4h recovery) treatments using quantitative real-time PCR (qRT-PCR). Expression levels were normalized to the reference gene **TIP41**, and the fold changes were calculated using the **2^(-ΔΔCt)** method. The **WT Control condition** was used as the reference condition for both genes. Bars represent the **mean fold change ± standard deviation (SD)** of biological replicates (n = 4). Statistical significance was evaluated for differential expression between Control and Heat Stress within each genotype for each using Unpaired t test with Welch's correction. Asterisks indicate significant differences between groups (*p < 0.05; **p < 0.01; ***p < 0.001****p < 0.0001).**(B) Relative expression of CESAR2-GFP transgene in WT and *atg5* transgenic lines under Heat Stress.** The relative expression levels of **CESAR2-GFP** were analyzed in 7d old seedlings of RPS5p:CESAR2-GFP in **wild-type (WT)** and ***atg5* in mCh-ATG8E** transgenic lines under control and heat stress (4h followed by a 4h recovery) treatments using quantitative real-time PCR (qRT-PCR). Expression levels were normalized to the reference gene **TIP41**, and the fold changes were calculated using the **2^(-ΔΔCt)** method. The **WT Control condition** was used as the reference condition. Bars represent the **mean fold change ± standard deviation (SD)** of biological replicates (n = 4). Statistical analysis was performed using Welch's ANOVA followed by Dunnett's multiple comparisons test to compare the differential expression of CESAR2-GFP transgene between Control and Heat Stress within each genotype. Asterisks indicate significant differences between groups (**p < 0.01).

Fig.S9

A

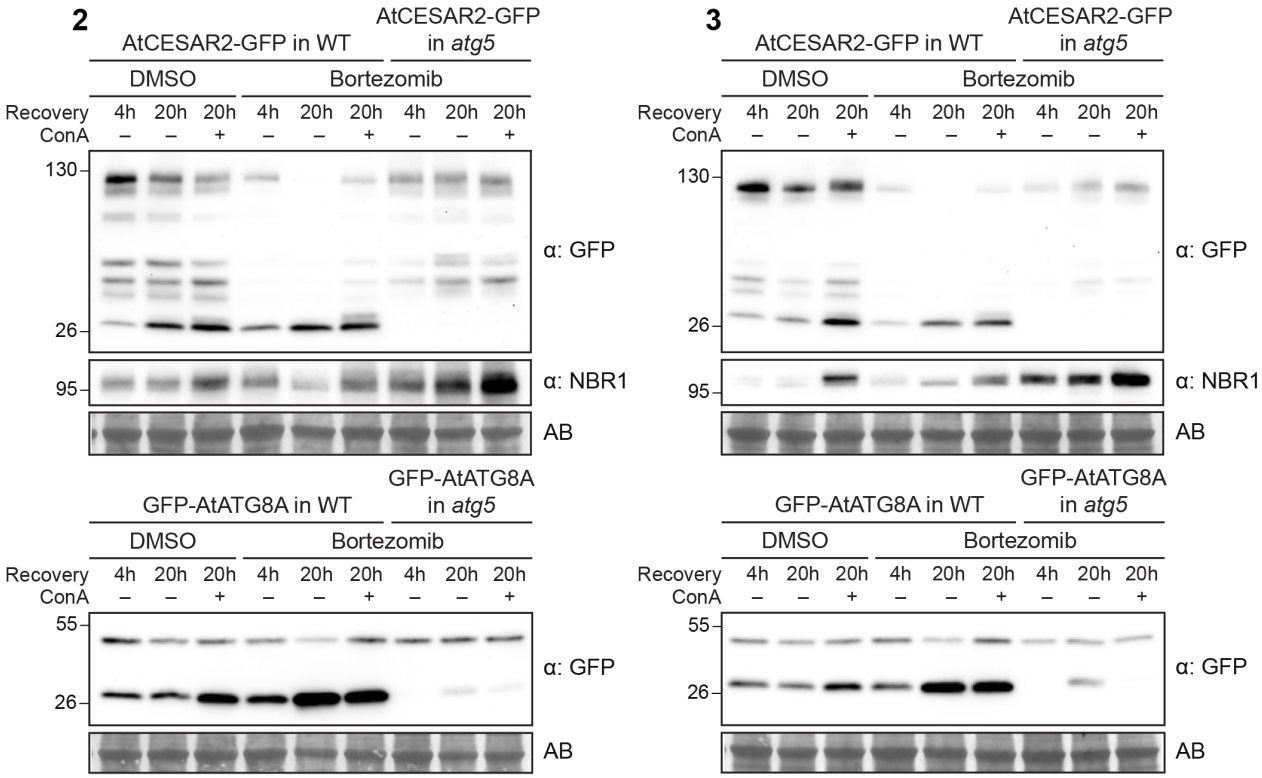
2
AtCESAR2-GFP in WT
AtCESAR2-GFP in atg5
DMSO
Bortezomib
Recovery 4h 20h 20h 4h 20h 20h 4h 20h 20h
ConA – – + – – + – – +
130
26
95
α: GFP
α: NBR1
AB
3
AtCESAR2-GFP in WT
AtCESAR2-GFP in atg5
DMSO
Bortezomib
Recovery 4h 20h 20h 4h 20h 20h 4h 20h 20h
ConA – – + – – + – – +
130
26
95
α: GFP
α: NBR1
AB
GFP-AtATG8A in WT
GFP-AtATG8A in atg5
DMSO
Bortezomib
Recovery 4h 20h 20h 4h 20h 20h 4h 20h 20h
ConA – – + – – + – – +
55
26
α: GFP
AB
GFP-AtATG8A in WT
GFP-AtATG8A in atg5
DMSO
Bortezomib
Recovery 4h 20h 20h 4h 20h 20h 4h 20h 20h
ConA – – + – – + – – +
55
26
α: GFP
AB

B

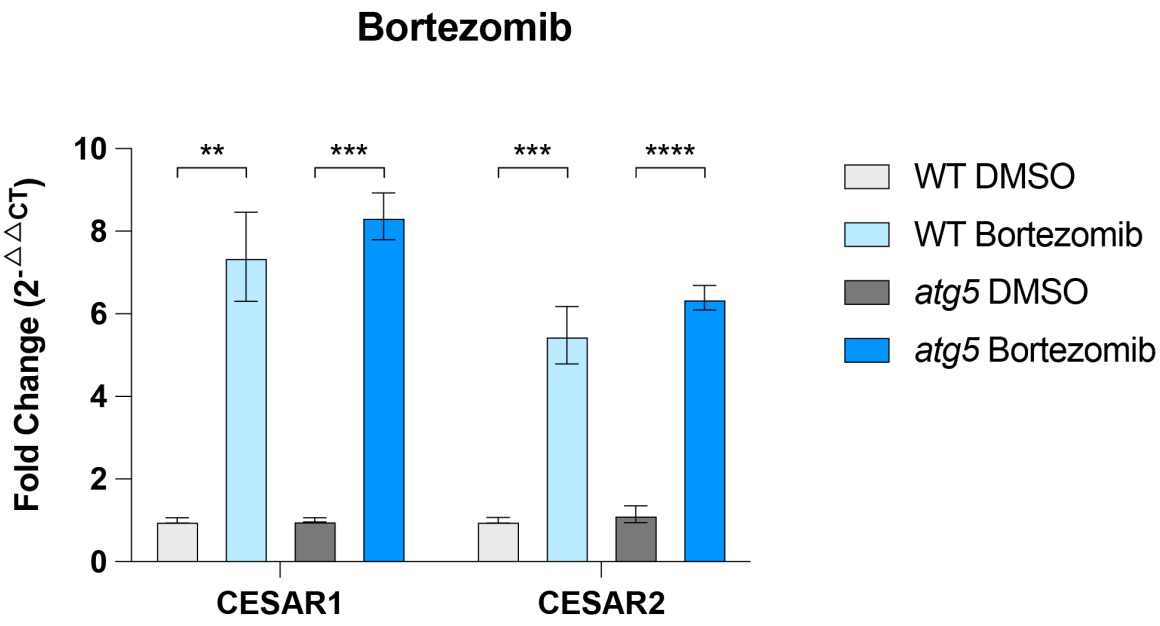
Bortezomib
Fold Change ($2^{-\triangle\triangle CT}$)
10
8
6
4
2
0
**
***
***
****
CESAR1
CESAR2
WT DMSO
WT Bortezomib
atg5 DMSO
atg5 Bortezomib

Figure S9. (A) AtCESAR2 undergoes autophagic degradation following proteasome inhibition. Two independent biological replicates of western blot analyses showing AtCESAR2-GFP (upper panel) and GFP-AtATG8A (lower panel) autophagic flux assays during recovery from proteasome inhibition. *A. thaliana* seedlings were grown in ½ MS + MES + 1% sucrose media for 7 days and incubated in media supplemented with either DMSO or 50 μM bortezomib for 4 hours, followed by recovery periods of either 4 or 20 hours in fresh media with or without 1 μM Concanamycin A (ConA). A total of 20 μg of protein extract was loaded and analyzed via immunoblotting with anti-GFP and anti-NBR1 antibodies. Protein size markers (kDa) are shown on the left of the blots. Total protein loading was assessed using Amidoblack (AB) staining. **(B) Relative expression of CESAR1 and CESAR2 genes in WT and *atg5* under Bortezomib treatment.** The relative expression levels of **CESAR1** and **CESAR2** were analyzed in 7d old seedlings of **wild-type (WT)** and ***atg5* mutant genotypes** under DMSO and 50 μM Bortezomib (4h treatment followed by a 4h recovery) treatments using quantitative real-time PCR (qRT-PCR). Expression levels were normalized to the reference gene **TIP41**, and the fold changes were calculated using the **2^(-ΔΔCt)** method. The **WT DMSO condition** was used as the reference condition for both genes. Bars represent the **mean fold change ± standard deviation (SD)** of biological replicates (n = 4). Statistical significance was evaluated for differential expression between DMSO and Bortezomib within each genotype for each using Unpaired t test with Welch's correction. Asterisks indicate significant differences between groups (*p < 0.05; **p < 0.01; ***p < 0.001; ****p < 0.0001).

Fig.S10

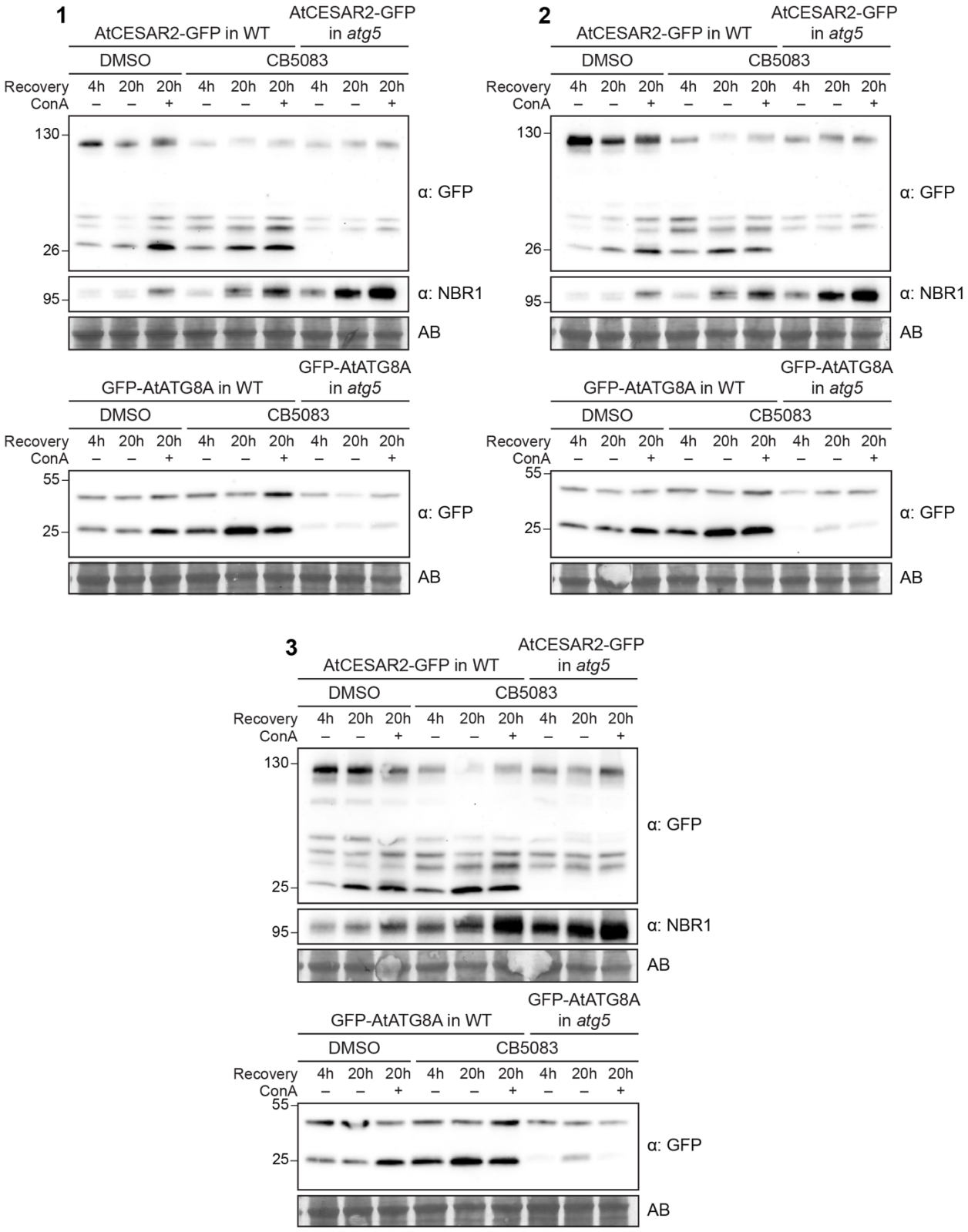
1
AtCESAR2-GFP in WT
AtCESAR2-GFP in atg5
DMSO
CB5083
Recovery 4h 20h 20h 4h 20h 20h 4h 20h 20h
ConA – – + – – + – – +
130
26
95
α: GFP
α: NBR1
AB
2
AtCESAR2-GFP in WT
AtCESAR2-GFP in atg5
DMSO
CB5083
Recovery 4h 20h 20h 4h 20h 20h 4h 20h 20h
ConA – – + – – + – – +
130
26
95
α: GFP
α: NBR1
AB
GFP-AtATG8A in WT
GFP-AtATG8A in atg5
DMSO
CB5083
Recovery 4h 20h 20h 4h 20h 20h 4h 20h 20h
ConA – – + – – + – – +
55
25
α: GFP
AB
GFP-AtATG8A in WT
GFP-AtATG8A in atg5
DMSO
CB5083
Recovery 4h 20h 20h 4h 20h 20h 4h 20h 20h
ConA – – + – – + – – +
55
25
α: GFP
AB
3
AtCESAR2-GFP in WT
AtCESAR2-GFP in atg5
DMSO
CB5083
Recovery 4h 20h 20h 4h 20h 20h 4h 20h 20h
ConA – – + – – + – – +
130
25
95
α: GFP
α: NBR1
AB
GFP-AtATG8A in WT
GFP-AtATG8A in atg5
DMSO
CB5083
Recovery 4h 20h 20h 4h 20h 20h 4h 20h 20h
ConA – – + – – + – – +
55
25
α: GFP
AB

Figure S10. AtCESAR2 undergoes autophagic degradation upon CDC48 inhibition. Three independent biological replicates of western blot analyses showing AtCESAR2-GFP (upper panel) and GFP-AtATG8A (lower panel) autophagic flux assays following CB5083 treatment. *Arabidopsis thaliana* seedlings were grown in ½ MS + MES + 1% sucrose media for 7 days and incubated in media supplemented with either DMSO or 50 µM CB5083 for 4 hours, followed by recovery periods of either 4 or 20 hours in fresh media with or without 1 µM Concanamycin A (ConA). A total of 20 µg of protein extract was loaded and analyzed via immunoblotting with anti-GFP and anti-NBR1 antibodies. Protein size markers (kDa) are shown on the left of the blots. Total protein loading was assessed using Amidoblack (AB) staining.

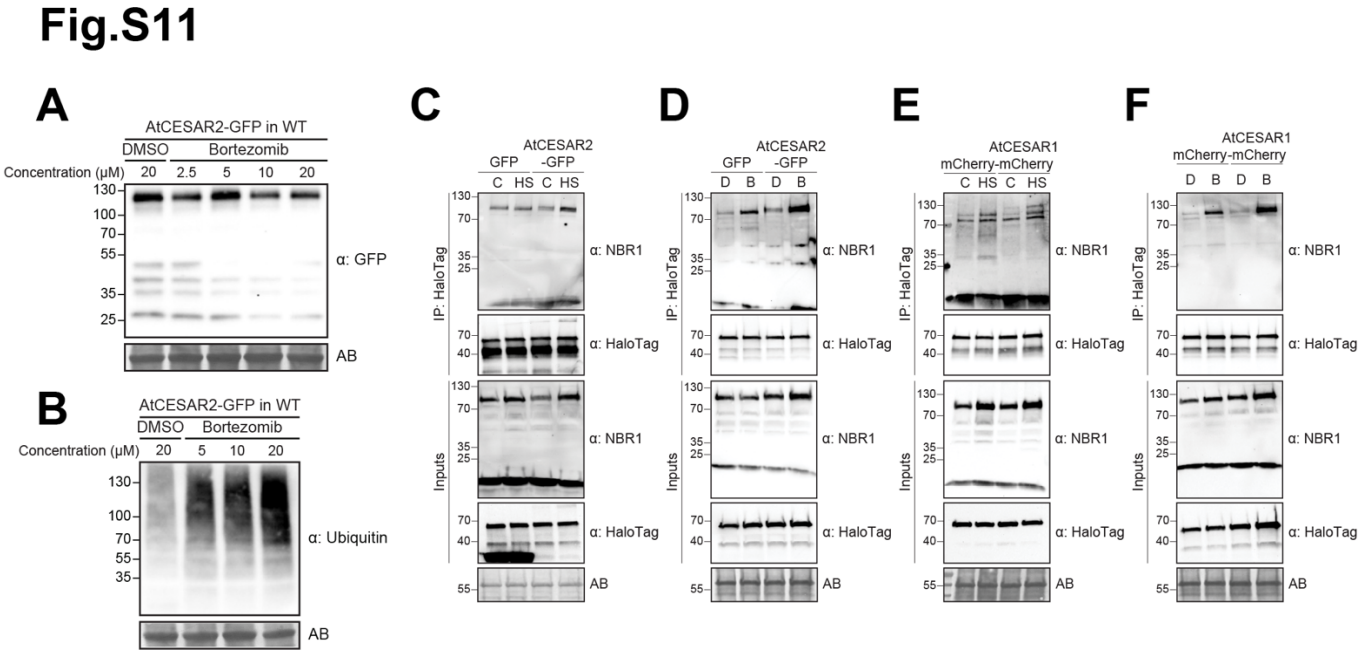

Figure S11. **(A) AtCESAR2 protein levels change in a concentration-dependent manner upon proteasome inhibition.** Western blot analysis of AtCESAR2-GFP protein levels after treatment with varying concentrations of bortezomib. *Arabidopsis thaliana* seedlings were grown in ½ MS + MES + 1% sucrose media for 7 days and incubated in media supplemented with either DMSO or the indicated concentrations of bortezomib at 21°C for 1 hour, followed by a 1-hour recovery in fresh media. A total of 20 µg of protein extract was loaded and analyzed via immunoblotting with an anti-GFP antibody. Protein size markers (kDa) are shown on the left of the blots. Total protein loading was assessed using Amidoblack (AB) staining**. (B) Proteasome inhibition leads**

to the accumulation of ubiquitinated species. Western blot analysis of ubiquitin levels after treatment with varying concentrations of bortezomib. *A. thaliana* seedlings were grown under continuous light in ½ MS + MES + 1% sucrose media for 7 days and incubated in media supplemented with either DMSO or the indicated concentrations of bortezomib at 21°C for 1 hour, followed by a 1-hour recovery in fresh media. A total of 20 µg of protein extract was loaded and analyzed via immunoblotting with an anti-ubiquitin antibody. Protein size markers (kDa) are shown on the left of the blots. Total protein loading was assessed using Amidoblack (AB) staining. **(C-F) NBR1 associates with TUBEs.** Co-immunoprecipitation of Halo-tagged TUBE bait and NBR1 is shown as a positive control for Fig. 16E (Fig. S11C), Fig. 16F (Fig. S11D), Fig. 16G (Fig. S11E), and Fig. 16H (Fig. S11F). Five-day-old *A. thaliana* seedlings expressing either GFP-EV (GFP) or AtCESAR2-GFP (panels E, F), or mCherry-EV (mCherry) or AtCESAR1-mCherry (panels G, H) in a wild-type (Col-0) background were incubated in liquid ½ MS medium with 1% sucrose for 4 hours at 21°C (Control, C) or 37°C (Heat stress, H), followed by a 4-hour recovery at 21°C (panels C, E), or for 1 hour at 21°C in media supplemented with either DMSO (D) or 5 µM bortezomib (B), followed by a 1-hour recovery at 21°C in fresh media (panels D, F). Co-immunoprecipitation was performed using plant lysates incubated with Magne® HaloTag® Beads conjugated with HaloTag-TUBE. Input and bound proteins were detected via immunoblotting with the indicated antibodies. Protein size markers (kDa) are shown on the left of the blots. Total protein loading was assessed using Amidoblack (AB) staining.

Fig.S12

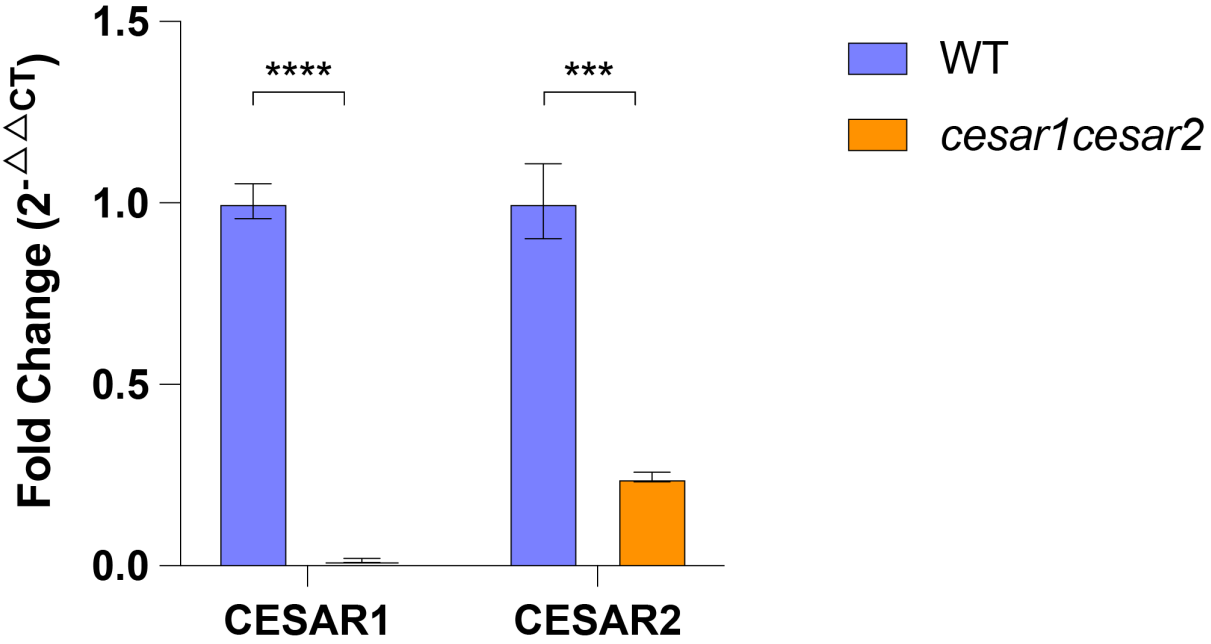

Figure S12. (A) Relative expression of CESAR1 and CESAR2 genes in WT and *cesar1cesar2* The relative expression levels of **CESAR1** and **CESAR2** were analyzed in 7d old seedlings of **wild-type (WT)** and ***cesar1cesar2* genotypes** using quantitative real-time PCR (qRT-PCR). Expression levels were normalized to the reference gene **TIP41**, and the fold changes were calculated using the **2^(-ΔΔCt)** method. The **WT condition** was used as the reference condition for both genes. Bars represent the **mean fold change ± standard deviation (SD)** of biological replicates (n = 4). Statistical significance was evaluated for differential expression of each gene between WT and *cesar1cesar2* using Unpaired t test with Welch's correction. Asterisks indicate significant differences between groups (*p < 0.05; **p < 0.01; ***p < 0.001****p < 0.0001).

Fig.S13

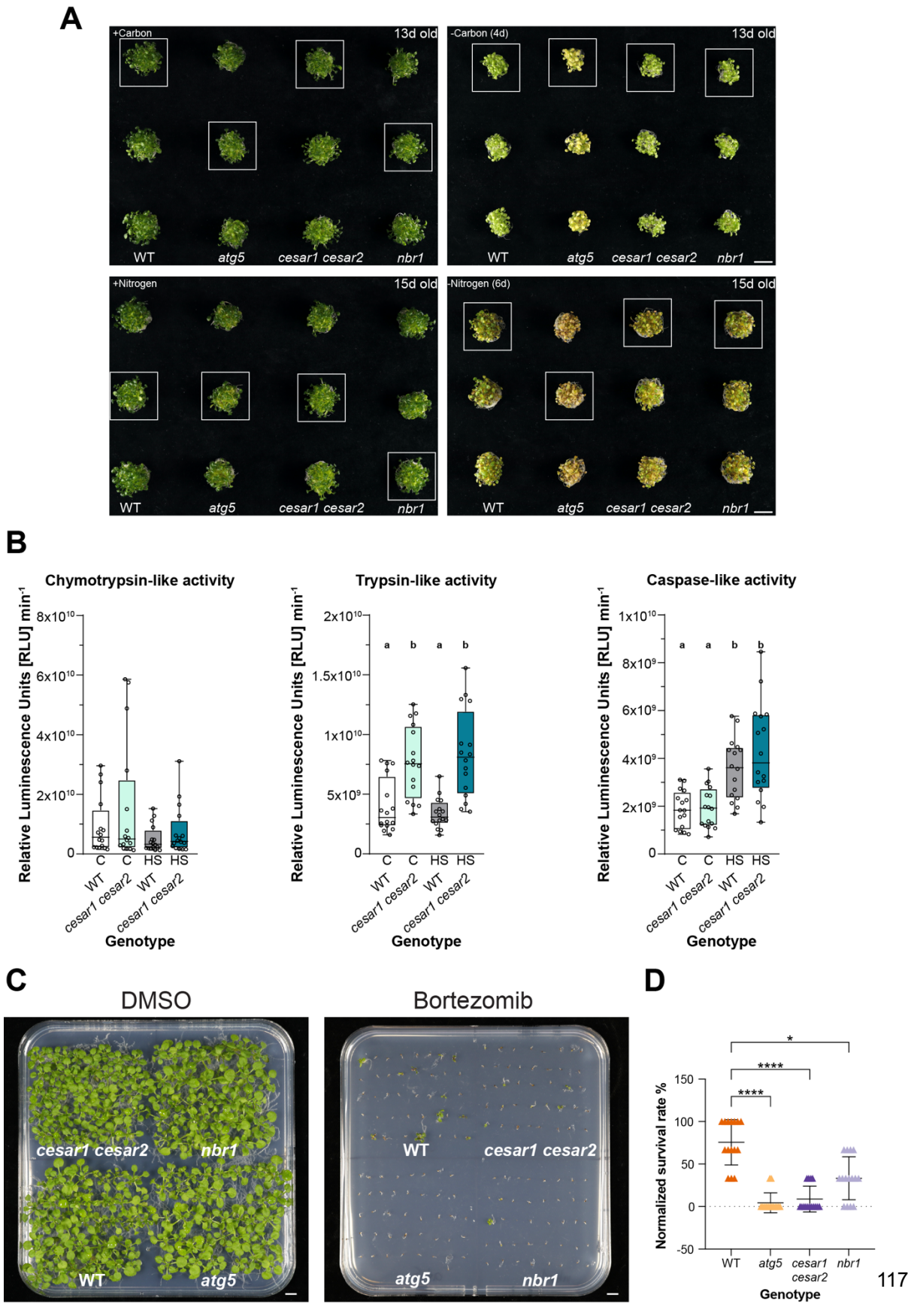
A
+Carbon
13d old
-Carbon (4d)
13d old
+Nitrogen
15d old
-Nitrogen (6d)
15d old
WT
atg5
cesar1 cesar2
nbr1
B
Chymotrypsin-like activity
Trypsin-like activity
Caspase-like activity
Relative Luminescence Units [RLU] min-1
C
HS
Genotype
a
b
C
DMSO
Bortezomib
cesar1 cesar2
nbr1
WT
atg5
D
Normalized survival rate %
****
*
Genotype

Figure S13. CESAR is required for proteotoxic stress tolerance. (A) The cesar1cesar2 mutant is not hypersensitive to starvation. Starvation assays were performed in three independent biological replicates. Nine-day-old *Arabidopsis thaliana* seedlings of the indicated genotypes were grown in ½ MS + MES + 1% sucrose for 9 days, followed by either 4 days of carbon starvation (-C, left) or 6 days of nitrogen starvation (-N, right). Representative images from Fig. 17A are highlighted with a white box. Scale bar: 1 cm. **(B) Proteasome activity is altered in cesar1cesar2 plants.** Boxplots show three distinct protease activities of the 26S proteasome. Protease activities were measured in wild-type (Col-0) and *cesar1cesar2* mutant *A. thaliana* seedlings grown at 21°C (Control) or 37°C (Heat stress, HS) for 4 hours, followed by a 20-hour recovery. Protease activities are expressed in Relative Luminescence Units (RLU) min^{-1}. Each boxplot represents 16 replicates from four experimental repetitions (n = 4 per repetition, with 6 seedlings per repetition). Statistical significance was determined using one-way ANOVA ($P < 0.05$). **(C) The cesar1cesar2 mutant is hypersensitive to proteasome inhibition.** A second independent biological replicate of the bortezomib plate assays shown in Fig. 17D. *A. thaliana* seedlings of the indicated genotypes were grown on 1% agar ½ MS + MES + 1% sucrose plates supplemented with either DMSO (left panel) or 3.75 µM bortezomib for 18 days before imaging. Representative images from six independent biological replicates are shown (n = 240). Scale bar: 1 cm. **(D) Quantification of the survival rate of seedlings grown on bortezomib-containing plates.** The normalized survival rate for the biological replicate of the bortezomib plate assays shown in Fig. 13C is presented. The survival rate for each biological replicate was calculated by dividing the number of seedlings with a phenotype of size greater than 0.3 cm and green coloration by the total number of seeds sown per genotype (40). This value was then normalized to the highest survival rate observed for the wild-type (Col-0) background across all 15 biological replicates (n = 600). Each triangle represents a replicate with 40 seeds per genotype per plate. A Kruskal-Wallis test followed by Dunn's multiple comparisons test was used to evaluate differences in survival rates between genotypes. ***, Adjusted $P < 0.001$; *, Adjusted $P < 0.05$. Non-significant differences are not shown.

Fig.S14

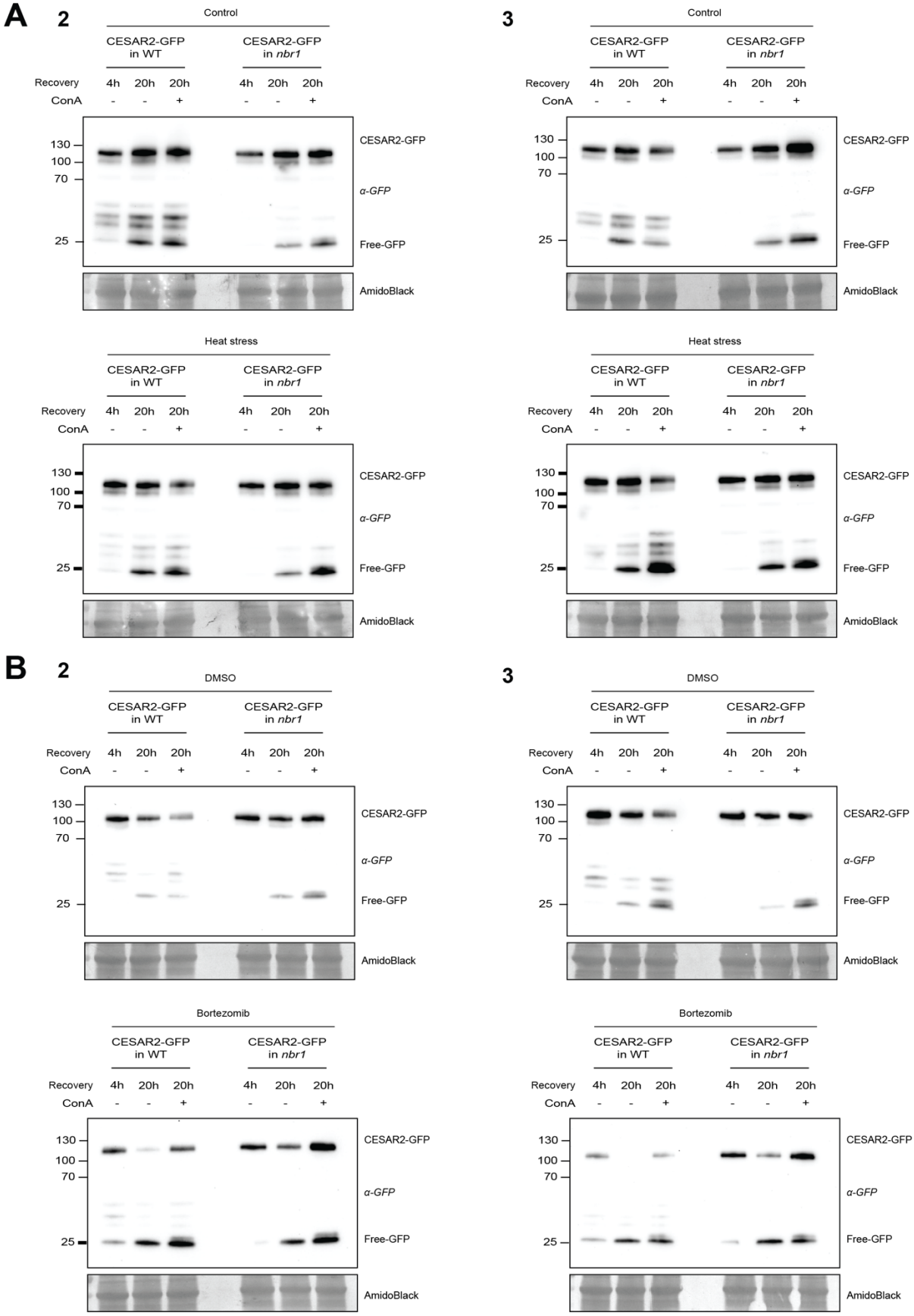
A
2
Control
CESAR2-GFP in WT
CESAR2-GFP in nbr1
Recovery 4h 20h 20h 4h 20h 20h
ConA - - + - - +
130
100
70
25
CESAR2-GFP
α-GFP
Free-GFP
AmidoBlack
Heat stress
3
B
DMSO
Bortezomib

Figure S14. (A) AtCESAR2 autophagic flux decreases in the absence of NBR1. Two independent biological replicates of western blot analyses showing AtCESAR2-GFP autophagic flux assays under control (upper panel) and heat stress (lower panel) in WT and *nbr1* mutant backgrounds. **(B) AtCESAR2 autophagic flux is impaired in the absence of NBR1 upon proteasomal inhibition.** Two independent biological replicates of western blot analyses showing AtCESAR2-GFP autophagic flux assays under DMSO (upper panel) and Bortezomib (lower panel) treatments in WT and nbr1 mutant backgrounds. *A. thaliana* seedlings were grown in ½ MS + MES + 1% sucrose media for 7 days and incubated with the respective treatments for 4 hours, followed by recovery periods of either 4 or 20 hours in fresh media with or without 1 µM Concanamycin A (ConA). A total of 20 µg of protein extract was loaded and analyzed via immunoblotting with anti-GFP antibodies. Protein size markers (kDa) are shown on the left of the blots. Total protein loading was assessed using Amidoblack (AB) staining.

Fig.S15

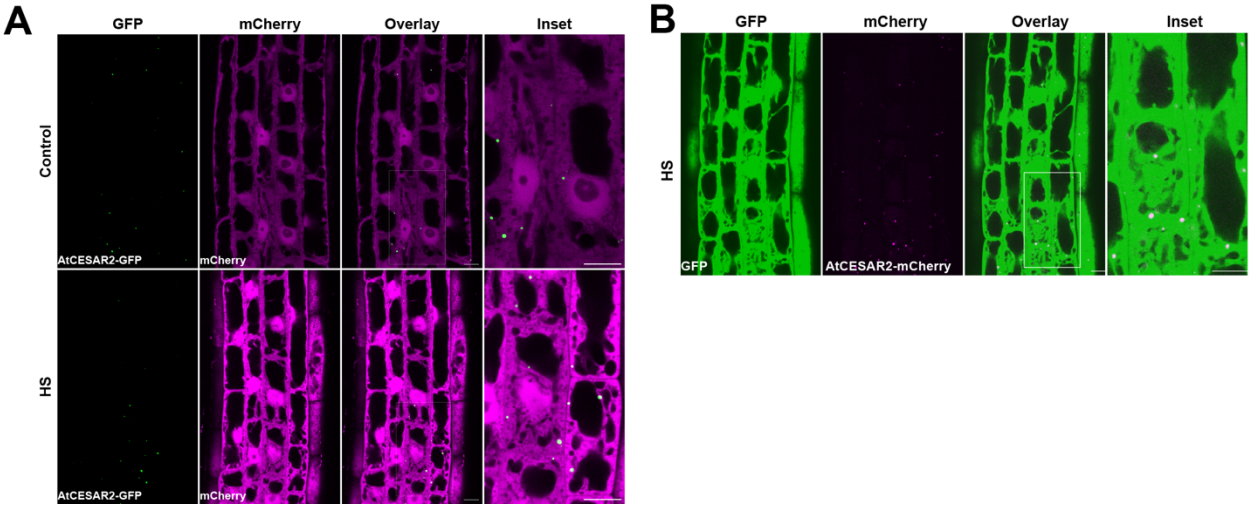

Figure S15. (A) AtCESAR2 does not co-localize with mCherry-EV control. (B) AtCESAR2 does not co-localize with GFP-EV control. Confocal microscopy images of *A. thaliana* root epidermal cells at the transition zone. 5-d-old *A. thaliana* seedlings were grown in 1% agar ½ MS + MES + 1% sucrose plates and incubated at 21ºC (Control, C) or 37ºC (Heat stress, HS) for 3h followed by a recovery of 3h at 21ºC prior to imaging. Area highlighted in the white-boxed region in the merged panel was further enlarged and presented in the inset panel. Scale bars, 10 µm. Inset scale bars, 10 µm.

SUPPLEMENTARY MATERIALS

Materials

Proteomic datasets of Arabidopsis thaliana (Table S10) can be found with other data used for the associated pre-print https://doi.org/10.1101/2024.09.08.611708 in Zenodo: DOI:10.5281/zenodo.13714560

Primers used for cloning and genotyping:

Name	Sequence
ELKS2_CDS_F_1	aataacGGTCTCaGGCTtgATGGGTTTCGGTTCTGTTTATC
ELKS2_CDSint_R_1	caataaGGTCTCtAAATCAGTACTTAGAGCACGG
ELKS2_CDSint_F_2_BsaIMut	caataaGGTCTCtATTTGGTATCAAACATGAACGAGC
ELKS2_CDS_R_2	gttattGGTCTCtCTGAGTACCAAACAACTTGTTCGGTT
ELKS2_fragment2_BsaImut_F	GACATCTTTGACAAGGAAACCG
ELKS2_fragment2_BsaImut_r	AACAACTTGTTCGGTTTCCTTG
cesar2-1_LP	GCTCTGAAATGCTTCCAGATG
cesar2-1_RP	CCACAGCACGACTTAGTCCTC
cesar1-1_LP	CTCCAGTTGCTGTTTAGCCTG
cesar1-1_RP	TCCATCACAGTGAACAAGGTTC
cesar2-1_LP	GCTCTGAAATGCTTCCAGATG

Primers used for qPCR:

Primer	Sequence
CESAR1_qPCR_ex3-4_FWD	CAGATCAACCCAGGGATGCA
CESAR1_qPCR_ex3-4_REV	CCTTTGCCTTTTCTGCCTCC
CESAR2_qPCR_ex2-3_FWD	AGCGCGAAGTAGAACATGGT
CESAR2_qPCR_ex2-3_REV	GGTTGCAAGGTTGTTAGCTCG
TIP41_qPCR_F	TGAACTGGCTGACAATGGAGTG
TIP41_qPCR_R	CATGAGCTTGGCATGACTCTCAC

Plasmids used for plant transformation:

Name	**Identifier**	**Reference**
pGGSun		10.1073/pnas.2302069120
pGGSun-pRPS5:CESAR2_GFP	AT1G03290.1	This study
pGGSun-pRPS5:CESAR1_mCherry	AT4G02880.1	This study
pGGSun-pRPS5:CESAR2_mCherry	AT4G02880.1	This study

Peptides

Name	**Source**	**Sequence**
AIM *wt*	Synthetized *in house*	EPLDFDWEIVLEEEM
AIM *mut*	Synthetized *in house*	EPLDFDAEIALEEEM

Antibodies:

Antibody	Host	Supplier	Cat. #	Working concentration
Anti-Rabbit IgG HRP-Conjugate	Goat	Bio-Rad	1706515	1:5000
Anti-Mouse IgG-HRP Conjugate	Goat	Bio-Rad	1706516	1:5000
Anti-GFP	Mouse	Roche	11814460001	1:2500 and 1:5000
Anti-GFP	Rabbit	Invitrogen	A11122	1:5000
Anti-mCherry	Rabbit	Proteintech	26765-1-AP	1:5000
Anti-RFP 6G6	Mouse	Chromotek	AB_2631395	1:5000
Anti-GFP polyclonal	Chicken	Abcam	ab13970	1:80
Anti-mCherry polyclonal	Rabbit	Abcam	ab167453	1:40
Anti-rabbit IgG 10 nm	Goat	Electron Microscopy Sciences	SKU.25109	1:20
Anti-chicken IgG 15 nm	Goat	Electron Microscopy Sciences	SKU.25591	1:40
Anti-GST HRP-Conjugate	Goat	GE Healthcare	RPN1236	1:5000
Anti-MBP	Mouse	Sigma Aldrich	M1321	1:5000
Anti-NBR1	Rabbit	Agrisera	AS14 2805	1:10000
Anti-HaloTag	Mouse	Promega	G9211	1:5000
Anti-Ubiquitin	Mouse	Santa Cruz Biotechnology	3936	1:5000

Inhibitors and drugs

Name	Supplier	Cat. #
Bortezomib	Santa Cruz Biotechnology	sc-217785
CB5083	BIOCAT GmbH	T6796-50mg-TM
Concanamycin A (ConA)	Santa Cruz Biotechnology	sc-202111A